NANOSTRUCTURED METAL BORIDES AND METAL FLUORIDES

by

ROSHINI RAMACHANDRAN

(Under the Direction of Tina T. Salguero)

ABSTRACT

The metal borides are well known for their high melting points, strength and hardness which make them useful for high performance applications. Conversely, the metal fluorides are renowned for their stability, transparency and ability to host other cations for a range of imaging and biomedical applications. Excitedly, we have developed two different synthetic methods for nanostructuring the metal borides and metal fluorides. Herein, we discuss our efforts at synthesizing different nanomorphologies of these materials. Chapter II details how we can synthesize nanoparticles of SrB_6 using a novel top-down ion incorporation technique. Chapters III discusses similar synthetic strategies for producing nanosheets of LaB_6. Chapter IV outlines top-down efforts made at forming nanostructured CeB_6, CaB_6 and SmB_6. Chapter V discusses the synthesis of AlB_2 nanosjeets using a top-down exfoliation technique. Finally, Chapter VI details the bottom-up formation of CaF_2 nanosheets and nanostructured lanthanide fluorides using the CaF_2 nanosheets as a template.

INDEX WORDS: metal borides, metal fluorides, nanosheets, two-dimensional materials, exfoliation, lithium incorporation, nanostructure, solid-solution, doping, nanoscroll

NANOSTRUCTURED METAL BORIDES AND METAL FLUORIDES

by

ROSHINI RAMACHANDRAN

M.Sc., Anna University, India, 2012

A Dissertation Submitted to the Graduate Faculty of The University of Georgia in Partial Fulfillment of the Requirements for the Degree

DOCTOR OF PHILSOPHY

ATHENS, GEORGIA

2017

NANOSTRUCTURED METAL BORIDES AND METAL FLUORIDES

by

ROSHINI RAMACHANDRAN

Major Professor: Tina T. Salguero

Committee: John Stickney

Jin Xie

Electronic Version Approved:

Suzanna Barbour

Dean of the Graduate School

The University of Georgia

August 2017

DEDICATION

To Appa - for always believing in my dreams

ACKNOWLEDGEMENTS

I am very grateful for my family, Amma, Rohit, Thatha and Patti, for being a constant source of support throughout these years. I thank my husband, Pradeep Kumar, for being my strength and my biggest cheerleader.

I acknowledge my fellow Salguero group members who helped me throughout my graduate years- Dr. Timothy Pope, Dr. Matt Davidson, Dr. Darrah Johnson-McDaniel, Dr. Eric Formo, Dr. Christopher Barrett, Gregory Neher, Matt Bloodgood, Monika Milkovska, Harshani Rathnaweera, Eman Abdelrahman, Nick Nguyen, Mayra Pedraza, Yassamin Ghafouri, Hayden Evans, and Asma Sharafi. I also acknowledge undergraduate researchers Samuel Baxter and Patrick Eaves who assisted me in some topics in this thesis. I would like to thank Dr. Johannes Leisen who has been a great resource for NMR experiments.

I would like to express my immense gratitude to my research advisor, Dr. Tina Salguero, who showed me the real meaning of ‘science’. I am also very grateful for her mentorship and encouragement to help me evolve as a teacher. I would also like to thank my committee members, Dr. John Stickney and Dr. Jin Xie for their assistance and mentorship.

TABLE OF CONTENTS

CHAPTER 1

INTRODUCTION AND LITERATURE REVIEW

Nanomaterials

"Nano" has been the buzzword of the last decade due to the push to move towards incorporating smaller materials in devices. In recent years, nanotechnology emerged as a solution to many problems faced in materials science.[1] Nanomaterials are defined as materials where at least one dimension is in the nanoscale (below 100 nanometers). At this scale, these materials can display unique optical, magnetic and electrical properties in comparison to the bulk.[2] By carefully tuning the morphology of the nanomaterials, one can tune their properties to expand a material's abilities and usefulness in many applications like electronics, medicine and mechanics.[2]

There are two broad approaches for fabricating nanostructured materials, the 'top-down' and 'bottom-up' methods. The top-down method deals with techniques aimed at the disassembly of a bulk structure. This is achieved by many ways- milling[3], sonication[4], micromechanical cleavage[5] and ion-intercalation[6] to name a few. Top-down approaches have better scalability, synthetic ease and low cost. However, the nanostructures formed may have a broad size distribution and defects in the crystal structure due to the nature of this method.

The bottom-up method involves the synthesis of nanostructures starting at the atomic level. This uses smaller building blocks such as soluble precursors, substrates for controlled growth, or layer depositions. Bottom-up approaches typically utilize templates or size control agents for nanostructuring.[7,8] The nanomaterials formed from these methods are more homogeneous, with less defects and have better short and long range ordering. Although it easier to control the size,

chemical composition and dimensionality of the product, bottom-up approaches tend to be expensive and non-scalable due to the usage of specialized equipment and conditions.

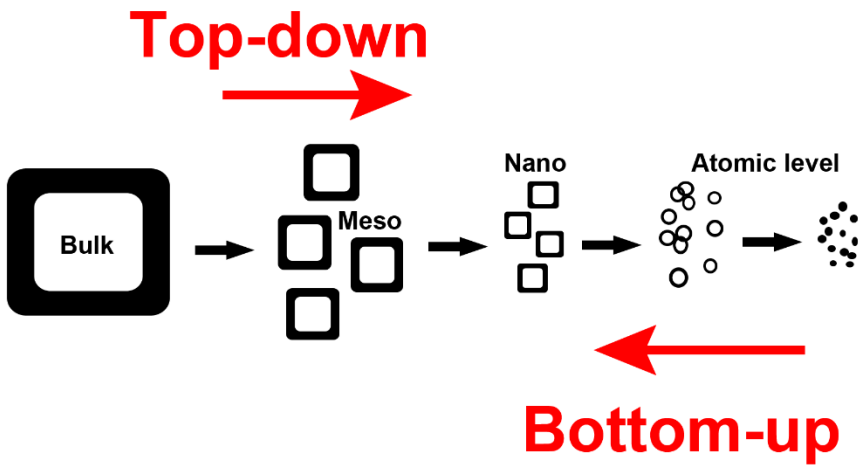

Figure 1.1. Schematic representation of top-down and bottom-up approaches

Many different morphologies of nanomaterials can be formed using top-down and bottom-up methods. They can be classified under zero dimensional (0-D), one dimensional (1-D) and two dimensional (2-D) nanomaterials. 0-D materials have all dimensions within the nanoscale (below 100 nm), eg: nanoparticles and quantum dots. 1-D materials have one dimension outside the nanoscale, eg: nanorods, nanowires, nanotubes. 2-D materials have two dimensions outside the nanoscale (typically the lateral dimensions), eg: nanosheets, nanofilms. Three dimensional nanomaterials consist of larger structures are not confined to the nanoscale in any dimensions, however, they comprise a nanocrystalline structure or multiple nanolayers. The dimensionality of nanostructures play an important role in their properties as they are influenced by their surface area-to-volume ratio and morphology, and subsequently can be tailored for specific applications.

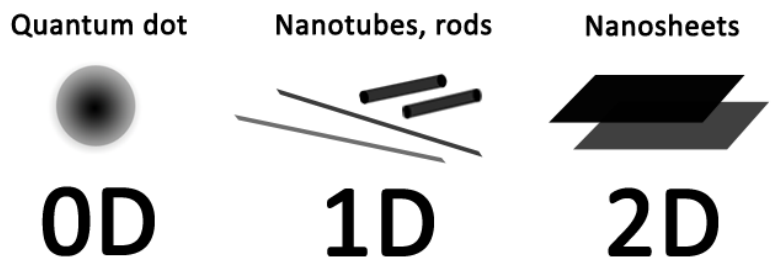

Figure 1.2. Illustration of the different dimensions of nanomaterials

Since the Nobel Prize in Physics was awarded for graphene in 2010, interest in the area of nanosheets has increased considerably. A nanosheet is a two-dimensional material with thickness < 100 nm and lateral dimensions >1 µm. Nanosheets can have different properties from their bulk as they exhibit quantum confinement effects.[1] In nanosheets, not only their size but also spatial factors like dimensionality and anisotropy determine their properties.[1]

Besides graphene, there are many other layered materials that can form nanosheets. The term 'nanosheet' was coined by Sasaki in as early as 1996, when he applied a top-down approach called 'exfoliation' to convert a layered titanate to its constituent nanosheets.[9] Several synthetic techniques have been employed for top-down exfoliation of various layered materials such as ultrasonication[10], ion-intercalation[6], leaching[11], and micromechanical cleavage[5].

Bottom-up synthesis of nanosheets involves templating[7,8,12], solvothermal techniques[13,14], directed growth[15] and layer confinement[16,17]. Bottom up synthesis can be used to create nanosheets of both layered and non-layered materials, however top-down approaches have only been used for layered materials to date.

This next few sections detail the two classes of materials that we worked with, the metal borides and metal fluorides, and efforts at nanostructuring them using both synthetic approaches.

Metal Borides

Metal boride ceramics are a well-known class of high performance materials. They exhibit very high thermal and oxidative stability, and have incredibly high melting points (excess of 2000 ^{o}C). They also possess extreme mechanical strength and are chemically inert. Besides these properties, several metal borides possess other extraordinary qualities; MgB_2 is a high temperature superconductor with T_c of 39 K,[18] ZrB_2 and HfB_2 are ultra high temperature ceramics (UHTC'S) with melting points above 3200 °C[19] and ReB_2 displays superhardness.[20] Metal borides are one of few material systems with properties suitable for hypersonic applications- ZrB_2 and HfB_2 are leading candidates for use in projectiles and rocket nozzles.[19] Other borides such as LaB_6 and CeB_6 have the highest electron emissivities known and are used as robust cathodes.[21]

Metal borides can be classified into two categories based on their boron to metal ratio, metal rich borides and boron rich borides. Each category can be further divided into subcategories depending on the types of boron frameworks that exist within the structure. Metal rich borides consist of chains of boron atoms (eg. FeB), discrete B_2 or B_3 units (eg. V_3B) or sheets of boron atoms (eg. CrB_2) in the metal boride lattice. In the case of boron rich borides, there are more complex three dimensional boron frameworks within the crystal such as octahedra (eg. CeB_6), cuboctahedra (eg. YB_{12}) and icosahedral boron arrangements (eg. AlB_{12}). The high performance properties of metal borides arise from the presence of the boron frameworks which provide stability and robustness to the metal borides.[22]

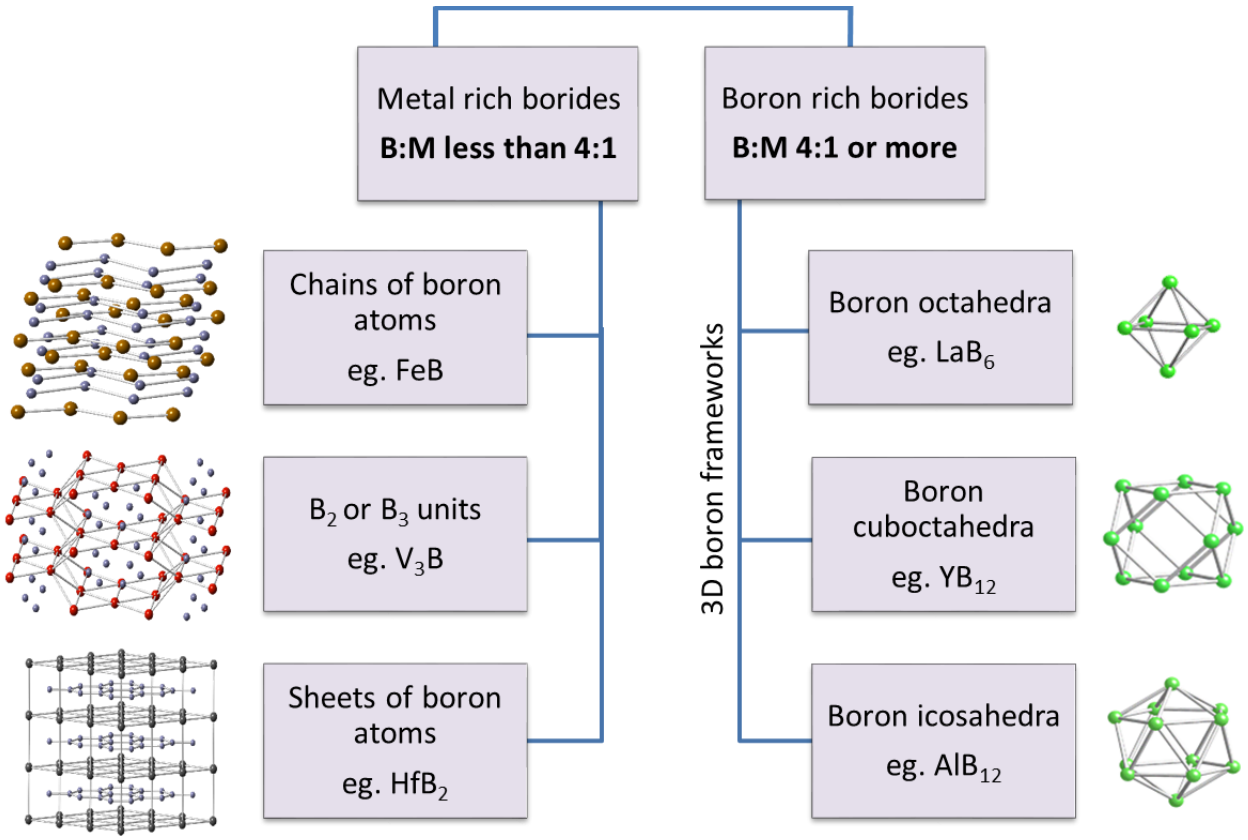

Figure 1.3. Classification of metal borides

Even though metal borides have exceptional properties, their industrial use is limited because they are difficult to process. Their high melting points (excess of 1500 ºC) make it challenging to convert them to thin films for coatings. Currently, methods being employed to make thin films of metal diborides are physical and chemical vapour deposition, but the drawback to these techniques is that we have little control over the thickness and uniformity of the coating formed.[23] Converting the metal borides into nanosheets would open up a wide range of processing options. Since nanosheets have a tendency to lay flat, self-assemble by stacking, and form thin films easily, they serve as a junction between nanoscale and macroscale regimes. Nanosheets stay suspended colloidally in water and other solvents over long periods of time. We can use simple techniques such as spray deposition, dip coating or inkjet printing to apply them on surfaces.

The focus of my research is to develop an innovative exfoliation technique for converting certain metal borides into nanosheets. Among the metal boride series, we have targeted the metal diborides and metal hexaborides due to their desirable properties and applications in UHTC's and cathodes, respectively. Metal diborides (MB_2) have a layered, hexagonal crystal structure with sheets of boron atoms alternating with aluminum atoms in a hexagonal arragement.[21] Examples are CrB_2, ZrB_2, HfB_2, TiB_2. Metal hexaborides (MB_6) have a cubic crystal structure with metal ions and boron octahedra occupying the cubic sites.[24] Examples include LaB_6, CaB_6, CeB_6, SmB_6.

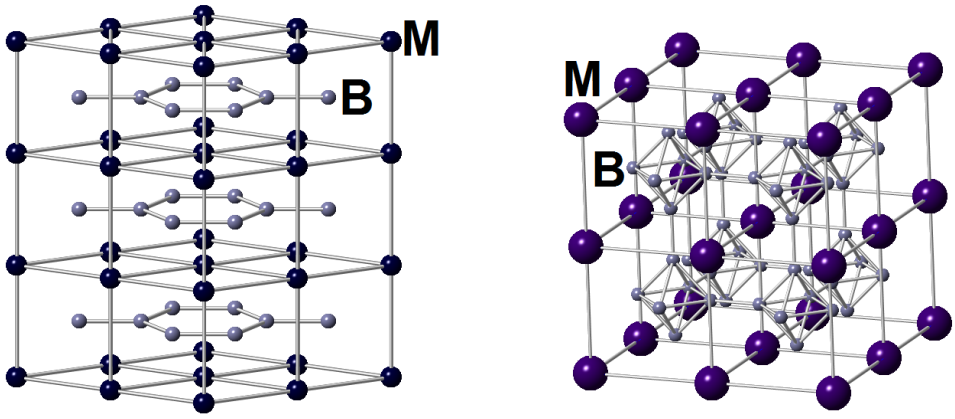

Figure 1.4. Crystal structure of metal diborides (left) and metal hexaborides

Research Approaches

I employ a top-down approach targeted at the disassembly of metal boride structures. In these compounds, the atoms are held together by ionic and covalent interactions.[22] These interactions are much stronger than the van der Waals bonding existing in layered materials such as graphite and metal chalcogenides. Therefore, typical exfoliation conditions such as sonication and micromechanical cleavage do not work with the metal borides.

Our synthetic methodology to make nanosheets is via an alkali metal insertion-exfoliation reaction. We use various lithation reactions to insert lithium ions into the metal boride lattice to form a 'lithiated' or lithium doped metal boride. There have been reports of lithium borides in the literature, with different compositions of Li and B.[25-29] We are especially interested in lithium borides with structures similar to the metal diborides and metal hexaborides, specifically LiB_2 and Li_2B_6. Although the few reports on LiB_2 deal with computational calculations,[26] there are reported syntheses on dilithium hexaboride Li_2B_6,[29] which has a tetragonal crystal structure with boron octahedral frameworks. The Li^+ ions in the structure are mobile, and have more than one site of partial occupancy.[29] Our lithiation reaction aims to incorporate Li^+ into the metal boride crystal lattice to form stable Li_2B_6-MB_6 or LiB_2-MB_2 solid solution intermediates. We hypothesize that the incorporation of lithium ions would occur through a cation exchange or be inserted in a completely new site in the crystal structure.

The next step in our nanostructuring/exfoliation process is to react the lithiated metal boride with deionized water. This removes the lithium ions as lithium hydroxide through a highly vigorous and exothermic reaction possibly accompanied by H_2 evolution. Lithium borides can be water-sensitive[29], therefore, this "exfoliation" reaction would cause a disassembly of the metal boride structure, and this would be enhanced with a subsequent ultrasonication step.

Metal Fluorides

Metal fluorides are of great importance in for diverse applications such as microelectronics, optoelectronics, coatings and catalysis.[30,31] They are non-hygroscopic, stable with respect to oxidation, and possess high transparency over a wide wavelength region.[32,33] Metal fluorides have various crystal structures ranging from cubic in the case of metal monofluorides and difluorides, to hexagonal and orthorhombic in the case of metal trifluorides and tetrafluorides.

Metal fluorides can be broadly classified into low oxidation state metal fluorides and high oxidation state metal fluorides. Under low oxidation state metal fluorides, metals have oxidation state +3 and below. These fluorides are ionic with comprise the monofluorides, difluorides, trifluorides and tetrafluorides. Their properties such as melting point, solubility, and bonding vary depending on the structure and metal present. Eg. CaF_2 (fluorite), LaF_3 (tysonite), ZrF_4.

High oxidation metal fluorides have metals in oxidation state +5 and above. The bonding existing in these compounds is covalent and they are subcategorized into pentafluorides, hexafluorides and heptafluorides. Their physical state varies with WF_6 being a gas, MoF_6 is a liquid, while other high oxidation metal fluorides are volatile solids.

The alkaline earth metal fluorides CaF_2 and BaF_2, are most popular due to their ability to act as host crystals for a variety of cations, especially lanthanides, for bioimaging applications.[34] Lanthanide fluoride materials are promising targets for bio-detection, upconversion, and laser applications, especially in nanostructured forms, due to their strong photoluminescence, excellent stability, and low toxicity.[35-37] Nanostructured metal fluorides have been produced by a wide range of methods such as co-precipitation,[33] sol-gel,[38] microemulsion,[30,32] and hydrothermal techniques.[39] However, two dimensional structures have not been explored for the metal difluoride system, as their crystal structure is not layered. Synthesizing nanosheets of alkaline-earth metal

difluorides would be advantageous as they could then be doped or used as a template for creating lanthanide containing fluorides for the above mentioned applications.

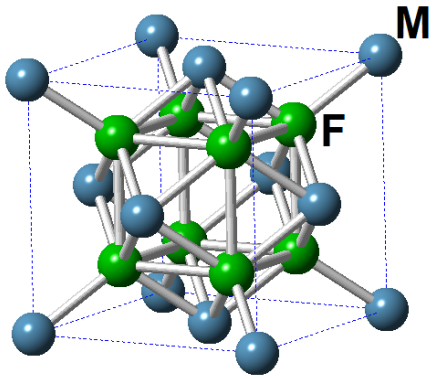

Figure 1.5. Cubic crystal structure of CaF_2

Research Approaches

We synthesized CaF_2 nanosheets using a bottom-up nanofabrication technique. We directed the two-dimensional growth of CaF_2 through interlayer confinement and templating within calcium silicide ($CaSi_2$) by reacting it with HF(aq). $CaSi_2$ is a layered material, which has a structure comprised of covalently-bonded, corrugated silicide $(Si_2^{2-})_n$ sheets alternating with Ca^{2+} that is ideal for interlayer reactions. $CaSi_2$ has been previously reacted with HCl or metal chlorides to produce a range of silicon-based products[40-47] and various other intermediate products,[48-50] depending on the conditions. According to the accepted mechanism, HCl(aq) reacts with the interlayer Ca^{2+} of $CaSi_2$ to produce soluble $CaCl_2$ while the silicide layers become hydroxylated under the acidic aqueous conditions.

In our synthetic methodology, we utilize the layered nature of $CaSi_2$ in a quite different way by transforming the Ca^{2+} into CaF_2 while solubilizing the silicide. Since CaF_2 is insoluble in water, it gets precipitated out immediately when the Ca^{2+} cations come in contact with the F^- anions

under aqueous conditions. However, the silicide layers provide for interlayer confinement and templating effects within the $CaSi_2$ lattice serve to direct the formation of CaF_2 into the desired nanosheet morphology.

We then utilized the CaF_2 nanosheets as a template to react with salts of the lanthanide series at ambient conditions to form lanthanide fluorides. The goal was to dope the calcium fluoride nanosheets or cause a topochemical conversion into the lanthanide fluoride while preserving the nanosheet morphology.

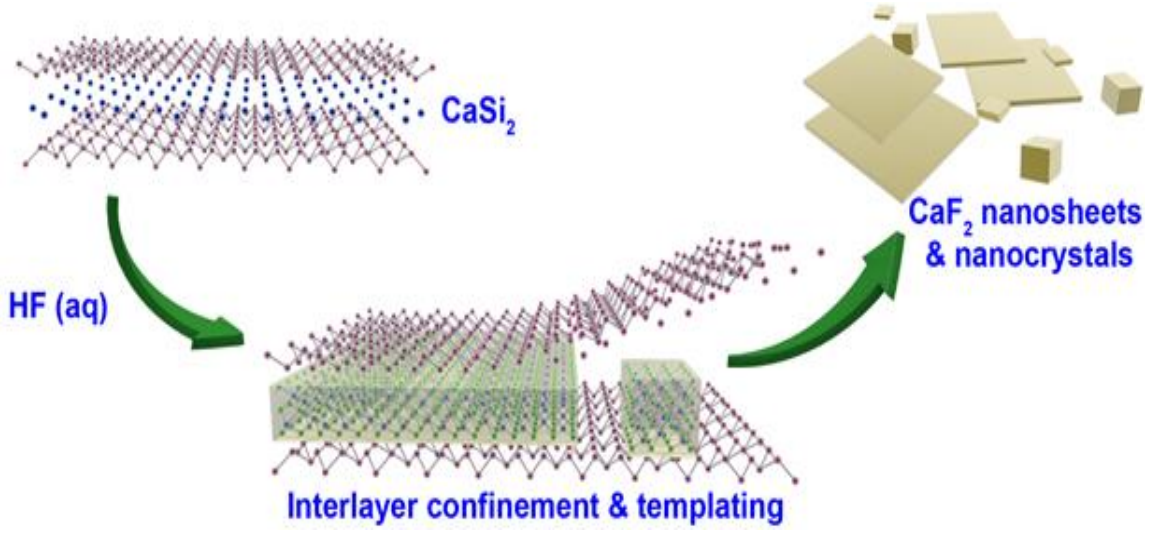

Figure 1.6. Schematic representation of the formation of CaF_2 nanosheets

References

1. Merkle, R. C. *Spectrum.* **2001**. *38*. 19

2. Hewakuruppu, Y.L., Dombrovsky, L.A., Chen, C., Timchenko, V., Jiang, X., Baek, S., Taylor, R.A. *Appl. Opt.* **2013**. 52. *24*. 6041–6050.

3. Liu, S., Huang, Z.L., Liu, G., Yang, G.B. *Int. J. Refract. Met. H*. **2006.** 24. *6*. 461-464.

4. Hernandez, Y., Nicolosi, V., Lotya, M., Blighe, F.M., Sun, Z., De, S., McGovern, I.T., Holland, B., Byrne, M., Gun'Ko, Y.K., Boland, J.J. *Nat. Nanotechnol*. **2008**. 3. 9. 563-568.

5. Novoselov, K.S., Jiang, D., Schedin, F., Booth, T.J., Khotkevich, V.V., Morozov, S.V., Geim, A.K. *Proc. Natl. Acad. Sci. U.S.A.* **2005**. 102. *30*. 10451-10453.

6. Ding, Z., Bux, S.K., King, D.J., Chang, F.L., Chen, T.H., Huang, S.C., Kaner, R.B. *J. Mater. Chem*. **2009.** 19. *17*. 2588-2592.

7. Kitaura, R., Imazu, N., Kobayashi, K. and Shinohara, H. *Nano lett.* **2008.** *8*. 2. 693-699.

8. Zheng, M., Wang, Z.S., Zhu, Y.W. *Trans. Nonferrous Met. Soc. China.* **2006**. 16. *6*. 1348-1352.

9. Coleman, J.N., Lotya, M., O'Neill, A., Bergin, S.D., King, P.J., Khan, U., Young, K., Gaucher, A., De, S., Smith, R.J., Shvets, I.V. *Science*. **2011**. 331. *6017*. 568-571.

10. Ma, R., Sasaki, T., Bando, Y. *J.A.C.S*. **2004**. 126. *33*. 0382-10388

11. Johnson-McDaniel, D., Barrett, C.A., Sharafi, A., Salguero, T.T. *J.A.C.S*. **2013**. 135. *5*. 1677-1679.

12. Pope, T.R., Lassig, M.N., Neher, G., Weimar III, R.D., Salguero, T.T. *J. Mater. Chem. C*. **2014**. 2. *17*. 3223-3230.

13. Yang, H.G., Liu, G., Qiao, S.Z., Sun, C.H., Jin, Y.G., Smith, S.C., Zou, J., Cheng, H.M., Lu, G.Q. *J.A.C.S*. **2009**. 131. *11*. 4078-4083.

14. Choi, H.G., Jung, Y.H., Kim, D.K. *J.A.C.S*. **2005**. 88. *6*. 1684-1686.

15. Li, H., Zhang, Y., Wang, J. *J. Am. Ceram. Soc*. **2012**. 95. *4*. 1241-1246.

16. Jiang, G., Zhou, C.H., Xia, X., Yang, F., Tong, D., Yu, W., Liu, S. *Mater Lett*. **2010**. 64. *24*. 2718-2721.

17. Zheng, X., Xu, J., Yan, K., Wang, H., Wang, Z. and Yang, S. *Chem. Mater*. **2014**. 26. *7*. 2344-2353.

18. Nagamatsu, J., Nakagawa, N., Muranaka, T., Zenitani, Y. Akimitsu, J. *Nature*. **2010**. 410. *6824*. 63-64.

19. Fahrenholtz, W.G., Hilmas, G.E., Talmy, I.G., Zaykoski, J.A. *J. Am. Ceram. Soc.* **2007**. 90. *5*. 1347-1364.

20. Gou, H., Wang, Z., Zhang, J., Yan, S.,Gao, F. *Inorg. Chem*. **2008**. 48. *2*. 581-587.

21. Lafferty, J.M. *J. Appl. Phys.* **1951**. 22. *3*. 299-309.

22. Lundstrom, T. *Pure Appl. Chem*. **1985**. 57. *10*. 1383-1390.11

23. Mitterer, C. *J. Solid State Chem.* **1997**. *1*. 279-291.

24. Hasegawa, A. Yanase, A. *J. Phys. C: Solid State Phys*. **1979**. 12. *24*. 5431.

25. Secrist, D.R. *J. Am. Ceram. Soc*. **1967**. 50. *10*. 520-523.

26. Serebryakova, T.I., Lyashenko, V.I. Levandovskii, V.D. Powder Metall. Met. C+. **1995**. 33. *1-2*. 49-53.

27. Vojteer, N., Stauffer, J., Hillebrecht, H., Hofmann, K., Panda, M., Albert, B. *Z. Anorg. Allg. Chem*. **2009**. 635. *4-5*. 653-659.

28. Mair, G., Nesper, R., Von Schnering, H.G. *J. Solid State Chem*. **1988**. 75. *1*. 30-40.

29. Mair, G., von Schnering, H.G., Wörle, M. *Z. Anorg. Allg. Chem*. **1999**. 625. *7*. 1207-1211.

30. Cao, M.; Hu, C.; Wang, E. *J. Am. Chem. Soc*. **2003.** 125. 11196−11197.

31. Rü diger, S.; Groß, U.; Kemnitz, E. *J. Fluorine Chem*. **2007**. 128. 353− 368.

32. Hua, R.; Zang, C.; Shao, C.; Xie, D.; Shi, C. *Nanotechnol.* **2003**. 14. 588−591.

33. Mao, Y.; Zhang, F.; Wong, S. S. *Adv. Mater*. **2006**. 18. 1895−1899

34. Dong, N. N.; Pedroni, M.; Piccinelli, F.; Conti, G.; Sbarbati, A.; Ramirez-Hernandez, J. E.; Maestro, L. M.; Iglesias-de la Cruz, M. C.; Sanz-Rodriguez, F.; Juarranz, A.; Chen, F.; Vetrone, F.; Capobianco, J. A.; Sole, J. G.; Bettinelli, M.; Jaque, D.; Speghini, A. *ACS Nano*. **2011**. 5. 8665−8671.

35. Li, C.; Lin, J. *J. Mater. Chem*. **2010**. 20. 6831−6847.

36. Lucca, A.; Debourg, G.; Jacquemet, M.; Druon, F.; Balembois, F.; Georges, P.; Camy, P.; Doualan, J. L.; Moncorge, R. *Opt. Lett*. 2004. *29*. 2767−2769.

37. Fedorov, P. P.; Luginina, A. A.; Kuznetsov, S. V.; Osiko, V. V. *J. Fluorine Chem*. **2011**. 132. 1012−1039.

38. Rehmer, A.; Scheurell, K.; Kemnitz, E. *J. Mater. Chem. C*. **2015**. *3*. 1716−1723.

39. Li, C.; Lin, J. *J. Mater. Chem*. **2010**. 20. 6831−6847.

40. Wö hler, F. *Justus Liebigs Ann. Chem*. **1863**. 127. 257−274.

41. Weiss, A.; Beil, G.; Meyer, H. *J. Chem. Sci*. **1980**. 35. 25−30.

42. Dahn, J. R.; Way, B. M.; Fuller, E.; Tse, J. S. *Phys. Rev. B: Condens. Matter Mater. Phys*. **1993**. 48. 17872−17877.

43. Vogg, G.; Brandt, M. S.; Stutzmann, M. *Chem. Mater*. **2003**. *15*. 910−915.

44. Nakano, H.; Ishii, M.; Nakamura, H. *Chem. Commun*. **2005**. 23. 2945−2947.

45. Brandt, M. S.; Vogg, G.; Stutzmann, M., John Wiley & Sons: Weinheim, Germany, 2007; pp 194− 199.

46. Kleewein, A.; Patzold, U.; Hengge, E.; Tasch, S.; Leising, G., Auner, N., Weis, J., Eds.; Wiley: Weinheim, Germany, 2008; pp 327−332.

47. Hoenle, W.; Dettlaff-Weglikowska, S.; Molassioti-Dohms, A.; Weber, J. Vieweg: Braunschweig, Germany, 1996; pp 99−116

48. Oh, S. Y.; Imagawa, H.; Itahara, H. *Chem. - Asian J*. **2014**. *9*. 3130−3135.

49. Imagawa, H.; Takahashi, N.; Nonaka, T.; Kato, Y.; Nishikawa, K.; Itahara, H. *J. Mater. Chem. A*. **2015**. 3. 9411−9414.

50. Yaokawa, R.; Ohsuna, T.; Morishita, T.; Hayasaka, Y.; Spencer, M. J.; Nakano, H. *Nat. Commun*. **2016.** *7*. 10657.

CHAPTER 2

LITHATION AND NANOSTRUCTURING OF STRONTIUM HEXABORIDE

Roshini Ramachandran and Tina T. Salguero. To be submitted to *Chemistry of Materials*.

Abstract

We have converted bulk strontium hexaboride into nanoparticles using a novel approach aimed at the disassembly of the crystal structure. We used a lithium ion incorporation technique to form a solid solution of Li_xSrB_6. After lithation, Li_xSrB_6 was structurally characterized using powder x-ray diffraction, multinuclear solid-state nuclear magnetic resonance spectroscopy and scanning electron microscopy. Li_xSrB_6 was then nanostructured by subsequently treating with deionized water to remove the incorporated lithium ions and produce a disassembly of the structure. Upon disassembly, SrB_6 formed an abundance of nanoparticles with particle sizes between 15-25 nm. Powder x-ray diffraction, multinuclear solid-state nuclear magnetic resonance spectroscopy, and transmission electron microscopy were used to characterize the morphology and composition of the nano strontium hexaboride. Effects on the morphology of the Li_xSrB_6 were investigated as a function of reaction time, reaction temperature and stirring rate.

Introduction

Metal borides are a well-known class of high performance refractory materials that have incredibly high melting points and exhibit good thermal stability, chemically inertness and excellent hardness.[1] Several metal borides possess other extraordinary properties; metal-rich UHTC's ZrB_2 and HfB_2 are leading candidates for hypersonic applications whereas boron-rich LaB_6 and CeB_6 have the highest electron emissivities known and are used as robust cathodes.[2-4] The high performance properties of metal borides arise from the 2D and 3D boron frameworks existing within the crystal structures of various subclasses of borides.[3] Even though metal borides have exceptional properties, their industrial use is limited due to their difficulty in being processed. Their high melting points make it challenging to convert them into thin films for coating applications.[4,5]

To improve their processability, nanostructuring of metal borides has been attempted using various techniques such as co-precipitation, pyrolysis, solid-state and vapor deposition methods.[7-25] However, a top-down approach to nanostructure metal borides remains unexplored. Converting metal borides into the nanoscale would open up a wide range of processing options; colloidal nanoparticle suspensions can be fabricated into thin films using simple spray deposition techniques instead of using conventional vapor deposition coating methods.

The strong covalent and ionic bonding existing in metal borides' frameworks make their exfoliation challenging. Therefore, typical conditions such as sonication and micromechanical cleavage cannot be applied to the metal borides. We employed a novel top-down exfoliation approach to strontium hexaboride aimed at the disassembly of the MB_6 structure. Our innovative synthetic methodology utilizes a lithium ion incorporation reaction that inserts lithium ions into the metal boride lattice to form a Li_xSrB_6 intermediate which is then subjected to disassembly.

Experimental

Materials: Strontium hexaboride (powder, Office of Naval Research, USA), 11 M *n*-butyllithium in hexanes (Sigma-Aldrich), hexanes (≥98.5%, Fisher).

Reaction of Strontium Hexaboride with *n*-Butyllithium:

All the following manipulations were conducted in an argon-filled glove box. 0.10 g (7.0 mmol) of SrB_6 powder was placed in a glass vial with teflon lined cap equipped with a Teflon stir bar. 2 mL of 11 M *n*-butyllithium (10.6 mmol) and 1 mL of anhydrous hexane was added to the vial. The vial was sealed with Parafilm M® and placed in a beaker filled with metallic thermal beads for uniform heating. The reaction was then left stirring at 300 rpm at 65 $^{\circ}$C for 11 days. Then the reaction mixture was vacuum filtered, and the isolated solids were washed twice with 20 mL hexane each time to remove any residual *n*-butyllithium. The lithiated SrB_6 powder was dried overnight to provide 0.09 g of a pale blue-grey powder (78.40% isolated yield).

Strontium Hexaboride Heated in Hexane (Control Experiment):

All the following manipulations were conducted in an argon-filled glove box. 0.10 g (7.0 mmol) of SrB_6 powder was placed in a glass vial equipped with a Teflon stir bar and 1 mL of anhydrous hexane was added to the vial. The vial was sealed with Parafilm M® and placed in a beaker filled with metallic thermal beads for uniform heating. The reaction was then left stirring at 300 rpm at 65 $^{\circ}$C for a period of 11 days. After 11 days, the reaction mixture was vacuum filtered, washed twice with 20 mL hexane each time and the isolated solids were dried overnight to provide 0.094 g of a dark grey powder (94% isolated yield).

Reaction of Lithiated Strontium Hexaboride with Water:

0.07 g of the lithiated strontium hexaboride (Li_xSrB_6) powder was treated with 20 mL of deionized water kept in an ice bath for 20 minutes. The product mixture was centrifuged and decanted to remove soluble byproduct LiOH. The solid product was washed and subjected to another cycle of centrifugation/decanting. The residual product was then re-dispersed in water and probe sonicated (Misonix S-4000 Ultrasonic Liquid Processor) at 60 amp for 1 hour. The nano product was dried overnight in a vacuum oven to provide 0.04 g of a fluffy, dark grey powder (59.79% isolated yield).

Characterization Details:

The composition of the bulk, lithiated and nano SrB_6 materials was confirmed using a Bruker D8- Advance powder X-ray diffractometer (Co-Kα radiation source) operated at 40 mA and 40 kV at a scanning rate of 0.3 sec $step^{-1}$. The morphology of the bulk and lithiated SrB_6 were examined using a FEI Inspect F field emission gun scanning electron microscope (FEG-SEM) operating at 20 kV and a FEI Teneo FEG-SEM with an Oxford EDS system operated at 5-10 keV. The bulk and lithiated samples were prepared for SEM by sprinkling the powders on carbon sticky tape. The morphology of the exfoliated nanoproducts were characterized using a FEI Tecnai 20 (200 kV) TEM with SAED capability.

Solid-state NMR data were collected with a Bruker Avance III 400 spectrometer operating at 10000 Hz. The instrument was calibrated for ^{7}Li, ^{11}B and ^{139}La NMR spectroscopy using aqueous solutions of lithium chloride, boric acid and lanthanum chloride respectively. Spectral deconvolution was performed using the SpinWorks4 software.

Results and Discussion

We treated bulk strontium hexaboride with an *n*-BuLi reaction at 80 ^{o}C and isolated the lithiated SrB_6. On observing the lithiated SrB_6, we noticed a color change from the dull grey-black color of SrB_6 to a light blue-grey (Figure 2.1). We attribute this to the formation of strontium-deficient SrB_6 under these reaction conditions.[3, 26-27]

We characterized the lithiated SrB_6 using powder x-ray diffraction (PXRD) and solid-state nuclear magnetic resonance spectroscopy (NMR) to obtain insight into the mechanism of lithium incorporation. ^{7}Li NMR experiment showed a peak at 0.10 ppm signifying the presence of Li in the lithiated SrB_6 (Figure 2.2 B). This indicates that the lithiation reaction was successful in incorporating Li^{+} ions within the SrB_6 lattice. We also measured ^{7}Li NMR shifts for common lithium side products for comparison (Figure 2.3), none of them match the new peak we observed in the lithiated SrB_6 sample. Solid-state NMR spectroscopy also showed a large change of 100 ppm in the ^{11}B chemical shift (Figure 2.2 A, 2.2 C) between the bulk SrB_6 and lithiated SrB_6 informing us that there was a drastic transformation in the chemical environment of the boron octahedra framework upon lithation. The asymmetry of the peaks in the ^{11}B spectra arises due to ^{11}B being a quadruploar nucleus with spin of 3/2.[28] This was consistently observed as a shoulder peak in all the ^{11}B spectra.

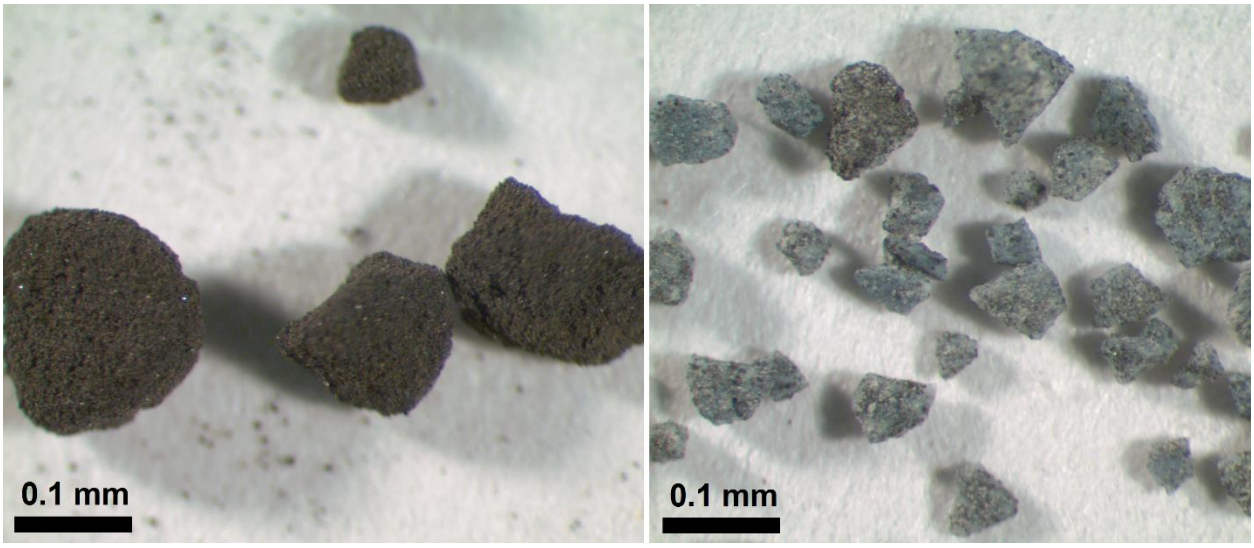

Figure 2.1: Optical images of bulk SrB_6 (left) and lithiated SrB_6 (right)

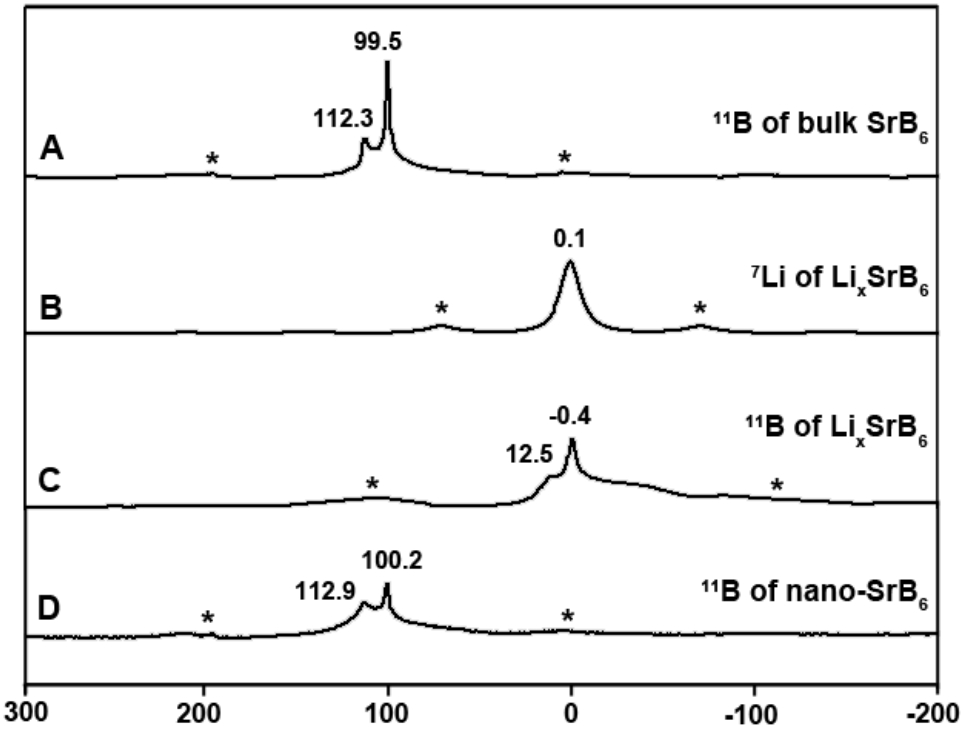

Figure 2.2. Solid-state NMR spectroscopy A) ^{11}B NMR on bulk SrB_6 B) ^{7}Li NMR on lithiated SrB_6 C) ^{11}B NMR on lithiated SrB_6 D) ^{11}B NMR on nano SrB_6 (* denotes spinning side bands)

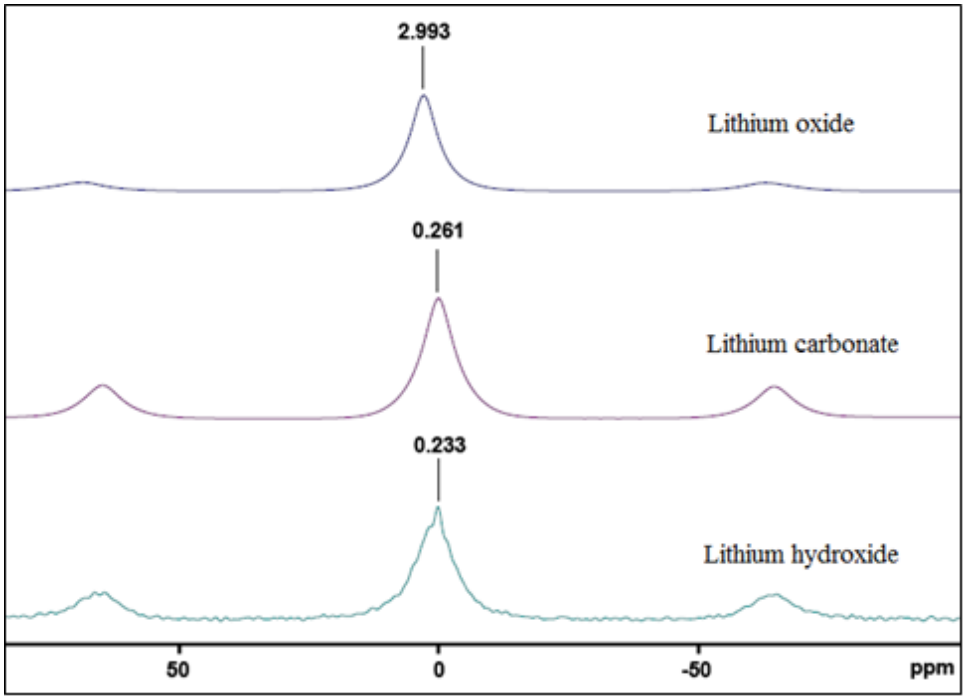

Figure 2.3: ^{7}Li solid state NMR spectra of lithium side products as standards

PXRD on the lithiated SrB_6 showed peak broadening and a large degree of peak 'splitting' that indicates the presence of two similar phases (Figure 2.4). This new phase can be attributed to a dilithium hexaboride species Li_2B_6, which has a crystal structure very similar to SrB_6.[29] Due to the mobility of Li^+ ions in the structure,[29] the lithiation reaction incorporates Li^+ into the SrB_6 crystal lattice to form a stable Li_2B_6-SrB_6 solid solution. We hypothesize that the Li^+ ions occupy the large spaces between the boron octahedra of SrB_6, which is plausible due to the similarities in crystal structure. In both hexaborides, the boron atoms form octahedral frameworks; however, in Li_2B_6, the B_6 octahedra are slightly twisted in the (001) plane to accommodate two lithium atoms.[29] Therefore, Li_2B_6 has a tetragonal crystal structure instead of the typical cubic MB_6 structure.[29]

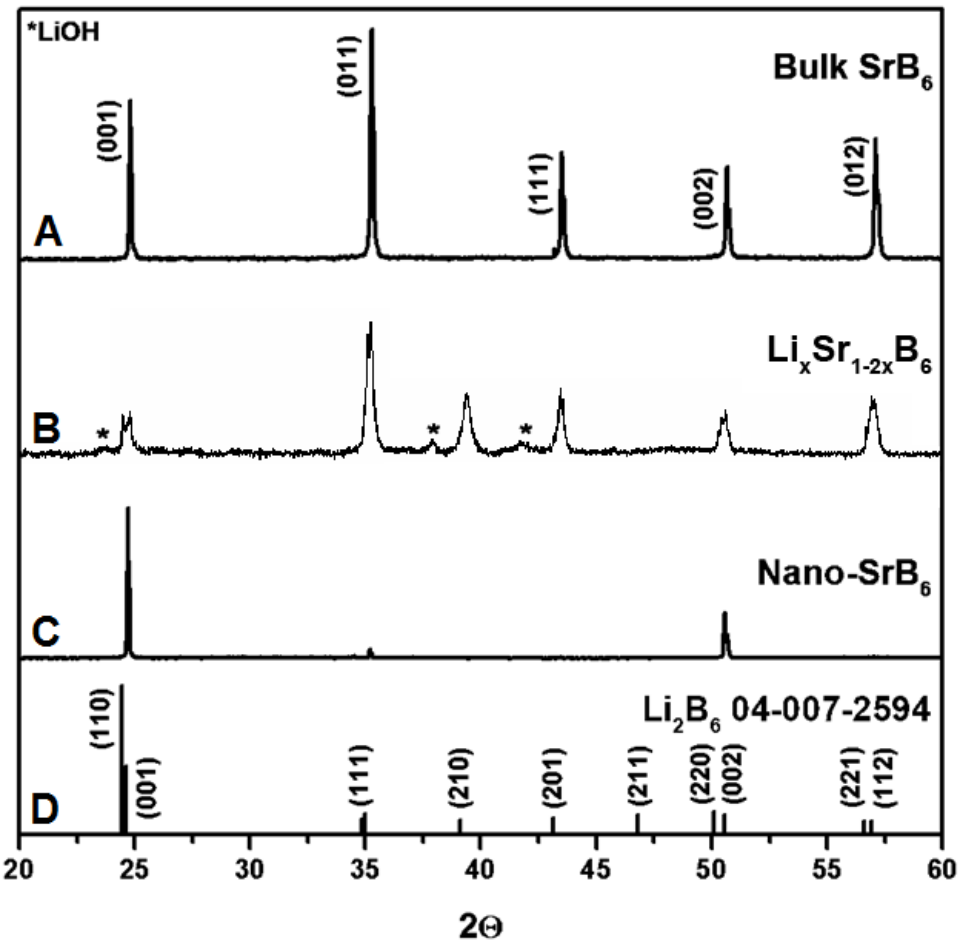

Figure 2.4. Powder x-ray diffraction patterns of nano, lithiated SrB_6 and bulk SrB_6 with reference pattern for LiB_3 (ICDD no. 04-00-2594)

High resolution synchrotron x-ray diffraction on the lithiated SrB_6 gave us a better resolution of the SrB_6 and Li_2B_6 peaks (Figure 2.5). Zoom in of the individual peaks further confirmed the presence of both phases. The lithiated SrB_6 is air-sensitive, over time it leads to the formation of various side products, as can be seen in the synchrotron XRD pattern.

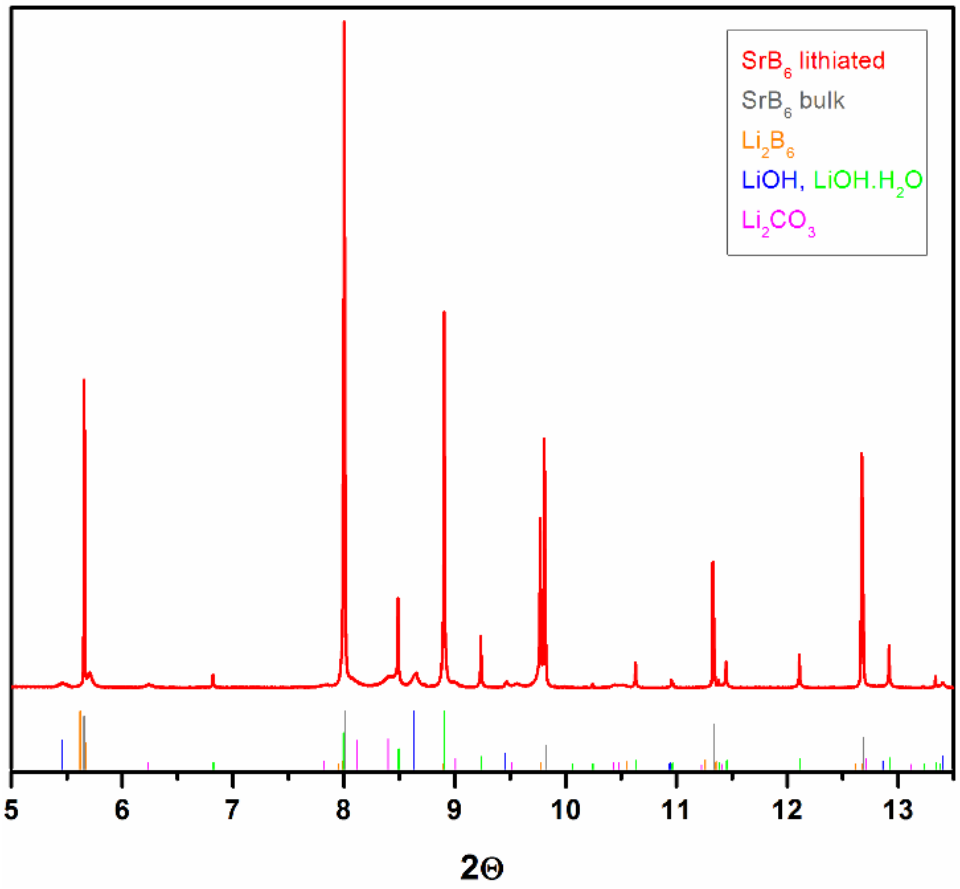

Figure 2.5. Synchrotron powder x-ray diffraction patterns of lithiated SrB_6 reference pattern for SrB_6, LiB_3 (ICDD no. 04-007-2594), LiOH (ICDD no. 00-001-1021), $LiOH{\cdot}H_2O$ (ICDD no. 00-025-0486) and Li_2CO_3 (ICDD no. 00-009-0359)

Observing and comparing the bulk and lithiated SrB_6 powders under scanning electron microscopy (SEM), it is evident that the lithiation is accompanied by a morphological change (Figure 2.6). Bulk SrB_6 powder is composed of clusters of large platelets (Figure 2.6 A) whereas the the particle size is decreased in the lithiated SrB_6 powder which comprises clusters of nanoparticles of less than a micron in lateral dimensions and hollow spheres of sizes ranging

between 3-5 microns (Figure 2.6 B). EDS mapping on the lithiated SrB_6 confirmed the presence of Sr, B and surface O (Figure 2.6 D-F respectively).

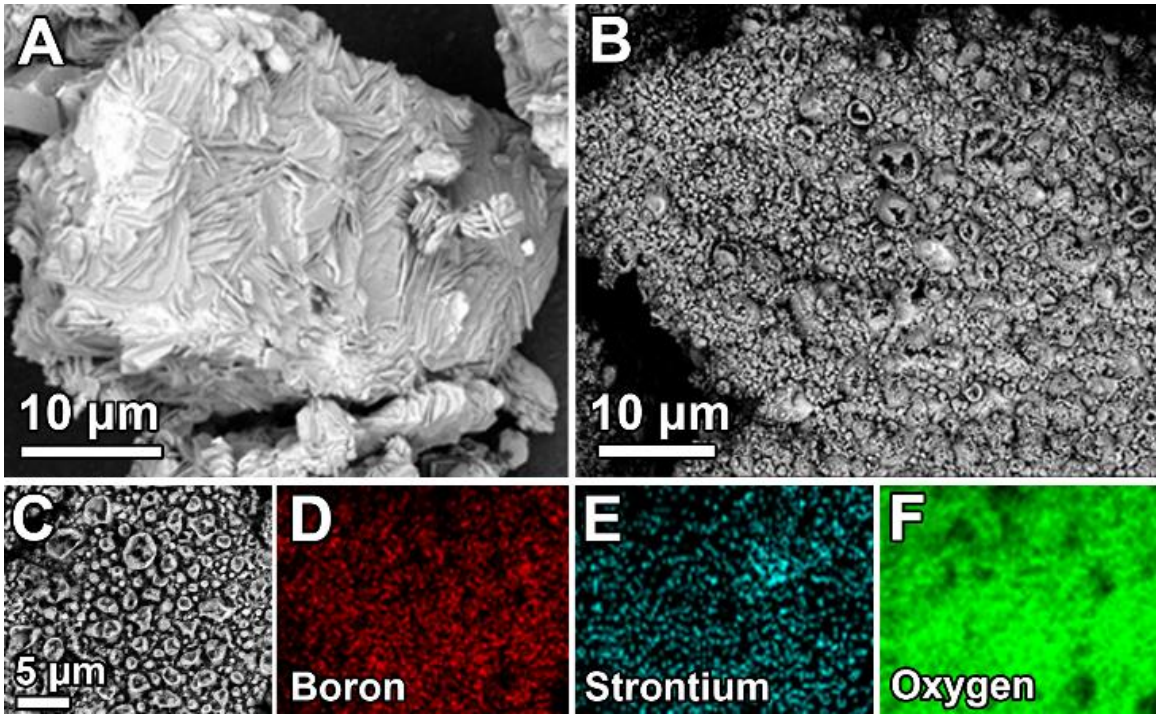

Figure 2.6. A) SEM image of bulk SrB_6 B) SEM image of lithiated SrB_6 C) Higher magnification SEM image of lithiated SrB_6 D-F) Elemental mapping of Boron, Strontium and Oxygen respectively

The next step in our nanostructuring process was to react lithiated SrB_6 with deionized water. This removes the lithium ions as lithium hydroxide through a highly vigorous and exothermic reaction possibly accompanied by H_2 evolution. The lithium hydroxide further converts to lithium carbonate under ambient conditions. Microcrystalline dilithium hexaboride is

water-sensitive[29], therefore, this "exfoliation" reaction causes a disassembly of the MB_6 structure, and is enhanced with a subsequent ultrasonication step.

Observing the exfoliated product using transmission electron microscopy (TEM) disclosed that the exfoliated SrB_6 product is very representative of the morphology we had seen in the lithiated SrB_6 powder. The nanoproduct consists of clusters of nanoparticles of size 15-25 nm (Figure 2.7 A, Figure 2.8). SAED on the nanoparticles shows polycrystalline rings indexed to SrB_6 (Figure 2.7 B). Analyzing the SrB_6 nanoparticles using PXRD shows a pattern matching that of bulk SrB_6, the absence of two phases further confirms that there is no dilithium hexaboride remaining (Figure 2.3). We do observe orientation effects in the PXRD pattern of nano SrB_6 with some peaks having a much higher intensity, particularly the (00l) series is expressed more strongly. This is because of the nanoparticles being oriented along that plane, thus producing a stronger XRD signal for the (00l) series.[30]

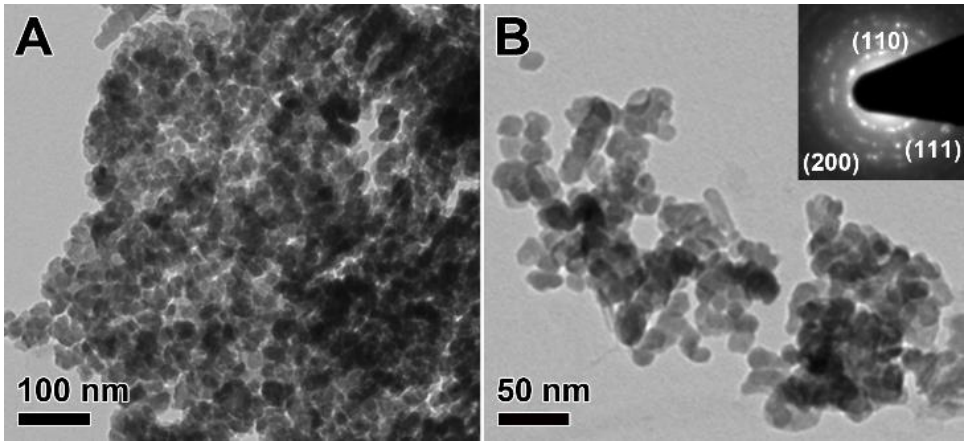

Figure 2.7. A) TEM image of a cluster of SrB_6 nanoparticles B) TEM image of individual particles with inset SAED pattern indexed to SrB_6

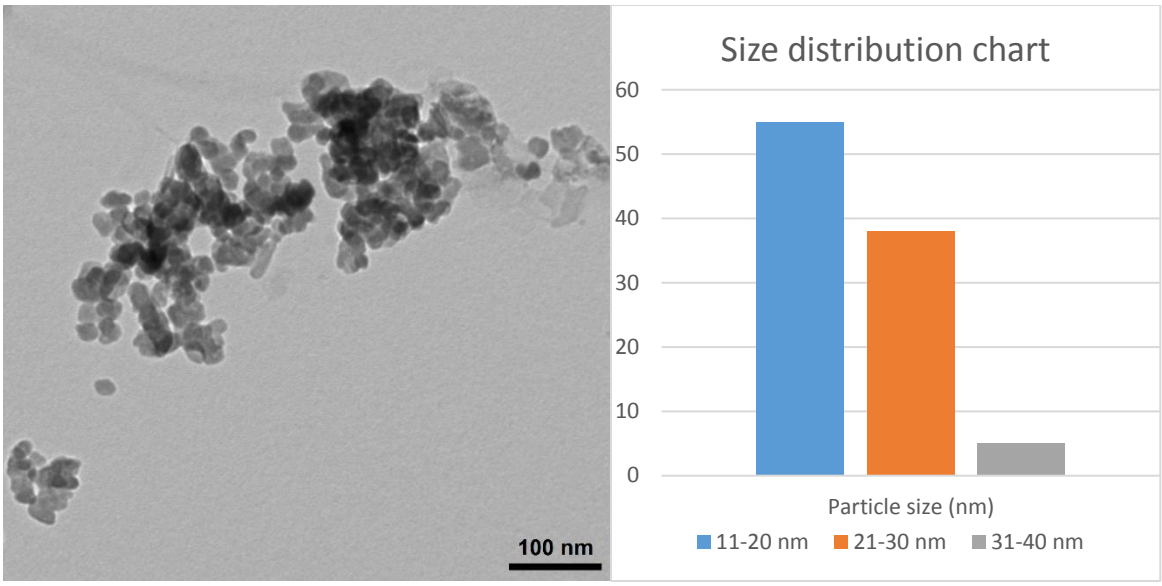

Figure 2.8. TEM image of nano SrB_6 with mean particle size of 20.39 nm

Performing ^{11}B NMR spectroscopy on nano SrB_6 shows a spectrum similar to that of bulk SrB_6 (Figure 2.2 D, 2.2 A) indicating that the boron environment has returned to that of the starting material. PXRD on the dried supernatant liquid confirms the presence of byproducts LiOH and Li_2CO_3 confirming our reaction mechanism hypothesis that lithium is removed from the structure on treatment with water (Figure 2.9).

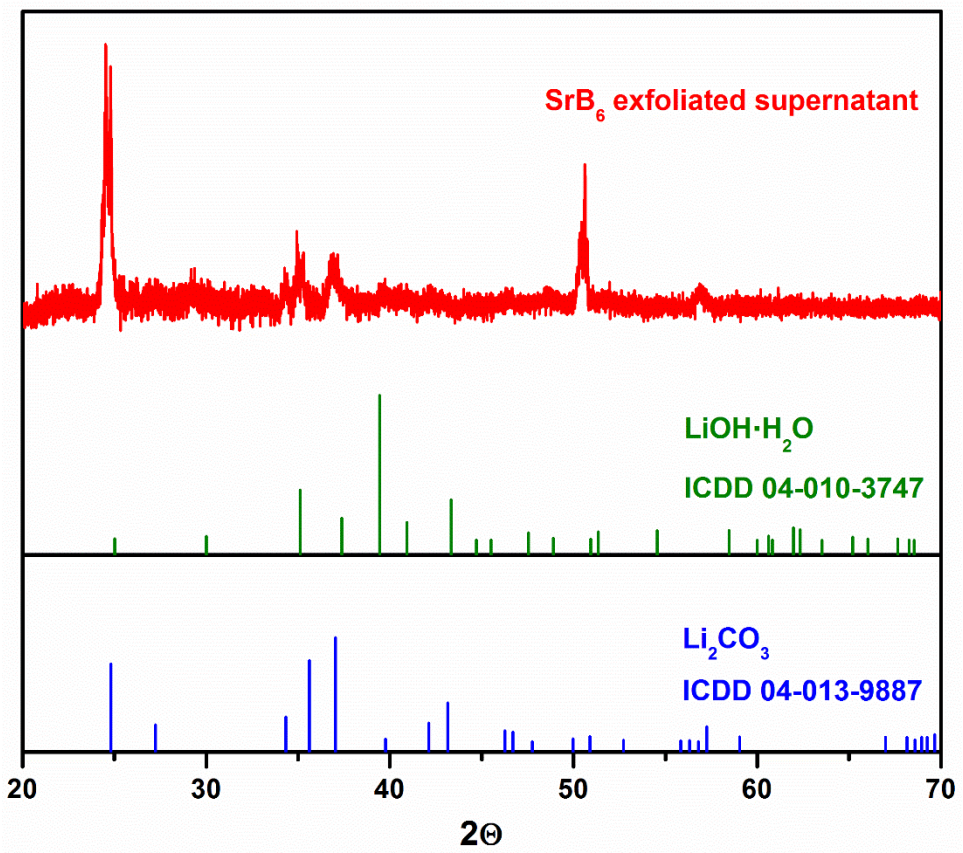

Figure 2.9. PXRD on the supernatant liquid from the reaction of lithiated SrB_6 with water.

These SrB_6 nanoparticles can get partially oxidized to strontium hydroxide and strontium carbonate over a period of a few days when stored in water due to their small size and high surface area with no observable change in morphology (Figure 2.10). Partial or complete oxidation of nanostructured metal hexaborides has been previously observed for other morphologies.[31,32]

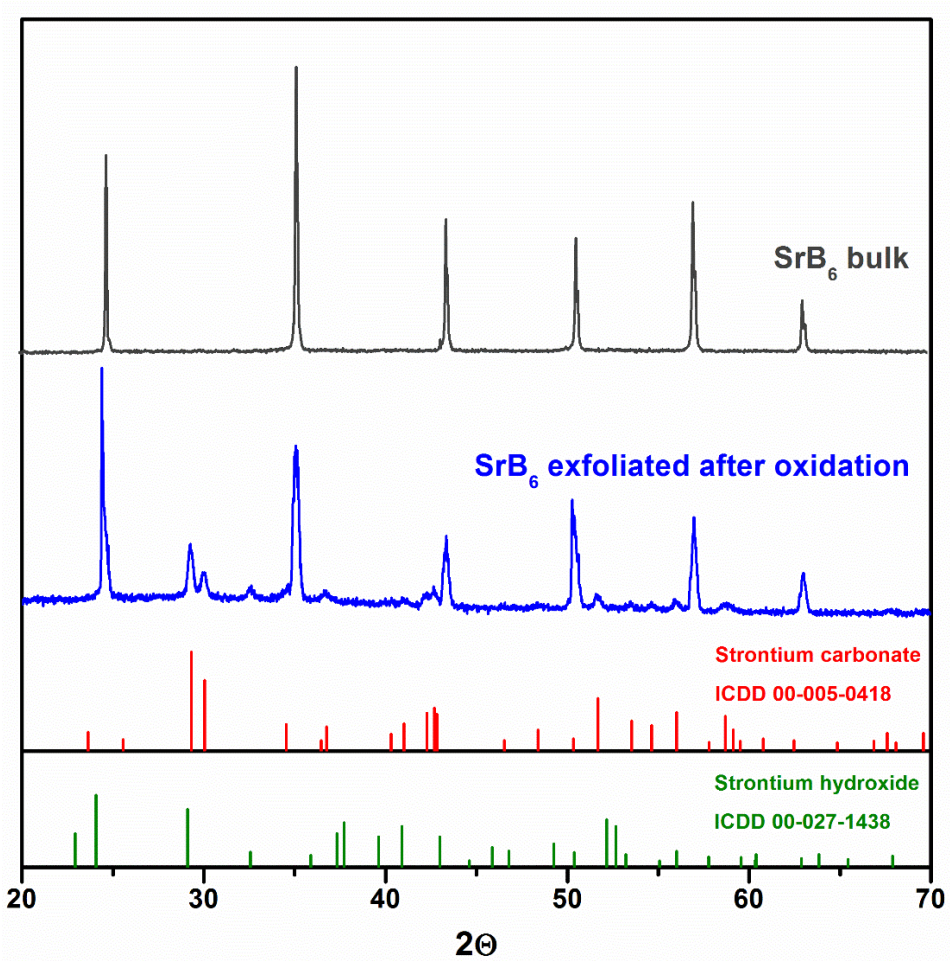

Figure 2.10. PXRD on SrB_6 nanoparticles after storing in water at room temperature for one week

To further confirm that the lithium incorporation was indeed responsible for the exfoliation of SrB_6, we performed a control reaction in hexane which yielded no nanoproduct. We observed the product under SEM which showed no observable change in the surface morphology. (Figure 2.11).

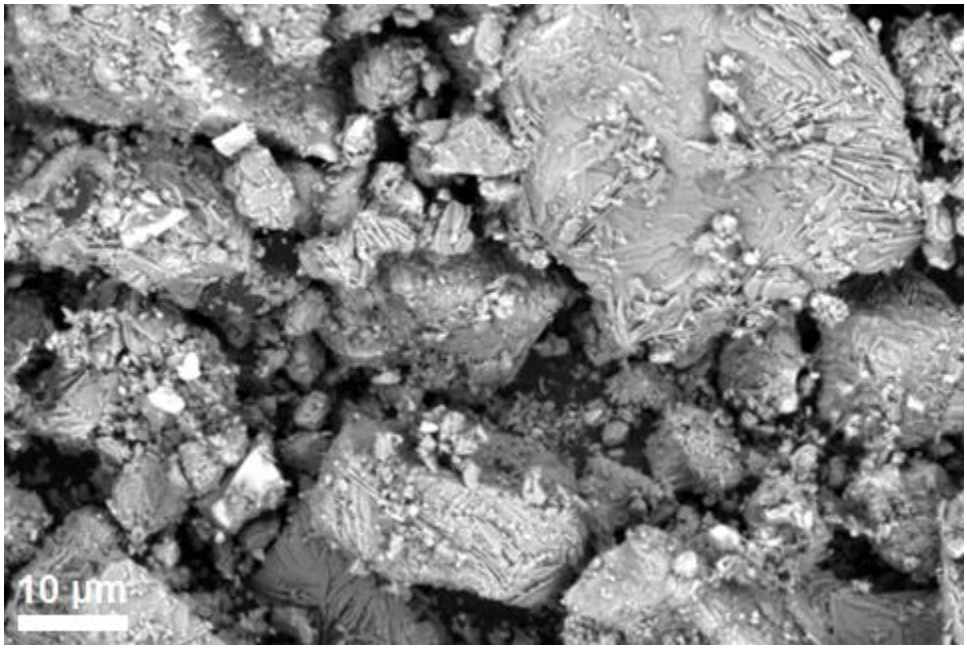

Figure 2.11. SEM of SrB_6 product from a control reaction of SrB_6 in hexane

Performing the lithiation reaction at room temperature did not produce any exfoliation of SrB_6, however the presence of dilithium hexaboride could be detected by PXRD (Figure 2.12). SEM on the room temperature lithiated SrB_6 showed the presence of platelets and particles (Figure 2.13).

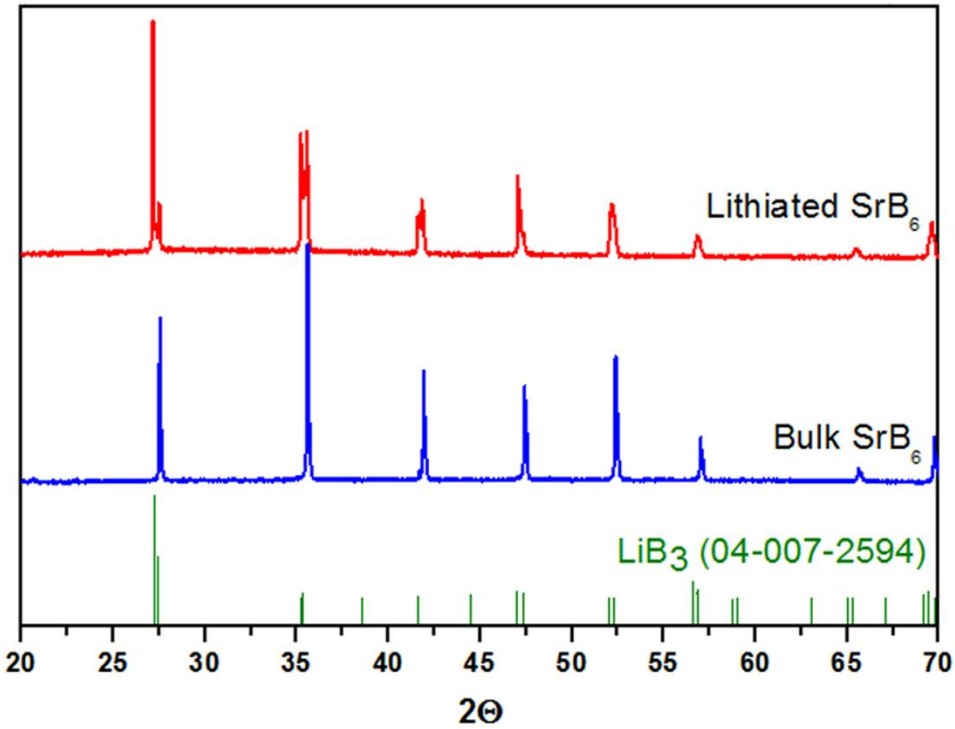

Figure 2.12. PXRD on lithiated SrB_6 obtained from *n*-BuLi reaction at room temperature

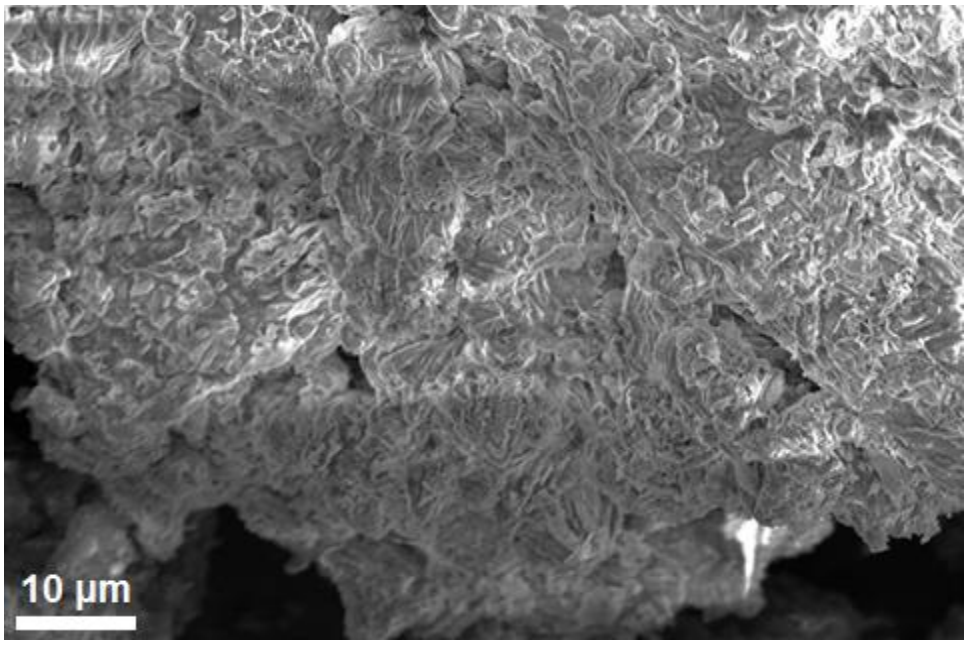

Figure 2.13. SEM on lithiated SrB_6 obtained from *n*-BuLi reaction at room temperature

We further performed the *n*-BuLi reaction at 80 ^{o}C on SrB_6 in the absence of stirring. Observing the lithiated product under SEM showed us that the non-uniform stirring led to partial nanostructuring in SrB_6, both partially disintegrated platelets and nanoparticle clusters were clearly visible (Figure 2.14).

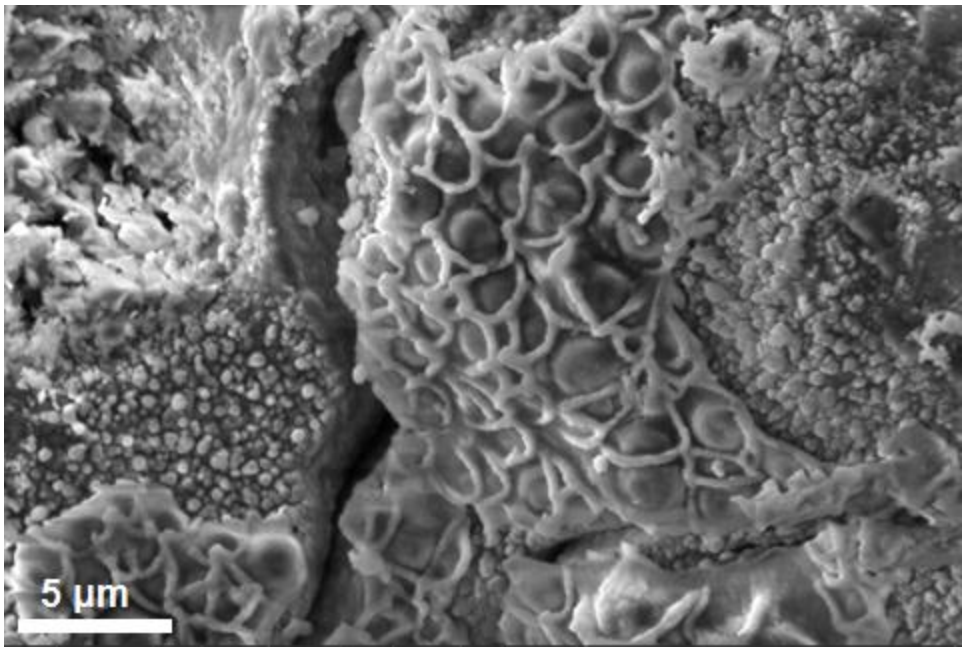

Figure 2.14. SEM image on lithiated SrB_6 obtained from *n*-BuLi reaction without stirring

We performed a time study; reducing the reaction time to one day did not produce any change in morphology of the lithiated SrB_6. Doing the reaction for 4 days did not yield a nanoproduct on exfoliation, however, we observed small nanoparticles beginning to form on the surface of the lithiated SrB_6.

Table 2.1. Literature values for ^{7}Li NMR chemical shifts of relevant lithium-containing compounds

Lithium compound	^{7}Li (ppm)	NMR technique	Reference
Li_2O	2.8	solid state	Meyer, B. M., Leifer, N., Sakamoto, S., Greenbaum, S. G., & Grey, C. P. "High field multinuclear NMR investigation of the SEI layer in lithium rechargeable batteries" *Electrochemical and solid-state letters* 8.3 (2005): A145-A148.
$LiOH{\bullet}H_2O$	0.4	solid state	
Li (metal)	258	solid state	Bhattacharyya, R., Key, B., Chen, H., Best, A. S., Hollenkamp, A. F., & Grey, C. P. "In situ NMR observation of the formation of metallic lithium microstructures in lithium batteries" *Nature materials* 9.6 (2010): 504-510.
LiH	1.5	solid state	Wang, Y., Guo, Z. X. "Enhanced hydrogen desorption of an ammonia borane and lithium hydride system through synthesised intermediate compounds" *Journal of Materials Chemistry A* (2014) 2 :6801-6813
$LiBH_4$	-2.7	solid state	Verkuijlen, M.H., Ngene, P., de Kort, D.W., Barré, C., Nale, A., van Eck, E.R., van Bentum, P.J.M., de Jongh, P.E. and Kentgens, A.P. "Nanoconfined $LiBH_4$ and enhanced mobility of Li^+ and BH_4^- studied by solid-state NMR" *The Journal of Physical Chemistry C* 116.42 (2012): 22169-22178.
phenyllithium	1.9	solid state	Pepels, A., Günther, H., Amoureux, J. P., & Fernandéz, C. "7Li Solid-State NMR of Organolithium Compounds: Dependence of 7Li Quadrupolar Coupling, χ (^{7}Li), on the Structural Angle C− Li− C" *Journal of the American Chemical Society* 122.40 (2000): 9858-9859.
	1.03	ether solution	Parker, J., and Ladd, J. A. "The ^{1}H and ^{7}Li magnetic resonance spectra of some aryllithiums" *Journal of Organometallic Chemistry* 19.1 (1969): 1-7.
n-butyllithium	-0.74	cyclopentane solution	Smart, J. B., Hogan, R., Scherr, P. A., Emerson, M. T., & Oliver, J. P. "Metal—double bond interactions: IV. A study of lithium—π-electron interactions in 3-butenyllithium by ^{7}Li and ^{1}H NMR spectroscopy" *Journal of Organometallic Chemistry* 64.1 (1974): 1-17.
	-1.53	ether solution	
ethyllithium	-0.77	cyclopentane solution	
	-1.52	ether solution	

Table 2.2. Literature values for ^{11}B NMR chemical shifts of relevant boron-containing compounds

Boron compound	**^{11}B (ppm)**	**NMR technique (standard)**	**Reference**
Li_2B_4O7	2.3 ± 0.1 18.2 ± 0.2	solid state	Hansen, M. R., Vosegaard, T., Jakobsen, H. J., & Skibsted, J. "^{11}B chemical shift anisotropies in borates from ^{11}B MAS, MQMAS, and single-crystal NMR spectroscopy" *The Journal of Physical Chemistry A* 108.4 (2004): 586-594.
B_2O_3	13.0 ± 1 18.1 ± 1.2	solid state	Youngman, R. E., and Zwanziger, J. W. "Multiple boron sites in borate glass detected with dynamic angle spinning nuclear magnetic resonance" *Journal of non-crystalline solids* 168.3 (1994): 293-297.
H_3BO_3 or $B(OH)_3$	19.1	solid state	Irwin, A. D., Holmgren, J. S., & Jonas, J. "Solid state ^{29}Si and ^{11}B NMR studies of sol-gel derived borosilicates" *Journal of non-crystalline solids*, 101.2(1988): 249-254.
HBO_2	2.0 13.0	solid state	Jimenez, M., Duquesne, S. and Bourbigot,S. "Intumescent fire protective coating: toward a better understanding of their mechanism of action" *Thermochimica acta* 449.1 (2006): 16-26.
α-rhombohedral B	48.0 −83.2	solid state	Lee, Donghoon, Philip J. Bray, and Terry L. Aselage. "The NQR and NMR studies of icosahedral borides" *Journal of Physics: Condensed Matter* 11.22 (1999): 4435.
β-rhombohedral B	14.2	solid state	Turner, C. L., Taylor, R. E. and Kaner, R. B. "^{10}B and ^{11}B NMR Study of Elemental Boron" *The Journal of Physical Chemistry C* 119.24 (2015): 13807-13813.
$LiBH_4$	-42.9	solid state	Verkuijlen, M.H., Ngene, P., de Kort, D.W., Barré, C., Nale, A., van Eck, E.R., van Bentum, P.J.M., de Jongh, P.E. and Kentgens, A.P. "Nanoconfined $LiBH_4$ and enhanced mobility of Li^+ and BH_4^-studied by solid-state NMR" *The Journal of Physical Chemistry C* 116.42 (2012): 22169-22178.
CaB_6	331 ± 9	solid state	Sears, R. E. J. "^{11}B chemical shifts and quadrupole coupling constants in the alkaline–earth hexaborides" *The Journal of Chemical Physics* 76.11 (1982): 5651-5652.
SrB_6	186 ± 14	solid state	
BaB_6	147 ± 10	solid state	
LaB_6	2	solid state	Ammar, A., Ménétrier, M., Villesuzanne, A., Matar, S., Chevalier, B., Etourneau, J., Villeneuve, G., Rodríguez-Carvajal, J., Koo, H.J., Smirnov, A.I. and Whangbo, M.H. "Investigation of the electronic and structural properties of potassium hexaboride, KB_6, by transport, magnetic susceptibility, EPR, and NMR measurements, temperature-dependent crystal structure determination, and electronic band structure calculations" *Inorganic chemistry* 43.16 (2004): 4974-4987.
KB_6	84	solid state	

Conclusions

We have nanostructured strontium hexaboride into nanoparticles using a novel lithium ion incorporation-exfoliation method. We incorporated lithium ions into the bulk strontium hexaboride structure to form Li_xSrB_6. After lithation, Li_xSrB_6 was structurally characterized using PXRD, multinuclear solid-state NMR and SEM/EDS. We detected the formation of a Li_2B_6 intermediate from PXRD and observed that lithiation is accompanied by a significant change in the ^{11}B chemical environments from NMR. Additionally, a morphological change was also observed in SrB_6 upon lithiation.

Li_xSrB_6 was disassembled to produce nanoparticles of SrB_6 nanoparticles which were characterized by PXRD, multinuclear solid-state NMR and TEM. It was shown that these nanoparticles retain the composition and structure of strontium hexaboride.

We observed that lowering the reaction temperature did not lead to a large extent of nanostructuring of SrB_6. Time study showed us that lower reactions times do not produce lithiation or nanostructuring. Performing the reaction without stirring led to the formation of pockets of nanostructuring which was due to partial lithiation. We optimized the reaction conditions to produce nanoparticles of SrB_6 that were between 15-20 nm in diameter, making this the first attempt at a top-down nanostructuring of metal hexaborides.

References

1. Mroz, C. *Am. Ceram. Soc. Bull.*, **1995**. *74*. 165–166
2. Chambers, S. A., Swanson, L. W. *Surf. Sci*. **1983**. 131. *2-3*. 385-402.
3. Lafferty, J.M. *J. Appl. Phys.* **1951**. 22. *3*. 299-309.
4. Lundström, T. *Pure Appl. Chem*. **1985**. 57. *10*. 1383-90.
5. Fahrenholtz, W. G., Hilmas, G. E., Talmy, I. G., & Zaykoski, J. A. *J. Am. Ceram. Soc.* **2007.** 90. *5*. 1347-1364.
6. Mitterer, C. *J. Solid State Chem.* **1997**. 133. *1*. 279-291.
7. Glavee, G. N., Klabunde, K. J., Sorensen, C. M., Hadjipanayis, G. C. *Langmuir*. **1993**. 9. *1*. 162-169.
8. T.T. Xu, J.G. Zheng, A.W. Nicholls, S. Stankovich, R.D. Piner, R.S. Ruoff. *Nano Lett.* **2004** 4. *10*. 2051-2055.
9. Zhang, H., Zhang, Q., Tang, J. Qin, L.C. *J.A.C.S.* **2005.** 127. *9*. 2862-2863.
10. Brewer, J.R., Deo, N., Wang, Y. M., Cheung, C.L. *Chem. Mater.* **2007**. 19. *26*. 6379-6381.
11. Xu. J., Zhao, Y., Zou, C., Ding. Q. *J. Solid State Chem.* **2007**. 180. 2577-2580.
12. Jash, P., Nicholls, A. W., Ruoff, R. S., Trenary, M. *Nano letters*. **2008.** 8. *11*. 3794-3798.
13. Selvan, R.K., Genish, I., Perelshtein, I., Calderon Moreno, J.M. and Gedanken, A. *J. Phys. Chem. C*. **2008**. 112. *6*.1795-1802.
14. Takeda, H., Kuno, H. and Adachi, K., *J.A.C.S*. **2008**. 91. *9*. 2897-2902.
15. Xu, J. Q., Zhao, Y. M., Ji, X. H., Zhang, Q., Lau. S. P. *J. Phys. D.* **2009**. 42. *13*. 135403.
16. Adachi, K., Miratsu, M., Asahi, T. *J. Mater. Res.* **2010**. 25. *3*. 510-521.
17. Zhou, S., Zhang, J., Liu, D., Lin, Z., Huang, Q., Bao, L., Ma, R. and Wei, Y. *Acta Mater*. **2010**. 58. *15*. 4978-4985.

18. Zhang, H., Tang, J., Yuan, J., Ma, J., Shinya, N., Nakajima, K., Murakami, H., Ohkubo, T., Qin, L.C. *Nano Lett.* **2010**. 10. *9*. 3539-3544.

19. Brewer, J.R., Jacobberger, R.M., Diercks, D.R., Cheung, C.L. *Chem. Mater.* **2011**. 23. *10*. 2606-2610.

20. Yuan, Y., Zhang, L., Liang, L., He, K., Liu, R., Min, G. *Ceram. Int*. **2011.** 37. *7*. 2891-2896.

21. Jha, M., Patra, R., Ghosh, S. Ganguli, A.K. *J. Mater. Chem.* **2012.** 22. *13*. 6356-6366.

22. Jha, M., Patra, R., Ghosh, S. Ganguli, A.K. *Solid State Commun.* **2013**. 153. *1*. 35-39.

23. Patra, R., Ghosh, S., Sheremet, E., Jha, M., Rodriguez, R. D., Lehmann, D., Ganguli, A. K., Gordan, O. D., Schmidt, H., Schulze, S., Zahn. D. R. T., *J. Appl. Phys.* **2014**. 115. *9*. 094302.

24. Ağaoğulları, D., Balcı, Ö., Öveçoğlu, M. L., Suryanarayana, C., Duman. İ. *J. Eur. Ceram. Soc.* **2015**. 35. *15*. 4121-4136.

25. Torabi, O., Naghibi, S., Golabgir, M. H., Jamshidi. A. J. *Chin. Chem. Soc.* **2016**. 63. *4*. 379-384.

26. Storms, E., Mueller. B. *J. Phys. Chem.* **1978**. 82. *1*. 51-59.

27. McKelvy, M. J., Eyring, L., Storms, E. K. *J. Phys. Chem.* **1984**. 88. *9*. 1785-1790.

28. Kroeker, S., Stebbins, J. F. *Inorg. Chem.* **2001**. 40. *24*. 6239-6246.

29. Mair, G., H. G. von Schnering, M. Wörle. *Z. Anorg. Allg. Chem.* **1999**. *625*. 1207–1211.

30. Brinzari, V., Korotcenkov, G., Golovanov, V., Schwank, J., Lantto, V., & Saukko, S. *Thin Solid Films.* **2002**. 408. *1*. 51-58.

31. Xu, T. T., Zheng, J. G., Nicholls, A. W., Stankovich, S., Piner, R. D., Ruoff, R. S. *Nano Lett*. **2004**. 4. 2051–2055

32. Machida, K., Okada, M., Yoshio, S., & Adachi, K. *J. Mater. Res.* **2016**. 1-9.

CHAPTER 3

LITHATION AND EXFOLIATION OF LANTHANUM HEXABORIDE

Roshini Ramachandran and Tina T. Salguero. To be submitted to *Journal of Materials Chemistry C*.

Abstract

We have exfoliated lanthanum hexaboride into nanosheets using a novel lithium ion incorporation-exfoliation method. This is the first account of a top-down exfoliation of metal borides. We used a lithium ion incorporation technique to lithiate bulk lanthanum hexaboride. After lithation, the lithiated intermediate ($Li_xLa_{1-x}B_6$) was structurally characterized using powder x-ray diffraction, multinuclear solid-state nuclear magnetic resonance spectroscopy and scanning electron microscopy. The lithiated lanthanum hexaboride $Li_xLa_{1-x}B_6$ was then exfoliated by subsequently treating with deionized water to remove the lithium ions incorporated and produce a disassembly of the structure. Upon exfoliation, LaB_6 formed uniform square-shaped nanosheets. Powder x-ray diffraction, multinuclear solid-state nuclear magnetic resonance spectroscopy, transmission electron microscopy and atomic force microscopy were used to characterize the morphology and composition of the exfoliated products obtained from lithiated lanthanum hexaboride. Effects on the morphology of the nanoproduct from factors such as grain size of the lanthanum hexaboride starting material, and duration of lithiation reaction were also investigated.

Introduction

Lanthanum hexaboride is a well-known metal boride due to its low work potential and high electron emissivity.[1-3] Owing to these properties, LaB_6 is widely used as cathode material in filaments of electron microscopes, microwave tubes, electron guns, X-ray tubes and free electron lasers.[1-2] Currently, thin films of lanthanum hexaboride are fabricated utilizing physical and chemical vapor deposition, but the drawback to these techniques is that we have little control over the thickness and uniformity of the coating formed.[4,5]

Converting bulk lanthanum hexaboride into nanosheets would open up a wide range of processing options. Since nanosheets have a tendency to lay flat, self-assemble by stacking, and easily form thin films, they serve as a junction between nanoscale and macroscale regimes.[6] Nanosheets stay suspended colloidally in water and other solvents over long periods of time. We can use simple techniques such as spray deposition, dip coating or inkjet printing to apply them on surfaces. Various bottom-up synthetic techniques using solid-state, templated growth and vapor deposition processes have been utilized to nanostructure lanthanum hexaboride.[7-16] However, a top-down exfoliation into nanosheets remains unexplored because the strong covalent and ionic bonding existing in the boron frameworks of LaB_6 make the exfoliation challenging. Another motivation for nanostructuring LaB_6 is the exhibition of strong NIR-absorption properties by nanoscale LaB_6, arising due to localized surface plasmon resonance effects.[17,18]

In this work, we have employed a novel top-down lithium ion insertion-exfoliation approach to lanthanum hexaboride aimed at the disassembly of the LaB_6 structure. Our innovative synthetic methodology utilizes a lithium ion incorporation reaction that inserts lithium ions into the metal boride lattice to form a “lithiated LaB_6 intermediate”. We used two different types of lithiation reactions that led to the formation of different nanoproducts under these conditions.

Experimental

Materials: Lanthanum hexaboride (99.9% powder, Sigma Aldrich), lanthanum hexaboride nanopowder (99.9%, US nano), lanthanum hexaboride single crystal (Applied Physics Technology), 11 M *n*-butyllithium in hexanes (Sigma Aldrich), lithium ribbon (99.9%, Sigma Aldrich), hexanes (≥98.5%, Fisher), anhydrous ammonia (99.99%, Airgas)

Lithiation reactions:

1. Reaction of lanthanum hexaboride with Li/NH_3

0.2 g (0.001 moles) of LaB_6 powder and 0.1 g Li (0.014 moles) were placed in a modified Schlenk vessel with Teflon cap. The Schlenk vessel was kept in an ethanol bath equipped with temperature probe maintained at -50 ^{o}C. The reaction vessel was pumped down to 5 mbar using a diffusion pump. Once the ethanol bath reached -50 ^{o}C, the pump was switched off and 60 mL of ammonia gas was slowly condensed into the vessel. The LaB_6 powder is left sitting in the Li/NH_3 solution for 4 days, after which the NH_3 gas is evaporated off into dil HCl solution. The product is washed with liquid NH_3 two or three times to remove any remaining elemental lithium and then the reaction vessel is flushed with argon gas, pumped down to remove any remaining gas and taken into an argon glove box. The lithiated LaB_6 powder ($Li_xLa_{2-x}B_6$) is removed from the Schlenk vessel and stored in the argon glove box pending future characterization.

2. Reaction of lanthanum hexaboride with NH_3 (control)

0.2 g (0.001 moles) of LaB_6 powder was placed in a modified Schlenk vessel with Teflon cap. The Schlenk vessel was kept in an ethanol bath equipped with temperature probe maintained at -50 ^oC. The reaction vessel was pumped down upto 5 mbar using a diffusion pump. Once the ethanol bath reached -50 ^oC, the pump was switched off and 60 mL of ammonia gas was slowly condensed into the vessel. The LaB_6 powder is left sitting in liquid NH_3 for 4 days, after which the NH_3 gas is evaporated off into dil HCl solution. The reaction vessel is flushed with argon gas, pumped down and taken into an argon glove box. The LaB_6 powder is removed from the Schlenk vessel and stored in the argon glove box pending future characterization.

3. Reaction of lanthanum hexaboride with *n*-butyllithium at high temperature

The following manipulations were carried out in an argon glove box. 0.1 g (0.0005 moles) of LaB_6 powder was placed in a glass vial equipped with a Teflon stir bar. 2 mL of 11 M *n*-butyllithium and 1 mL of anhydrous hexane was added to the vial. The vial was sealed with parafilm and placed in a beaker filled with metallic thermal beads for uniform heating. The reaction was then left stirring at 300 rpm at 65 ^oC for a period of 11 days. After 11 days, the reaction mixture was filtered using a vacuum filtration setup and the filtered powder was washed twice with hexane to remove any remaining *n*-butyllithium. The lithiated LaB_6 powder ($Li_xLa_{2-x}B_6$) was dried overnight and stored under inert conditions.

Reaction of $Li_xLa_{2-x}B_6$ with water (exfoliation):

The $Li_xLa_{2-x}B_6$ powder was treated with 20 mL of deionized water kept in an ice bath. The product mixture was centrifuged and decanted to remove the soluble byproduct LiOH. The solid product was washed and subjected to another cycle of centrifugation and decanting. The residual product was then re-dispersed in water and probe sonicated at 60 amp for 1 hour. The subsequent exfoliated product was vacuum dried or stored as a dispersion in water.

Characterization:

The composition of the bulk, lithiated and exfoliated materials was confirmed using a Bruker D8- Advance powder X-ray diffractometer (Co-Kα radiation source) operated at 40 mA and 40 kV. The PXRD patterns were recorded over the 2θ range of 5−80° with a scanning rate of 0.3 sec $step^{-1}$. The morphology of the $Li_xLa_{2-x}B_6$ and exfoliated products were examined using a FEI Teneo FEG-SEM with an Oxford EDS system operated at 5-10 keV. The lithiated samples were prepared for SEM by sprinkling the powders on carbon sticky tape while the exfoliated samples were dropcast on a silicon wafer. A Misonix S-4000 Ultrasonic Liquid Processor was used for the sonication step. The morphology of the exfoliated nanoproducts were characterized using a FEI Tecnai 20 (200 kV) TEM with SAED capability and a high resolution FEI Tecnai F30 Transmission TEM (300 kV). Atomic Force Miscroscopy (AFM) was determined using a Bruker Innova atomic force microscope (AFM) in tapping mode. Solid-state NMR data were collected with a Bruker Avance III 400 spectrometer operating at 10 Mhz.

Results and Discussion

Reaction of Lanthanum Hexaboride with Li/NH_3:

We treated bulk LaB_6 powder with a Li/NH_3 reaction and isolated and characterized the lithiated LaB_6 using PXRD and solid-state NMR to obtain insight into incorporation of lithium ions (Figure 3.1). ^{6}Li NMR experiment showed a peak at -0.5 ppm indicating the presence of a new lithium site in the lithiated LaB_6. This informs us that the lithiation reaction was successful in incorporating Li^+ ions within the LaB_6 lattice. We also performed ^{11}B and ^{139}La NMR to look at the binding environments of the constituent elements in the bulk and lithiated LaB_6. ^{139}La NMR showed peak shifting from 108 ppm to 114 ppm upon lithiation indicating that there is a change in the lanthanum environment upon lithiation. Similarly, ^{11}B NMR also displayed a change in chemical shift from 1.35 ppm to 0.22 ppm which confirmed a change in boron environment as well. The chemical shift values have been presented in Table 3.1. We have also included ^{6,7}Li and ^{11}B NMR values of standards at the end of this chapter (Table 3.2, Table 3.3)

Table 3.1. ^{11}B, ^{6}Li, ^{139}La NMR chemical shift values of bulk, lithiated and exfoliated LaB_6

	^{11}B	**^{139}La**	**^{6}Li**
LaB_6 bulk	1.35	-108.20	-
LaB_6 lithiated	0.22	-114.65	-0.05
LaB_6 exfoliated	1.45	-112.10	-

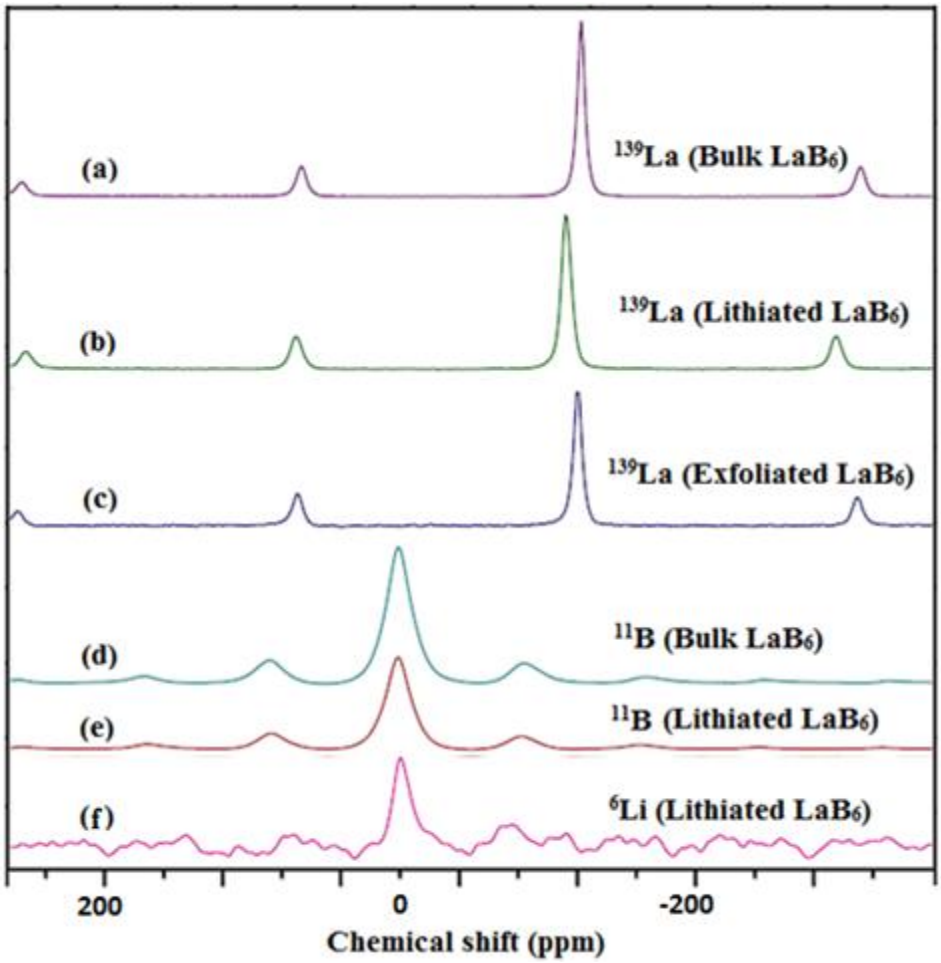

Figure 3.1. ^{139}La, ^{11}B, ^{6}Li NMR solid-state NMR on bulk, lithiated and exfoliated LaB_6

PXRD studies showed peak broadening in lithiated LaB_6 when compared to bulk LaB_6 (Figure 3.2). We also see peaks from lithium amide, a common side product of the Li/NH_3 reaction. We performed a Li concentration study and observed that the peak broadening actually gets better resolved into two peaks when higher concentrations of lithium are used in the Li/NH_3 reaction. These new set of peaks can be attributed to an additional phase that has been identified as dilithium hexaboride species LiB_3, which has a crystal structure similar to LaB_6.[20] Due to the mobility of Li^+ ions, the lithiation reaction incorporates Li^+ into the gaps between the boron octahedra in the

LaB_6 crystal lattice, to form a stable LiB_3-LaB_6 solid solution. To investigate the formation of the dilithium hexaboride intermediate, we performed three Li/NH_3 reactions with different lithium concentrations. Employing powder XRD on the lithated intermediates of these reactions (Figure 3.3) show that the reaction with higher concentration of lithium has a better resolution of the peaks of both phases; the new phase can be matched to LiB_3 (ICDD no. 04-007-2594).

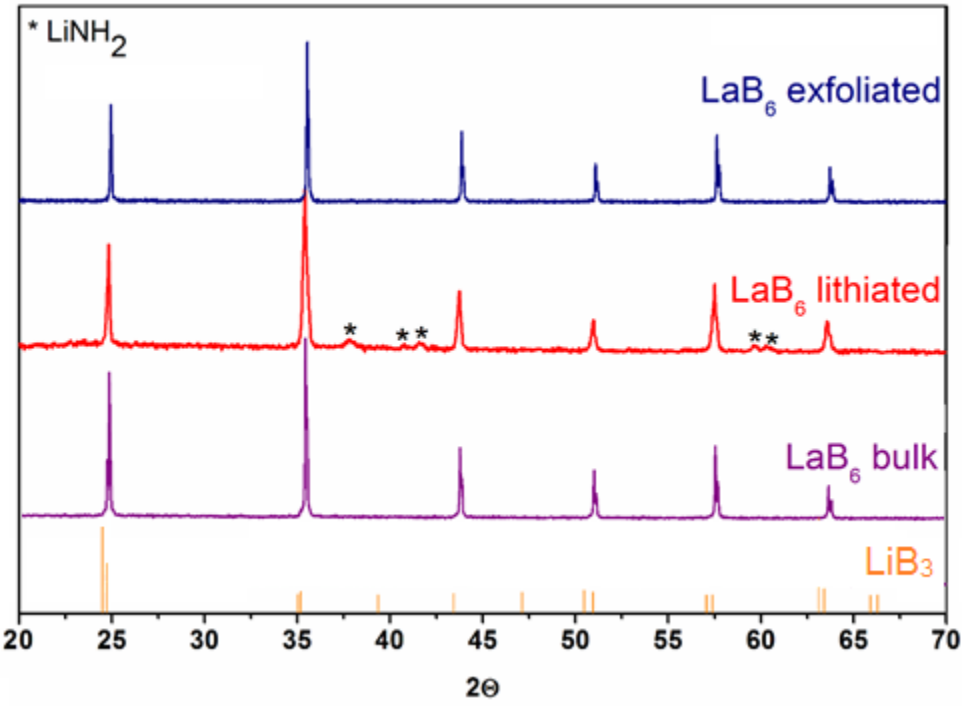

Figure 3.2. Powder x-ray diffraction patterns of bulk, lithiated and exfoliated LaB_6 with reference pattern for LiB_3 (ICDD 04-007-2594)

Table 3.2. FWHM values for bulk and lithiated LaB_6

Miller Indices	LaB_6 lithiated FWHM (2Θ)	LaB_6 bulk FWHM (2Θ)
(0 1 1)	0.0866	0.0787
(1 1 1)	0.0649	0.0480
(0 0 2)	0.0649	0.0480
(0 1 2)	0.1056	0.0480

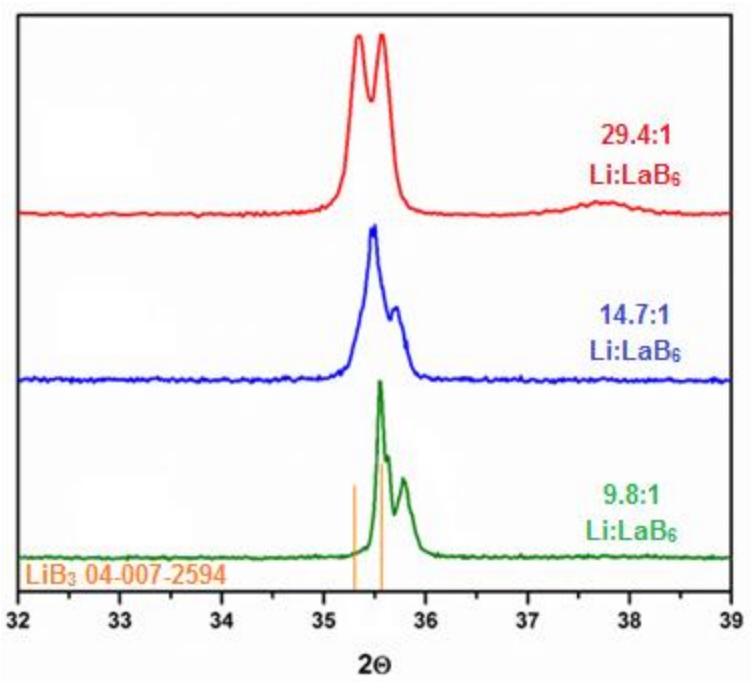

Figure 3.3. Powder x-ray diffraction patterns of lithiated LaB_6 for different concentrations of lithium reactant used with reference pattern for LiB_3 (ICDD 04-007-2594)

Comparing the morphology of the lithiated LaB_6 and bulk LaB_6 powders using SEM imaging, we see that the particle size is decreased in the lithiated LaB_6 and some large platelets are beginning to form (Figure 3.4 A-B). EDS mapping on an individual platelet shows the presence of La, B and O due to surface oxidation (Figure 3.4 D-F). Such an oxidation of nanostructured LaB_6 has been previously observed in the case of LaB_6 nanoparticles.[21]

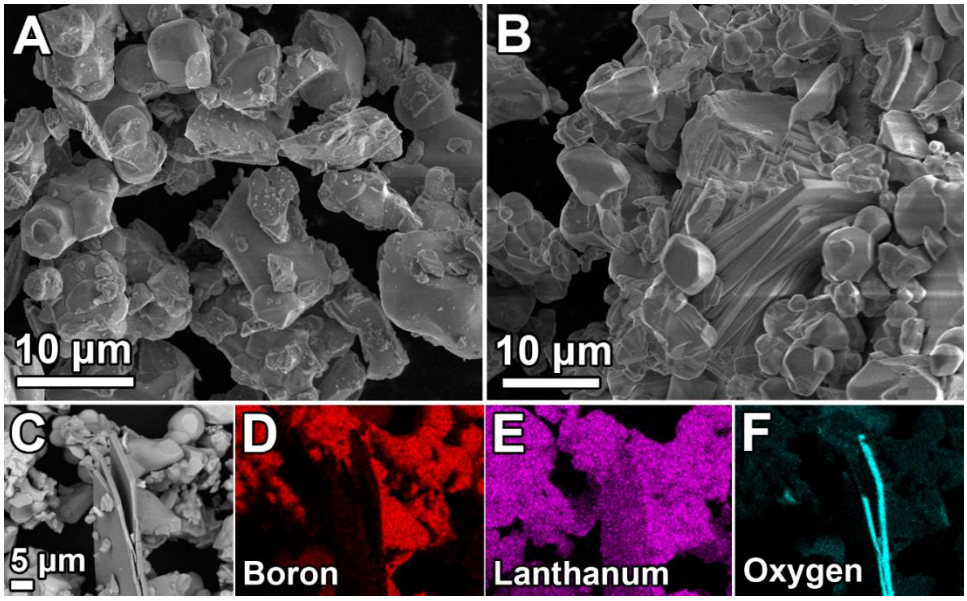

Figure 3.4. A) SEM image of bulk LaB_6 B) SEM image of lithiated LaB_6 showing the presence of platelets C) Backscatter SEM image of a platelet in lithiated LaB_6 D-F) Elemental mapping of boron, lanthanum and oxygen respectively

Once we obtained the lithiated LaB_6, the next step was to react it with deionized water to remove the lithium ions as lithium hydroxide through a highly vigorous and exothermic reaction. This "exfoliation" reaction causes a disassembly of the MB_6 structure, and is enhanced with a subsequent ultrasonication step.

$$LaB_6 + Li + NH_3 \rightarrow Li_xLaB_6 + LiNH_2$$

$$Li_xLaB_6 + H_2O \rightarrow LaB_6 + xLiOH + 1/2H_2$$

Observing the exfoliated product using TEM disclosed that LaB_6 forms a mixture of square-shaped and fragmented LaB_6 nanosheets (Figure 3.5 A), selected area electron diffraction (SAED) confirmed the cubic crystalline nature of nanosheets and the d-spacings from the pattern

were indexed to LaB_6 (3.5 B). High-resolution TEM further displayed the crystalline nature of the nanosheets and the lattice fringes were measured to be 0.30 nm which can be indexed to the (011) plane. AFM was used to determine the thickness of the LaB_6 nanosheets to be between 1-4 nm (Figure 3.5 C-D). STEM elemental mapping on the nanosheets (Figure 3.6) confirmed the presence of La and B, as well as O which is likely due to surface oxidation.

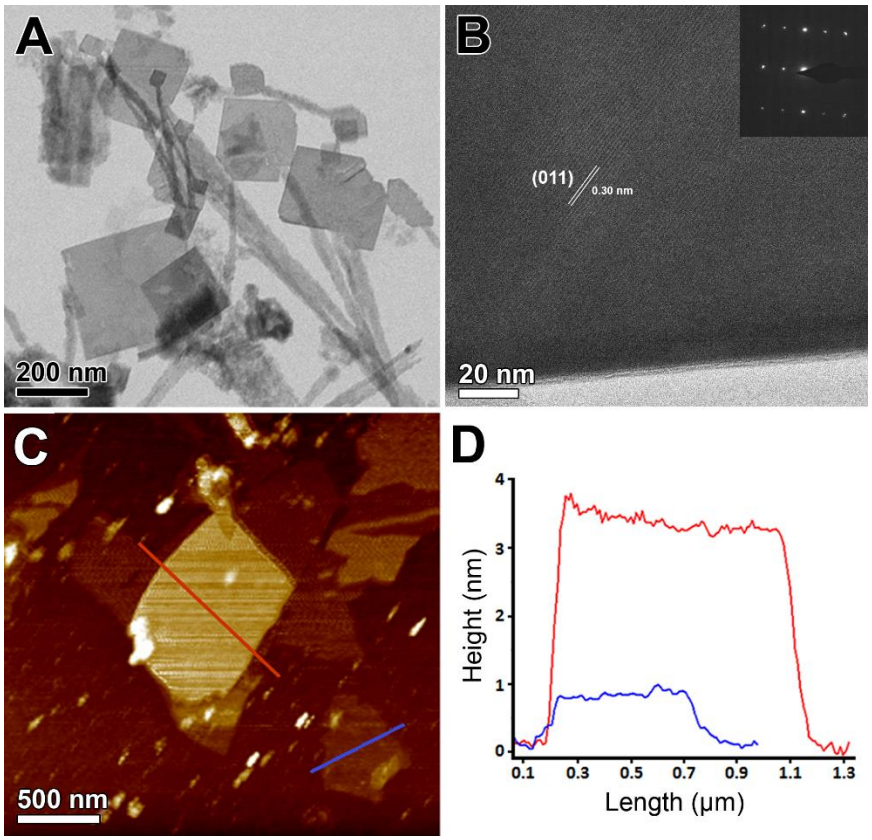

Figure 3.5. A) TEM image of LaB_6 nanoproduct B) HR-TEM image of a single LaB_6 nanosheet highlighting lattice fringes. Inset shows the cubic SAED pattern C) Topographic AFM image of LaB_6 nanosheets D) Height profile of square nanosheets and fragmented particles

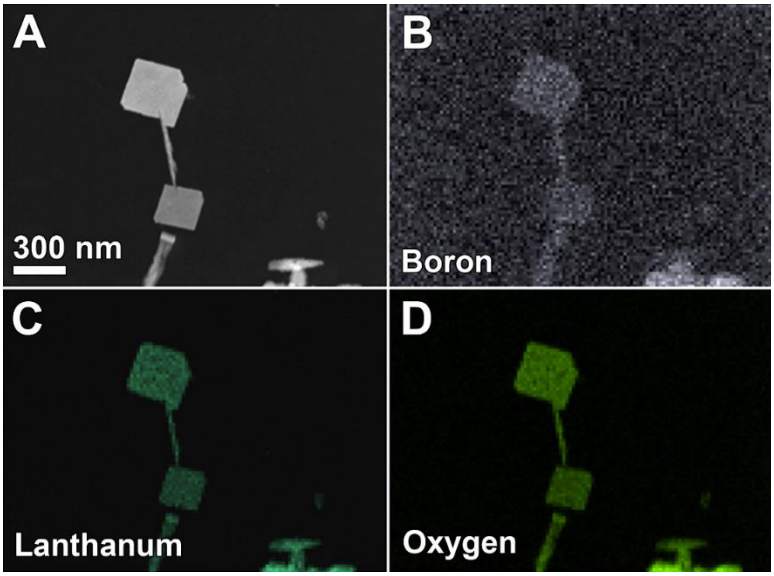

Figure 3.6. A) BF-STEM image of LaB_6 nanosheet with elemental mapping of B) Boron-K C) Lanthanum-L D) Oxygen-K

Employing solid-state ^{11}B and ^{139}La NMR spectroscopy on the exfoliated nanosheets showed that the boron environment in exfoliated LaB_6 remain unchanged with respect to bulk LaB_6 (Figure 3.1), indicating that the reaction with water removes all the lithium ions that were previously incorporated in the structure. Further analysis on our exfoliated LaB_6 nanosheets using PXRD shows a pattern that is very similar to that of bulk LaB_6, the absence of any peak broadening further confirms that there is no dilithium hexaboride present (Figure 3.2).

To confirm that the lithium incorporation into LaB_6 was indeed responsible for the exfoliation, we performed a control reaction in NH_3 which yielded no nanoproduct. Time study experiments showed that lower reaction times leads to partial exfoliation in LaB_6 (Figure 3.7 A) whereas longer reaction times leads to the formation of smaller, fragmented nanosheets (Figure 3.7 B).

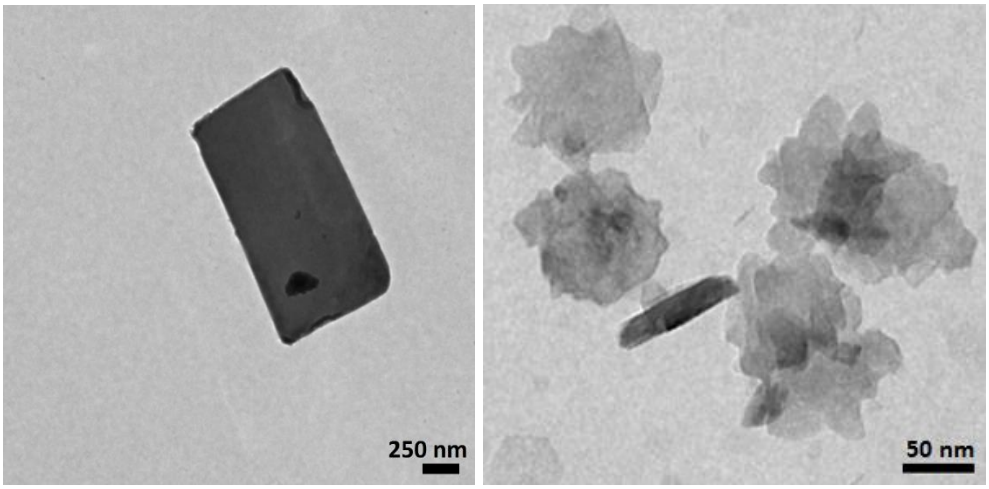

Figure 3.7. TEM of products obtained from a) 1 day Li/NH_3 reaction on LaB_6 powder b) 5 days Li/NH_3 reaction on LaB_6 powder

To check the dependence of the exfoliated product on the morphology of the starting material, we conducted identical Li/NH_3 reactions on LaB_6 nanopowder and ground up LaB_6 single crystals. The exfoliated product from the LaB_6 nanopowder consisted of small, irregular nanosheets (Figure 3.8 A) whereas the product from the reaction on LaB_6 single crystals gave us irregular, yet relatively large nanosheets and platelets of varying dimensions owing to the non-homogenous grain size of the starting material due to manual grinding (Figure 3.8 B).

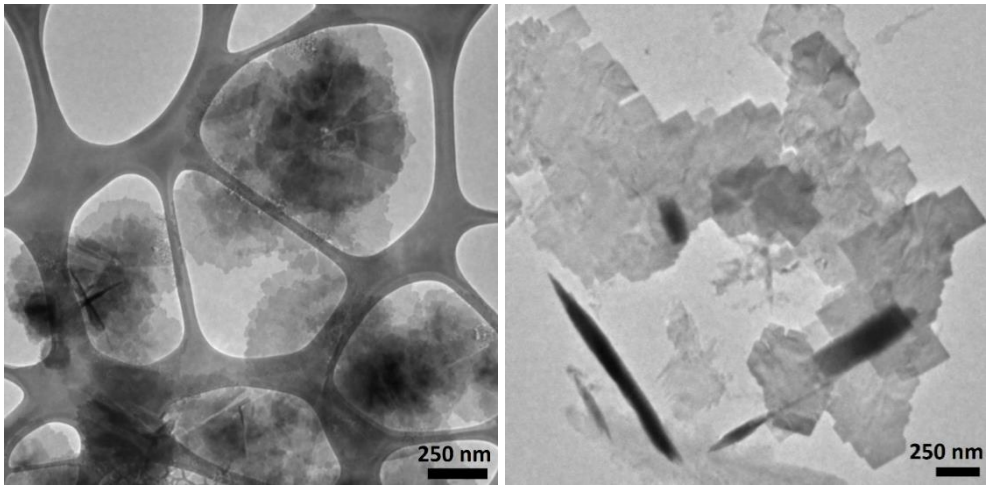

Figure 3.8. TEM of products obtained from a) LaB_6 nanopowder b) LaB_6 single crystals

Reaction on Lanthanum Hexaboride with *n*-butyllithium at high temperature:

We treated bulk LaB_6 powder with a 11 days long *n*-BuLi reaction at 65 ºC. Observing the lithiated and bulk LaB_6 powders under SEM showed a visible change in morphology between the bulk and lithiated (Figure 3.9). When comparing bulk LaB_6 (Figure 3.9 A) to lithiated LaB_6 (Figure 3.9 B), we see that the surface of the bulk is smooth whereas the lithiated is composed of small, regular shaped platelets and some irregular particles. On closer inspection, we observe that the platelets are less than a micron in size and square-shaped with clearly defined edges, unlike the morphology of the bulk LaB_6 starting material which is smooth and has particle dimensions of about 5 microns. This morphology change upon lithiation is interesting as it gives us some insight on the nanostructuring that occurs upon lithiation. EDS mapping on the platelets of lithiated LaB_6 showed the presence of boron, lanthanum and surface oxygen (Figure 3.9 D-F).

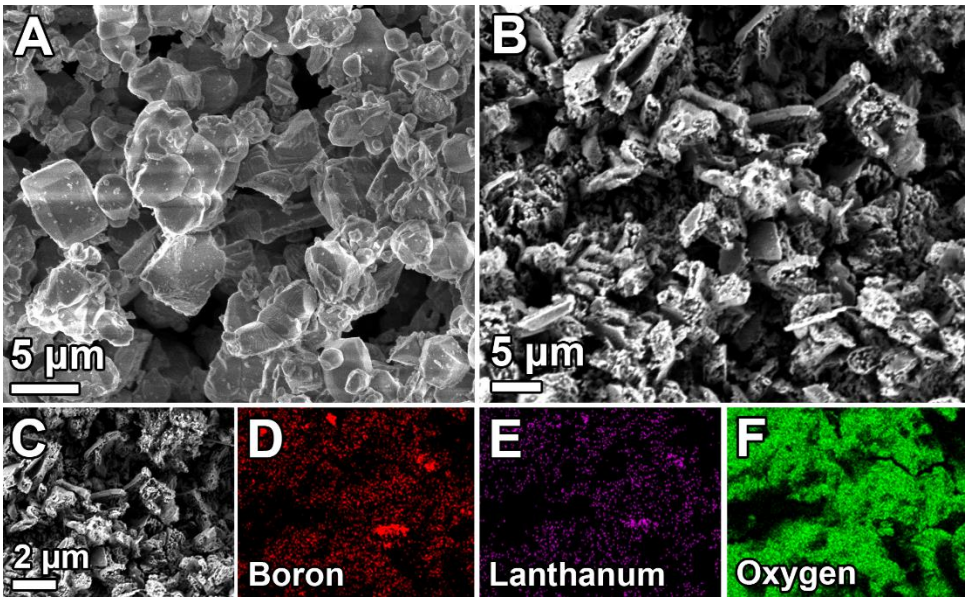

Figure 3.9. A) SEM image of bulk LaB_6 B) SEM image of *n*-BuLi lithiated LaB_6 showing the presence of platelets and particles C) Backscatter high magnification SEM image of lithiated LaB_6 D-F) Elemental mapping of boron, lanthanum and oxygen respectively

We additionally characterized the lithiated LaB_6 powder using PXRD to check for changes in the composition upon lithiation. Immediate characterization by PXRD showed the presence of two phases in the lithiated LaB_6, which can be indexed to LiB_3 and LaB_6 (Figure 3.10). This indicates that a LiB_3 phase is formed as an intermediate when lithium ions are being inserted into the LaB_6 lattice, which is similar to what we observed previously in the case of lithiated SrB_6. We hypothesize that LiB_3 and LaB_6 exist as solid solutions with nanodomains of LiB_3 being formed. This phenomenon has been observed in the case of other hexaboride solid-solutions.[22] However, as LiB_3 is sensitive to water,[21] it gets quickly oxidized to LiOH under ambient conditions which we observe in the XRD pattern (Figure 3.10).

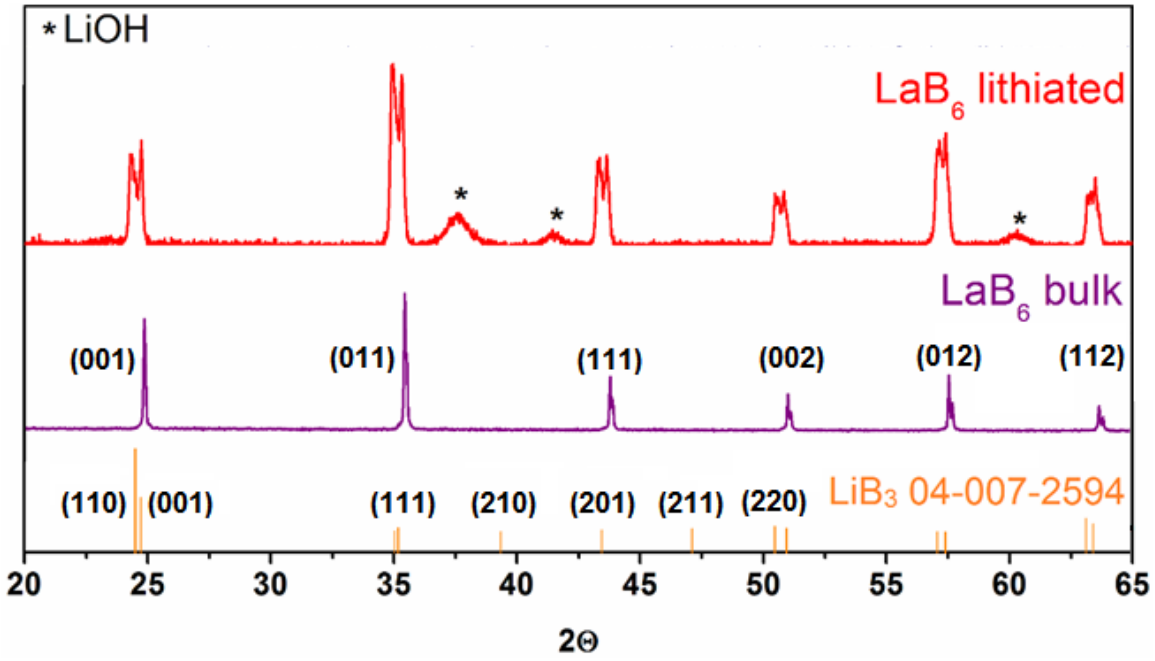

Figure 3.10. Powder x-ray diffraction patterns of bulk, *n*-BuLi lithiated and exfoliated LaB_6 with reference pattern for LiB_3 (ICDD 04-007-2594)

Observing the exfoliated product under TEM showed much smaller nanosheets with square-shaped edges (Figure 3.11). This reflects the morphology of the lithiated LaB_6 from this reaction, the dimensions of the platelets formed in lithiated LaB_6 were much smaller and thinner when compared to the Li/NH_3 reaction (Figure 3.9 B). There were also some fragmented sheets and smaller particles present. We see that the PXRD pattern of exfoliated LaB_6 from this reaction (Figure 3.10 B) shows only the LaB_6 phase, unlike the lithiated with shows presence of LaB_6 and LiB_3. This indicates that all the Li^+ ions are removed upon treatment with water.

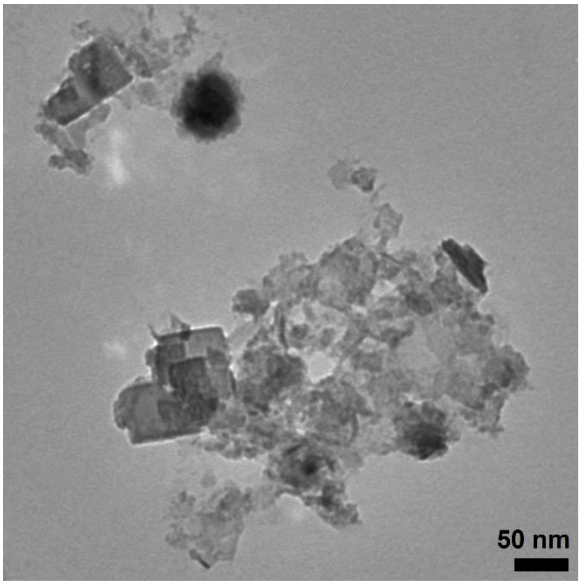

Figure 3.11. TEM image of nanoproduct obtained from *n*-BuLi reaction on LaB_6 at 65 ^oC

Table 3.2. Literature values for ^{7}Li NMR chemical shifts of relevant lithium-containing compounds

Lithium compound	^{7}Li (ppm)	NMR technique	Reference
Li_2O	2.8	solid state	Meyer, B. M., Leifer, N., Sakamoto, S., Greenbaum, S. G., & Grey, C. P. "High field multinuclear NMR investigation of the SEI layer in lithium rechargeable batteries" *Electrochemical and solid-state letters* 8.3 (2005): A145-A148.
$LiOH{\bullet}H_2O$	0.4	solid state	
Li (metal)	258	solid state	Bhattacharyya, R., Key, B., Chen, H., Best, A. S., Hollenkamp, A. F., & Grey, C. P. "In situ NMR observation of the formation of metallic lithium microstructures in lithium batteries" *Nature materials* 9.6 (2010): 504-510.
LiH	1.5	solid state	Wang, Y., Guo, Z. X. "Enhanced hydrogen desorption of an ammonia borane and lithium hydride system through synthesised intermediate compounds" *Journal of Materials Chemistry A* (2014) 2 :6801-6813
$LiBH_4$	-2.7	solid state	Verkuijlen, M.H., Ngene, P., de Kort, D.W., Barré, C., Nale, A., van Eck, E.R., van Bentum, P.J.M., de Jongh, P.E. and Kentgens, A.P. "Nanoconfined $LiBH_4$ and enhanced mobility of Li^+ and BH_4^- studied by solid-state NMR" *The Journal of Physical Chemistry C* 116.42 (2012): 22169-22178.

Table 3.3. Literature values for ^{139}La NMR chemical shifts of relevant lanthanum-containing compounds

Lanthanum compound	^{139}La (ppm)	NMR technique	Reference
LaB_6	-128 $\pm$ 10	solid state	Lutz, O. and Oehler, H., 1980. 135La and139La nuclear magnetic resonance studies. *Journal of Magnetic Resonance* (1969), 37(2), pp.261-267.
La_2O_3	640 $\pm$ 10	solid state	Spencer, L., Coomes, E., Ye, E., Terskikh, V., Ramzy, A., Thangadurai, V. and Goward, G.R., 2011. Structural analysis of lanthanum-containing battery materials using 139La solid-state NMR. *Canadian Journal of Chemistry*, 89(9), pp.1105-1117.
$La(OH)_3$	260 $\pm$ 20	solid state	

Table 3.4. Literature values for ^{11}B NMR chemical shifts of relevant boron-containing compounds

Boron compound	^{11}B (ppm)	NMR technique	Reference
Li_2B_4O7	2.3 ± 0.1 18.2 ± 0.2	solid state	Hansen, M. R., Vosegaard, T., Jakobsen, H. J., & Skibsted, J. "^{11}B chemical shift anisotropies in borates from ^{11}B MAS, MQMAS, and single-crystal NMR spectroscopy" *The Journal of Physical Chemistry A* 108.4 (2004): 586-594.
B_2O_3	13.0 ± 1 18.1 ± 1.2	solid state	Youngman, R. E., and Zwanziger, J. W. "Multiple boron sites in borate glass detected with dynamic angle spinning nuclear magnetic resonance" *Journal of non-crystalline solids* 168.3 (1994): 293-297.
H_3BO_3 or $B(OH)_3$	19.1	solid state	Irwin, A. D., Holmgren, J. S., & Jonas, J. "Solid state ^{29}Si and ^{11}B NMR studies of sol-gel derived borosilicates" *Journal of non-crystalline solids*, 101.2(1988): 249-254.
HBO_2	2.0 13.0	solid state	Jimenez, M., Duquesne, S. and Bourbigot,S. "Intumescent fire protective coating: toward a better understanding of their mechanism of action" *Thermochimica acta* 449.1 (2006): 16-26.
α-rhombohedral B	48.0 −83.2	solid state	Lee, Donghoon, Philip J. Bray, and Terry L. Aselage. "The NQR and NMR studies of icosahedral borides" *Journal of Physics: Condensed Matter* 11.22 (1999): 4435.
β-rhombohedral B	14.2	solid state	Turner, C. L., Taylor, R. E. and Kaner, R. B. "^{10}B and ^{11}B NMR Study of Elemental Boron" *The Journal of Physical Chemistry C* 119.24 (2015): 13807-13813.
$LiBH_4$	-42.9	solid state	Verkuijlen, M.H., Ngene, P., de Kort, D.W., Barré, C., Nale, A., van Eck, E.R., van Bentum, P.J.M., de Jongh, P.E. and Kentgens, A.P. "Nanoconfined $LiBH_4$ and enhanced mobility of Li^+ and BH_4^-studied by solid-state NMR" *The Journal of Physical Chemistry C* 116.42 (2012): 22169-22178.
CaB_6	331 ± 9	solid state	Sears, R. E. J. "^{11}B chemical shifts and quadrupole coupling constants in the alkaline–earth hexaborides" *The Journal of Chemical Physics* 76.11 (1982): 5651-5652.
SrB_6	186 ± 14	solid state	
BaB_6	147 ± 10	solid state	
LaB_6	2	solid state	Ammar, A., Ménétrier, M., Villesuzanne, A., Matar, S., Chevalier, B., Etourneau, J., Villeneuve, G., Rodríguez-Carvajal, J., Koo, H.J., Smirnov, A.I. and Whangbo, M.H. "Investigation of the electronic and structural properties of potassium hexaboride, KB_6, by transport, magnetic susceptibility, EPR, and NMR measurements, temperature-dependent crystal structure determination, and electronic band structure calculations" *Inorganic chemistry* 43.16 (2004): 4974-4987.
KB_6	84	solid state	

Conclusions

We have exfoliated lanthanum hexaboride into nanosheets using a novel lithium ion incorporation-exfoliation method. We utilized two lithiating solutions, Li/NH_3 and *n*-BuLi/hexane, to incorporate lithium ions into the bulk lanthanum hexaboride structure. After lithation, the lithiated intermediate (Li_xLaB_6) was structurally characterized using PXRD, multinuclear solid-state NMR and SEM/EDS. We detected the formation of a Li_2B_6 intermediate from PXRD and observed that lithiation is accompanied by a significant change in the ^{11}B and ^{139}La chemical environments. Additionally, a morphological change was also observed in LaB_6 upon lithiation.

The lithiated lanthanum hexaboride Li_xLaB_6 powders were exfoliated to produce uniform, square-shaped nanosheets which were characterized using PXRD, multinuclear solid-state NMR, TEM and AFM. The morphology of the nanoproduct was affected by multiple factors; using a lanthanum hexaboride bulk precursor with a larger grain size led to exfoliated nanoproducts of larger size, while increasing the duration of the lithiation reaction led to the formation of smaller, fragmented exfoliated nanoproducts.

The formation of LaB_6 nanosheets is of great significance as this is the first report of metal boride nanosheets. Efforts have been made to synthesize boron-based nanosheets from layered metal borides,[23-27] however, the products obtained are fragmented or crumpled, with a large degree of oxidation or surface modifications. Our synthetic method creates LaB_6 nanosheets with well-defined edges that have lateral dimensions on the micron scale, and thickness below 4 nm. This makes them an ideal candidate for use in coating materials, as they can be solution processed easily instead of fabricating thin films from the bulk boride.

References

1. Mroz, C. *Am. Ceram. Soc. Bull.*, **1995**. *74*. 165–166
2. Lundström, T. *Pure Appl. Chem*. **1985**. 57. *10*. 1383-90.
3. Lafferty, J.M. *J. Appl. Phys*. **1951**. 22. *3*. 299-309.
4. Fahrenholtz, W. G., Hilmas, G. E., Talmy, I. G., Zaykoski, J. A. *J. Am. Ceram. Soc.* **2007.** 90. *5*. 1347-1364.
5. Mitterer, C. *J. Solid State Chem.* **1997**. 133. *1*. 279-291.
6. Osada, M. and Sasaki, T. *Adv. Mater*. **2012**. 24. *2*. 210-228.
7. Zhang, H., Zhang, Q., Tang, J. Qin, L.C. *J.A.C.S.* **2005.** 127. *9*. 2862-2863.
8. Brewer, J.R., Deo, N., Wang, Y. M., Cheung, C.L. *Chem. Mater*. **2007**. 19. *26*. 6379-6381.
9. Selvan, R.K., Genish, I., Perelshtein, I., Calderon Moreno, J.M. and Gedanken, A. *J. Phys. Chem. C*. **2008**. 112. *6*.1795-1802.
10. Takeda, H., Kuno, H. and Adachi, K., *J.A.C.S*. **2008**. 91. *9*. 2897-2902.
11. Adachi, K., Miratsu, M., Asahi, T. *J. Mater. Res.* **2010**. 25. *3*. 510-521.
12. Zhou, S., Zhang, J., Liu, D., Lin, Z., Huang, Q., Bao, L., Ma, R. and Wei, Y. *Acta Mater*. **2010**. 58. *15*. 4978-4985.
13. Zhang, H., Tang, J., Yuan, J., Ma, J., Shinya, N., Nakajima, K., Murakami, H., Ohkubo, T., Qin, L.C. *Nano Lett.* **2010**. 10. *9*. 3539-3544.
14. Brewer, J.R., Jacobberger, R.M., Diercks, D.R., Cheung, C.L. *Chem. Mater.* **2011**. 23. *10*. 2606-2610.
15. Yuan, Y., Zhang, L., Liang, L., He, K., Liu, R., Min, G. *Ceram. Int*. **2011.** 37. *7*. 2891-2896.
16. Jha, M., Patra, R., Ghosh, S. Ganguli, A.K. *Solid State Commun.* **2013**. 153. *1*. 35-39.

17. Mattox, T.M., Agrawal, A. and Milliron, D.J., 2015. *Chem Mater.* **2015**. 27. *19*. 6620-6624.

18. Xu, J., Hou, G., Li, H., Zhai, T., Dong, B., Yan, H., Wang, Y., Yu, B., Bando, Y. Golberg, D. *NPG Asia Mat.* **2013** 5. *7*. e53.

19. Sato, Y., Terauchi, M., Mukai, M., Kaneyama, T., Adachi, K. *Ultramicroscopy* **2011**. 111. *8.* 1381-1387.

20. Mair, G., H. G. von Schnering, M. Wörle. *Z. Anorg. Allg. Chem.* **1999**. *625*. 1207–1211.

21. Machida, K., Okada, M., Yoshio, S., Adachi, K. *J. Mater. Res.* **2016**. 1-9.

22. Cahill, J.T., Alberga, M., Bahena, J., Pisano, C., Borja-Urby, R., Vasquez, V.R., Edwards, D., Misture, S.T. and Graeve, O.A. *Cryst. Growth Des.* **2017.**

23. Sexton, D.R., 2014. *Synthesis, delamination, and characterization of substituted magnesium diboride* (Doctoral dissertation, uga).

24. Das, S.K., Bedar, A., Kannan, A. and Jasuja, K. *Scientific reports*. **2015**. 5.

25. Ratnam, D., Das, S.K. Jasuja, K. ICAMT – Elsevier Materials Today: Proceedings. **2016**.

26. James, A.L. Jasuja, K. *RSC Advances*. **2017**. 7. *4*. 1905-1914.

27. Nishino, H., Fujita, T., Yamamoto, A., Fujimori, T., Fujino, A., Ito, S.I., Nakamura, J., Hosono, H., Kondo, T. *J. Phys. Chem. C*. **2017**.

CHAPTER 4

LITHATION AND NANOSTRUCTURING OF CALCIUM HEXABORIDE, CERIUM HEXABORIDE AND SAMARIUM HEXABORIDE

Roshini Ramachandran and Tina T. Salguero. To be submitted to *Journal of Materials Research*.

Abstract

We used two lithium ion incorporation techniques to lithiate bulk CaB_6, CeB_6 and SmB_6 powders. After lithation, the lithiated intermediate was structurally characterized using powder x-ray diffraction (PXRD) and scanning electron microscopy (SEM). The lithiated intermediate was then exfoliated by subsequently treating with deionized water to remove the lithium ions incorporated and produce a disassembly of the structure. The effect of reaction temperature, reaction duration, concentration of lithiating reagent, and nature of metal hexaboride precursor were also investigated. The products formed through these lithiation-exfoliation reactions were nanostructured to various degrees. Powder x-ray diffraction and transmission electron microscopy (TEM) were used to characterize the morphology and composition of the exfoliated products obtained through the various reaction conditions. Out of the three bulk starting materials, CaB_6 proved to be the most versatile for exfoliation and sensitive to changes in reaction conditions. We were able to exfoliate CaB_6 into small nanosheets and platelets, CeB_6 was nanostructured to a moderate degree and formed regular square-shaped platelets while SmB_6 only underwent a partial exfoliation to produce fragments.

Introduction

Metal hexaborides have extensive use as high-temperature materials, especially for surface protection and wear resistance. There are several metal hexaborides that possess other unique and useful properties. For example, Cerium hexaboride is a refractory ceramic with a high melting point of 2522 °C. It has a low work function and higher electron emissivity than lanthanum hexaboride, due to which it has widespread application as a cathode material for use in electron microscopes, microwave tubes, electron lithography, X-Ray tubes, and free electron lasers.[1,2]

Calcium hexaboride has a melting point of 2235 °C and is also used as a cathode material due to its low work function.[1] Additionally, CaB_6 is a favorable candidate for n-type thermoelectric materials, with a power factor comparable to those of conventional thermoelectrics such as bismuth telluride and silicon germanide.[3,4]

Samarium hexaboride is an intermediate-valence compound consisting of both Sm^{2+} and Sm^{3+} in a 3:7 ratio within the metal hexaboride crystal lattice.[5] It has a melting point of 2400 ºC and is a known Kondo insulator.[6] It has recently been discovered to be a topological insulator[7], however, much debate exists on the origin of topological insulation in SmB_6.

To date, efforts at nanostructuring these materials mainly involve bottom-up approaches involving solid or soluble boron and metal precursors. In the case of CeB_6, due to its desirable application in cathdoes, many morphologies ranging from nanowires, nanorods, nanoparticles, to nanocomposites with other materials have been synthesized.[8,9,10,11]

For CaB_6 and SmB_6, nanostructuring of the bulk materials has not been explored as much and the synthesized morphologies include nanowires and nanocrystalline powders and thin films.[12,13,14,15]

We were interested in exfoliating the above mentioned hexaborides into nanosheets to improve their processability. Nanosheets of these metal hexaboride would only require simple solution-based methods such as spray coating, dip coating and inkjet printing to form coatings for high performance applications. This is a big step forward from current methods employed for their processing such as physical and chemical vapor deposition that involve expensive and laborious equipment and precursors.

Another aspect to explore is the possible change in properties of nanomaterials when compared to their bulk counterparts. Owing to their small size and spatial factors such as anisotropy and dimensionality, we may observe an enhancement in mechanical and physical properties of these metal hexaboride nanosheets.[16] Especially in the case of samarium hexaboride, it would be very interesting to note the difference in properties between the bulk and nanosheet morphology to provide insight on, and fully understand the mechanism of topological insulation.

Experimental

Materials: Cerium hexaboride (3N, ESPI Metals), Calcium hexaboride (99.5%, Sigma Aldrich), Samarium hexaboride (99.9%, Ryan Scientific Inc.), 11 M *n*-butyllithium in hexanes (Sigma Aldrich), 2.5 M *n*-butyllithium in hexanes (Sigma Aldrich), lithium ribbon (99.9%, Sigma Aldrich), hexanes (≥98.5%, Fisher), anhydrous ammonia (99.99%, Airgas)

Lithiation reactions:

Reaction of calcium hexaboride with Li/NH3

0.3 g (0.0028 moles) of CaB_6 powder and 0.1 g Li (0.0144 moles) were placed in a modified Schlenk vessel with Teflon cap. The Schlenk vessel was kept in an ethanol bath equipped with temperature probe maintained at -50 ^{o}C. The reaction vessel was pumped down to 5 mbar using a diffusion pump. Once the ethanol bath reached -50 ^{o}C, the pump was switched off and 40 mL of ammonia gas was slowly condensed into the vessel. The CaB_6 powder is left sitting in the Li/NH_3 solution for 3 or 7 days, after which the NH_3 gas is evaporated off into dil HCl solution. The product is washed with NH_3 two or three times to remove any remaining elemental lithium. The reaction vessel is then flushed with Argon gas, pumped down to remove any remaining gas and taken into an Argon glove box. The lithiated CaB_6 ($Li_xCa_{2-x}B_6$) powder is removed from the Schlenk vessel and stored in the Argon glove box pending future characterization.

Reaction of cerium hexaboride with Li/NH_3

0.15 g (0.0007 moles) of CeB_6 powder and 0.1 g Li (0.0144 moles) were placed in a modified Schlenk vessel with Teflon cap. The Schlenk vessel was kept in an ethanol bath equipped with temperature probe maintained at -50 ^oC. The reaction vessel was pumped down to 5 mbar using a diffusion pump. Once the ethanol bath reached -50 ^oC, the pump was switched off and 40 mL of ammonia gas was slowly condensed into the vessel. The CeB_6 powder is left sitting in the Li/NH_3 solution for 5 days, after which the NH_3 gas is evaporated off into dil HCl solution. The product is washed with NH_3 two or three times to remove any remaining elemental lithium. The reaction vessel is then flushed with Argon gas, pumped down to remove any remaining gas and taken into an Argon glove box. The lithiated CeB_6 powder ($Li_xCe_{2-x}B_6$) is removed from the Schlenk vessel and stored in the Argon glove box pending future characterization.

Reaction of cerium hexaboride with n-butyllithium at room temperature

0.1 g (0.0007 moles) of CeB_6 powder was placed in a glass vial equipped with a Teflon stir bar. 1 mL of 2.5 M *n*-butyllithium and 4 mL of anhydrous hexane was added to the vial in an Argon glove box. The reaction was left stirring at 300 rpm at room temperature for a period of 11 days. After 11 days, the reaction mixture was filtered in the Argon glove box using a vacuum filtration setup and the filtered powder was washed twice with hexane to remove any remaining *n*-butyllithium. The lithiated CeB_6 powder ($Li_xCe_{2-x}B_6$) was dried overnight in the Argon glove box and stored under inert conditions.

Reaction of calcium hexaboride with n-butyllithium at room temperature

0.1 g (0.001 moles) of CaB_6 powder was placed in a glass vial equipped with a Teflon stir bar. 1 mL of 2.5 M *n*-butyllithium and 4 mL of anhydrous hexane was added to the vial in an Argon glove box. The reaction was left stirring at 300 rpm at room temperature for a period of 11 days. After 11 days, the reaction mixture was filtered in the Argon glove box using a vacuum filtration setup and the filtered powder was washed twice with hexane to remove any remaining *n*-butyllithium. The lithiated CaB_6 powder ($Li_xCa_{2-x}B_6$) was dried overnight in the Argon glove box and stored under inert conditions.

Reaction of calcium hexaboride with n-butyllithium for 3 months

0.1 g of CaB_6 powder (0.001 moles) was placed in a glass vial equipped with a Teflon stir bar. 1 mL of 2.5 M *n*-butyllithium and 4 mL of anhydrous hexane was added to the vial in an Argon glove box. The reaction was left stirring at 300 rpm at room temperature for a period of 3 months. After 3 months, the reaction mixture was filtered in the Argon glove box using a vacuum filtration setup and the filtered powder was washed twice with hexane to remove any remaining *n*-butyllithium. The lithiated CaB_6 powder ($Li_xCa_{2-x}B_6$) was dried overnight in the Argon glove box and stored under inert conditions.

Reaction of calcium hexaboride with n-butyllithium at high temperature

0.1 g of CaB_6 powder (0.001 moles) was placed in a glass vial equipped with a Teflon stir bar. 2 mL of 11 M *n*-butyllithium and 1 mL of anhydrous hexane was added to the vial in an Argon glove box. The vials were sealed with parafilm and placed in a beaker filled with metallic thermal

beads for uniform heating. The reaction was then left stirring at 300 rpm on a hot plate maintained at 80 ^{o}C for a period of 11 days. After 11 days, the reaction mixture was filtered in the Argon glove box using a vacuum filtration setup and the filtered powder was washed twice with hexane to remove any remaining *n*-butyllithium. The lithiated CaB_6 powder ($Li_xCa_{2-x}B_6$) was dried overnight in the Argon glove box and stored under inert conditions.

Reaction of samarium hexaboride with n-butyllithium at high temperature

0.1 g of SmB_6 powder (0.0005 moles) was placed in a glass vial equipped with a Teflon stir bar. 2 mL of 11 M *n*-butyllithium and 1 mL of anhydrous hexane was added to the vial in an Argon glove box. The vials were sealed with parafilm and placed in a beaker filled with metallic thermal beads for uniform heating. The reaction was then left stirring at 300 rpm on a hot plate maintained at 80 ^{o}C for a period of 14 days. After 14 days, the reaction mixture was filtered in the Argon glove box using a vacuum filtration setup and the filtered powder was washed twice with hexane to remove any remaining *n*-butyllithium. The lithiated SmB_6 powder ($Li_xSm_{2-x}B_6$) was dried overnight in the Argon glove box and stored under inert conditions.

Exfoliation reactions:

The lithiated intermediate powders ($Li_xCa_{2-x}B_6$, $Li_xCe_{2-x}B_6$, $Li_xSm_{2-x}B_6$) were treated with 20 mL of deionized water kept in an ice bath. The product mixture was centrifuged and decanted to remove soluble byproduct LiOH. The solid product was washed and subjected to another cycle of centrifugation and decanting. The residual product was then re-dispersed in water and probe

sonicated at 60 amp for 1 hour. The subsequent exfoliated product was vacuum dried or stored as a dispersion in water until future analysis.

Characterization:

The composition of the bulk, lithiated and exfoliated materials was confirmed using a Bruker D8- Advance powder X-ray diffractometer (Co-Kα radiation source) operated at 40 mA and 40 kV. The PXRD patterns were recorded over the 2θ range of 5−80° with a scanning rate of 0.1 sec $step^{-1}$. The morphology of the lithiated intermediate and exfoliated products were examined using a FEI Inspect F field emission gun scanning electron microscope (FEG-SEM) equipped with a EDAX energy dispersive x-ray spectrometer (EDS) operating at 20 kVand a FEI Teneo FEG-SEM with an Oxford EDS system operated at 5-10 keV. The lithiated samples were prepared for SEM by sprinkling the powders on carbon sticky tape while the exfoliated samples were dropcast on a silicon wafer. A Misonix S-4000 Ultrasonic Liquid Processor was used for the sonication step. The morphology of the exfoliated nanoproducts were additionally characterized using a FEI Tecnai 20 (200 kV) TEM with selected area electron diffraction (SAED) capability. Solid-state NMR data were collected with a Bruker Avance III 400 spectrometer operating at 10000 Mhz. Spectral deconvolution was performed using the SpinWorks4 software.

Results and discussion

Reactions of CaB_6 and CeB_6 with Li/NH_3

Treating bulk CaB_6 powder with a 3 days long Li/NH_3 reaction and subsequent exfoliation of the lithiated CaB_6 powder led to the formation of thick, large micron-sized platelets of CaB_6 (Figure 4.1 A). When the Li/NH_3 reaction time was increased to 7 days, the exfoliated product showed smaller but irregular fragments of CeB_6 (Figure 4.1 B). The exfoliated products in both the reactions were not optimal for the nanoscale products that we desired, and alternate routes for improving the degree of lithiation was the next step for consideration.

Similarly, we treated bulk CeB_6 powder with a 5 days long Li/NH_3 reaction. Exfoliation of the lithiated CeB_6 from this reaction yielded structured, square-shaped platelets that were less than 1 micron in lateral dimensions (Figure 4.2 A). Performing selected area electron diffraction on a single platelet showed a cubic pattern that was indexed to CeB_6 (Figure 4.2 B).

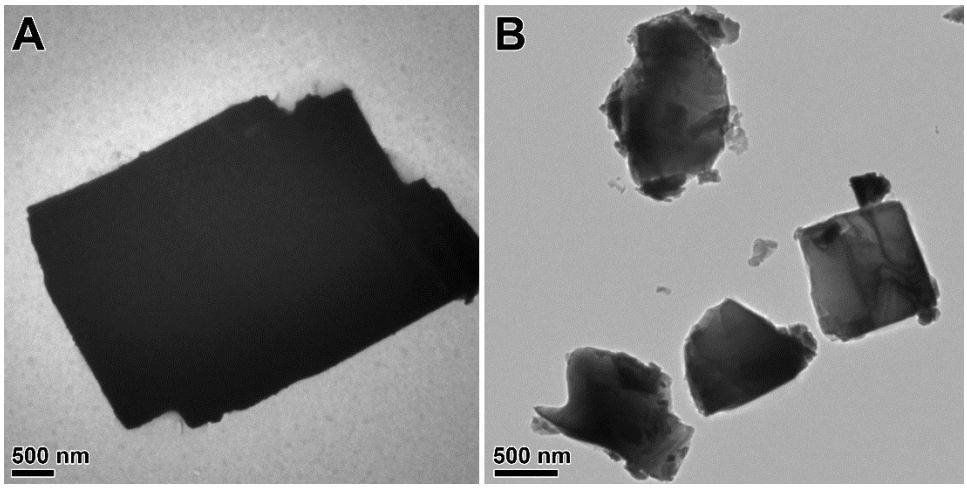

Figure 4.1. A) TEM image showing the large platelets obtained as the exfoliated product from the Li/NH_3 reaction on CaB_6. B) TEM image showing the irregular fragments produced from a 7 day long Li/NH_3 reaction on CaB_6.

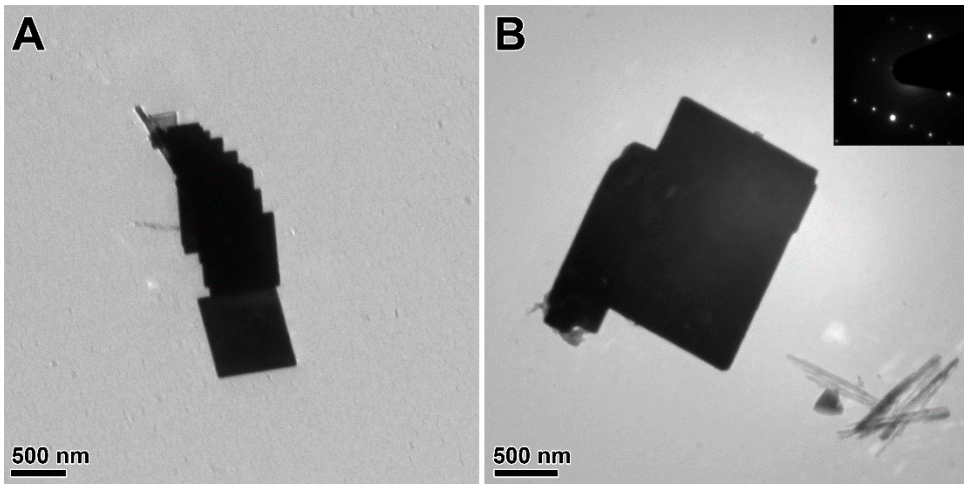

Figure 4.2. A) TEM image illustrating the regular, square-shaped platelets obtained after the exfoliation of lithiated CeB_6 from the Li/NH_3 reaction. B) TEM image highlighting a single platelet, inset SAED shows a single crystalline cubic pattern which can be indexed to CeB_6.

Reactions of CeB_6 and CaB_6 with n-butyllithium at room temperature

We treated bulk CaB_6 and CeB_6 powders with 11 day long *n*-BuLi reactions at room temperature. Observing the lithiated and bulk CaB_6 and CeB_6 powders under SEM showed a visible change in morphology between the bulk and lithiated (Figure 4.3). When comparing bulk CaB_6 (Figure 4.3 A) to lithiated CaB_6 (Figure 4.3 C), we see that the surface of the bulk is smooth whereas the lithiated is composed of small, regular shaped platelets and some irregular particles. On closer inspection, we observe that the platelets are only a few microns in size and square-shaped with clearly defined edges (Figure 4.3 D), unlike the morphology of the bulk CaB_6 starting material. When comparing bulk CeB_6 (Figure 4.3 B) with lithiated CeB_6 (Figure 4.3 E), we see a similar trend where the surface of the lithiated is rough and composed of aggregates of small, micron sized particles. In contrast, bulk CeB_6 has a smooth surface and has particle dimensions of over 25 microns. This morphology change upon lithiation is interesting as it gives us some insight

on the nanostructuring that occurs upon lithiation. It is apparent that the morphology of the lithiated material is indicative of the morphology of the exfoliated product. Upon exfoliation of the lithiated powders, CaB_6 yielded a mixture of irregular fragments and some regular nanosheets (Figure 4.4 A) whereas CeB_6 only produced large fragments (Figure 4.4 B), indicating that the aggregates of particles that we observed in the lithiated are fused together.

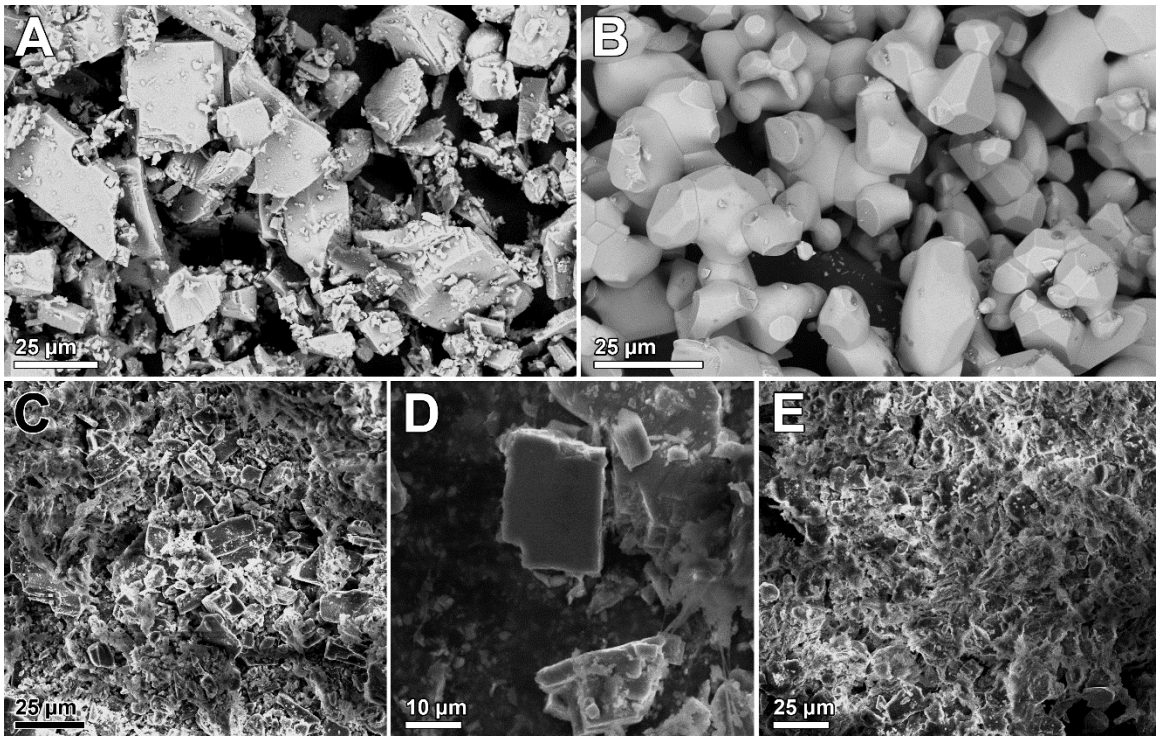

Figure 4.3. SEM images of A) Bulk CaB_6 B) Bulk CeB_6 C) Lithiated CaB_6 showing formation of platelets on the surface D) Zoom in of a single platelet on lithiated CaB_6 E) Lithiated CeB_6 displaying a rough surface with aggregated irregular particles and platelets

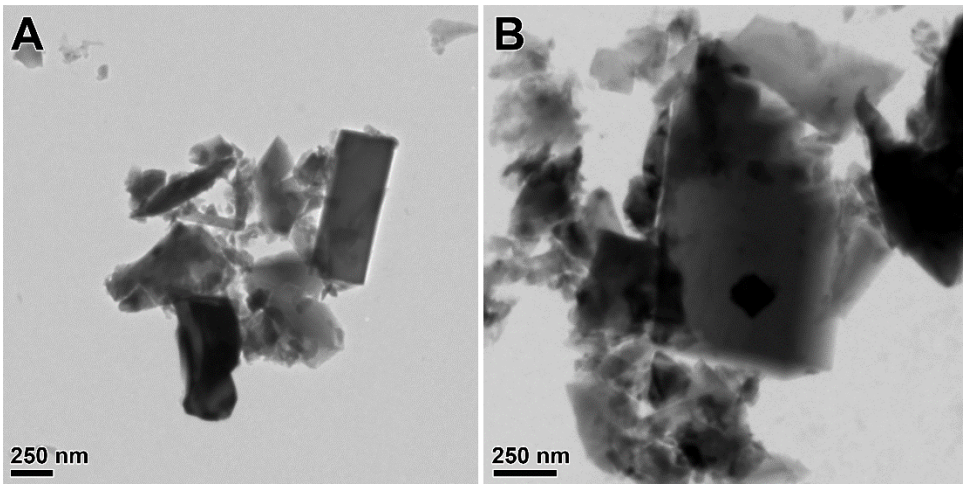

Figure 4.4. TEM images of A) Exfoliated CaB_6 showing irregular fragments and some regular nanosheets B) Partially exfoliated CeB_6 displaying fragments of varied sizes

To determine the effect that reaction duration plays on the composition of the lithiated product, and morphology of the exfoliated product, we treated bulk CaB_6 with a 3 month long *n*-BuLi reactions at room temperature. In our previous 11 day *n*-BuLi reaction on CaB_6, we noticed a new peak at ~20 2θ in the PXRD pattern on lithiated CaB_6 (Figure 4.5 A). Since it was not possible for us to match a single peak to a reference pattern, we decided to increase the reaction duration to three months to get a higher concentration of the lithiated intermediate. Characterizing the CaB_6 three month lithiated powder under XRD displayed many small, broad peaks that were not present in the PXRD pattern of bulk CaB_6 (Figure 4.5 A). The closest match we obtained from the ICDD database was to LiB_9, which is a lithium boride where borons are present in the crystal lattice as boron clusters.[17,18] We speculate that the concentration of boron in our lithiated boride ranges between LiB_9-LiB_{10}. Judging by the broadness of the LiB_9 peaks in PXRD, we determined that significant nanostructuring has occurred in our lithiated material.[19] Upon exfoliation of the three month lithiated CaB_6, the product yielded an abundance of small nanoparticles of diameter

less than 20 nm, and nanosheets of lateral dimensions between 50 – 150 nm (Figure 4.5 B-C). Performing Scherrer analysis on the broad XRD peaks gave us an average particle size of 14.47 nm (Table 3.1), which matched the diameter of the nanoparticles we had observed under TEM. Owing to the small particle size and high reactivity, the exfoliated nanoproduct got oxidized over a period of two weeks to form $Ca(OH)_2$ when stored under aqueous conditions. Peripheral oxidation of significantly larger CaB_6 nanostructures has been observed in the literature.[20]

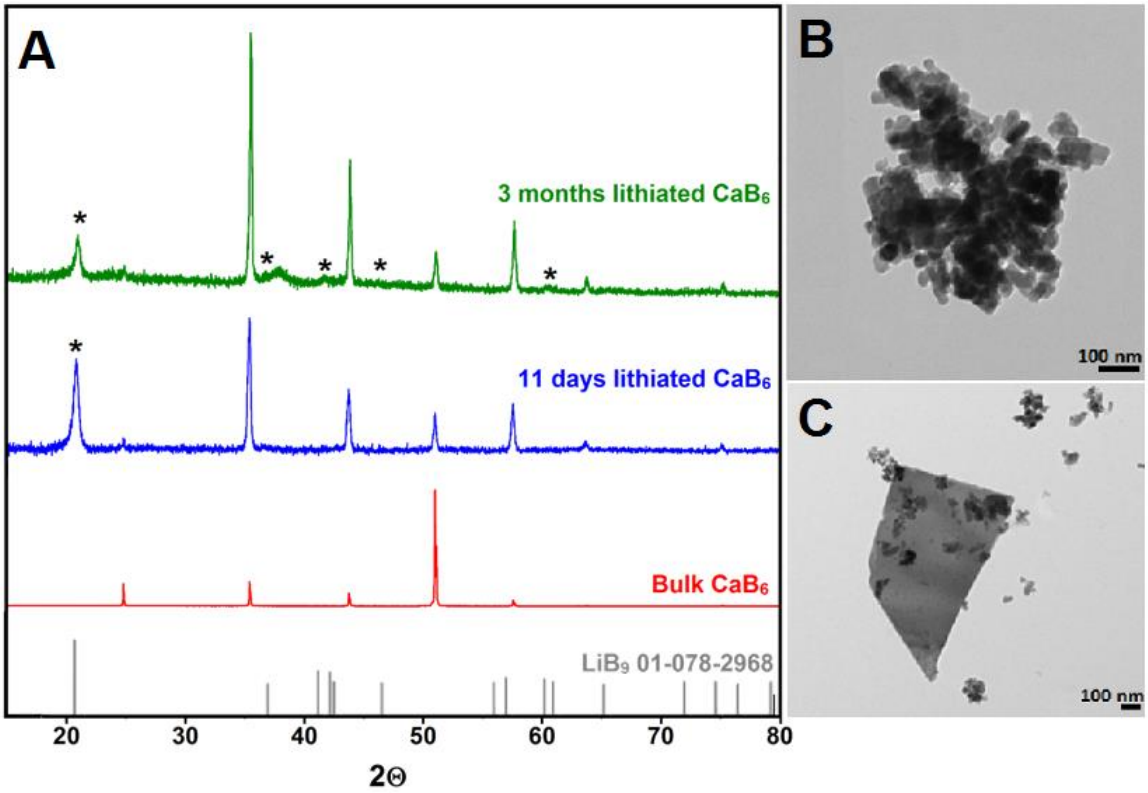

Figure 4.5. A) PXRD patterns of bulk CaB_6, 11 days lithiated CaB_6 and 3 months lithiated CaB_6 with reference pattern for LiB_9 (ICDD no. 01-078-2968) B) TEM image of the nanoproduct obtained from exfoliating 3 months lithiated CaB_6 C) Zoomed in TEM image captures the clusters of small nanoparticles produced in abundance in the exfoliated product

Table 3.1. Scherrer analysis of the broad peaks in 3 months lithiated CaB_6

No.	B obs. [°2Th]	B std. [°2Th]	Peak pos. [°2Th]	B struct. [°2Th]	Crystallite size [Å]
1	0.474	0	20.92	0.474	198
2	2.435	0	37.701	2.435	40
3	0.526	0	41.706	0.526	188
4	0.698	0	60.488	0.698	153
					Avg: 144.75

Reaction of CaB_6 with n-butyllithium at high temperature

Our next focus was to increase the amount of lithiation that occurs in CaB_6, without having to use long reaction durations such as three months. Therefore, we increased the concentration of lithium ions in the system by switching to a more concentrated 11 M *n*-BuLi solution as the lithium reagent. We also hypothesized that a higher temperature would lead to a greater degree of ionic exchange, or lithium incorporation into bulk CaB_6. Therefore, we treated bulk CaB_6 powder with a 11 day long *n*-BuLi reaction using 11 M *n*-BuLi at an elevated temperature of 80 ^{o}C. Observing the lithiated and bulk CaB_6 powders under SEM again displayed a drastic change in their morphologies (Figure 4.6 A-B). When comparing bulk CaB_6 (Figure 4.6 A) to lithiated CaB_6 (Figure 4.6 B), we see that the surface of the bulk is smooth whereas the lithiated is composed of small platelets and particles. It is interesting to note that the average particle size of the lithiated obtained at elevated temperatures is much smaller than that of the lithiated we had observed at room temperature (Figure 4.3 C). This is further reflected in the exfoliated product where we observe a mixed morphology comprising irregular nanoparticles and some square nanosheets of dimensions below 50 nm (Figure 4.6 C), instead of the larger fragments we had seen in the room temperature reaction (Figure 4.4 A).

PXRD on the CaB_6 high temperature lithiated powder indicated the presence of many different species (Figure 4.6 D). In addition to CaB_6, as expected, we also saw peaks for LiOH which was a side product of the elevated temperature reaction. An interesting feature we observed was a broadening of the CaB_6 peaks, as well as an apparent shifting or splitting of the peaks. We have matched these peaks to LiB_3, another lithium boride species with a crystal structure very similar to that of the metal hexaborides.[21] LiB_3 has boron octahedra present in its structure, with mobile lithium ions around it in lattice sites. We speculate that upon lithiation, our CaB_6 undergoes partial formation of LiB_3, possibly in the nanoregime. Since LiB_3 is sensitive to water[21], the LiB_3 pockets formed get disintegrated during the exfoliation reaction. This leads to disassembly of the CaB_6 structure as well, thereby nanostructuring our metal hexaboride.

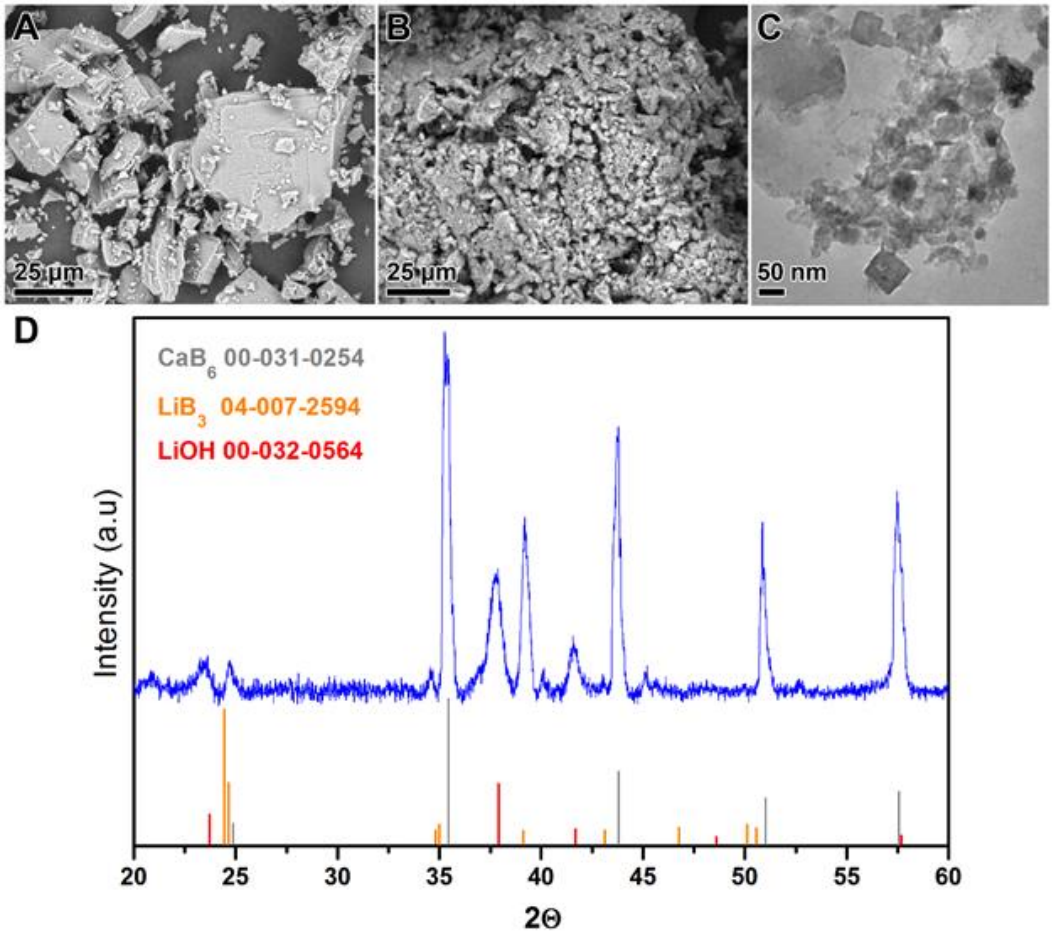

Figure 4.6. A) SEM image of bulk CaB_6 B) SEM image of high-temperature lithiated CaB_6 highlighting the roughened surface after lithiation as well as clusters of particles forming on the surface C) TEM image of exfoliated CaB_6 comprising of small square nanosheets and irregular particles D) PXRD pattern of HT lithiated CaB_6 with reference patterns for CaB_6 (ICDD no. 00-031-0254), LiB_3 (ICDD no. 04-007-2594) and LiOH (ICDD no. 00-032-0564)

Reaction of samarium hexaboride with n-butyllithium at high temperature

We performed a 1 month long *n*-BuLi reaction on SmB_6 using 11 M *n*-BuLi at an elevated temperature of 80 ^{o}C. Observing the lithiated and bulk SmB_6 powders under SEM (Figure 4.7 A-B) showed a morphological change wherein the lithiated SmB_6 has a rough surface composed of aggregates of particles when compared to bulk SmB_6 which comprises smooth platelets. An important point to note is that the grain size of bulk SmB_6 is much smaller than our other metal boride precursors, with most platelets in bulk SmB_6 being less than a micron in size. EDS mapping on the surface of the lithiated SmB_6 showed the presence of boron and samarium, as expected, as well as a large amount of oxygen due to surface oxidation and some carbon (Figure 4.7 D-G respectively). PXRD on the lithiated SmB_6 (Figure 4.7 C) showed the presence of SmB_6, LiOH and also lithium hydride, which is a decomposition product of n-butyllithium.

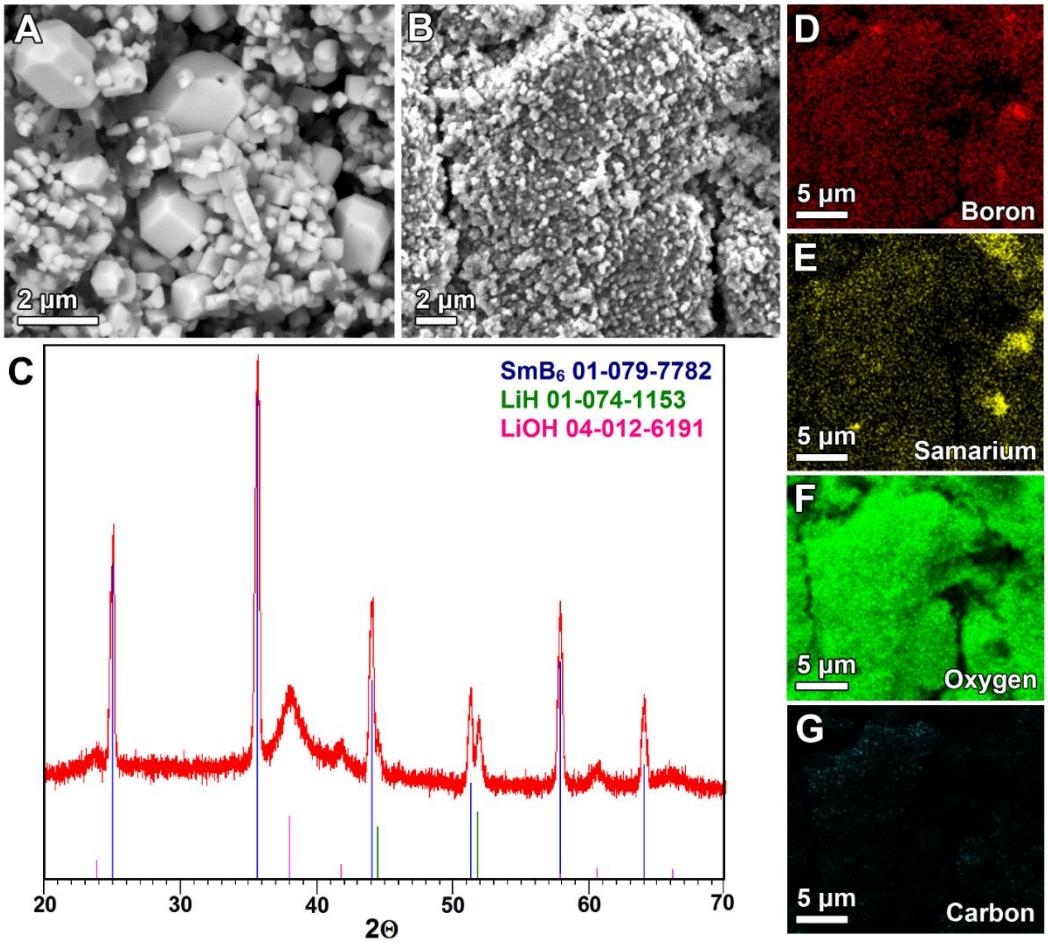

Figure 4.7. A) SEM image of bulk SmB_6 B) SEM image of lithiated SmB_6 having aggregates of particles on the surface C) PXRD pattern of lithiated SmB_6 with reference pattern for SmB_6 (ICDD no. 01-079-7782), LiH (ICDD no. 01-074-1153) and LiOH (ICDD no. 04-012-6191) D-G) EDS mapping of Boron, Samarium, Oxygen, and Carbon respectively

After treating lithiated SmB_6 with the exfoliation reaction, we characterized the exfoliated product using PXRD and TEM. PXRD showed that the exfoliated product was crystalline and matched the reference pattern of SmB_6. TEM showed that the product was composed of uniform, circular disk shaped particles of dimensions between and nm (Figure 4.8). SAED showed that the disks were very single crystalline with a cubic diffraction pattern, although there seems to be a

visible distortion in the pattern. This could arise from the destabilization that occurs in the SmB_6 crystal structure upon lithiation and exfoliation, thereby causing a strained lattice. PXRD on the exfoliated product showed the presence of SmB_6, and byproducts LiOH, and Li_2CO_3.

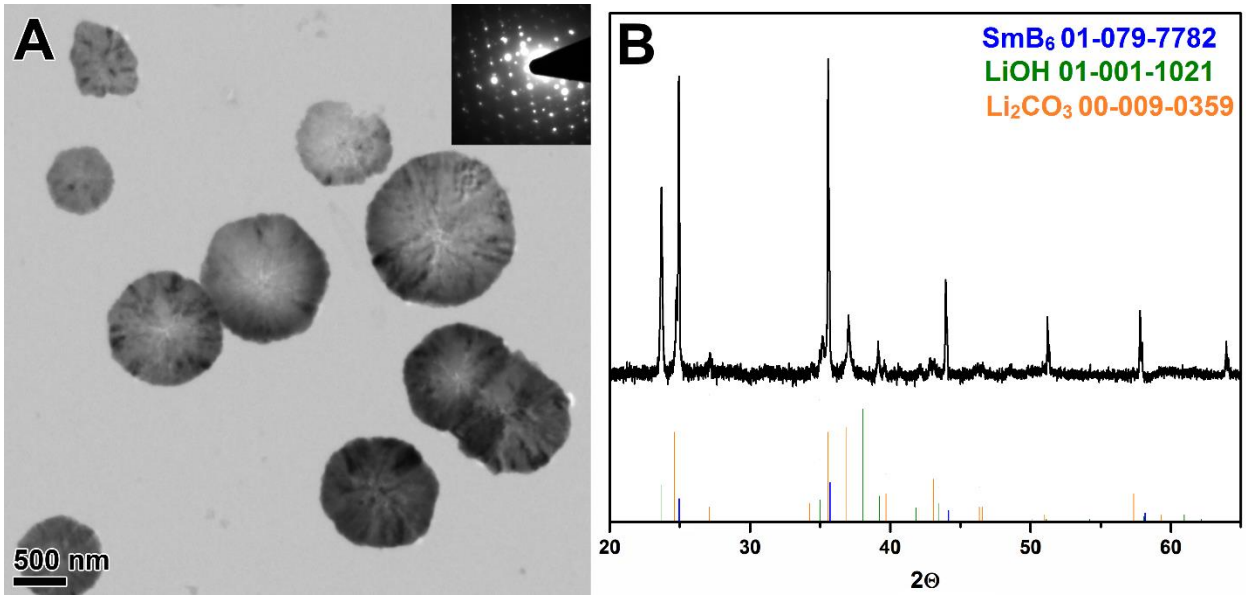

Figure 4.8. Exfoliated SmB_6 A) TEM image of exfoliated SmB_6 with inset SAED pattern B) PXRD pattern of exfoliated SmB_6 with reference pattern for SmB_6 (ICDD no. 01-079-7782), LiOH (ICDD no. 01-001-1021) and Li_2CO_3 (ICDD no. 00-009-0359)

Conclusions

We used two lithium ion incorporation techniques to lithiate bulk CaB_6, CeB_6 and SmB_6 powders. After lithation, the lithiated intermediate was structurally characterized using powder x-ray diffraction (PXRD) and scanning electron microscopy (SEM). The lithiated intermediate was then exfoliated by subsequently treating with deionized water to remove the lithium ions incorporated and produce a disassembly of the structure. The effect of reaction temperature, reaction duration, concentration of lithiating reagent, and nature of metal hexaboride precursor were also investigated.

The products formed through these lithiation-exfoliation reactions were nanostructured to various degrees. Powder x-ray diffraction and transmission electron microscopy (TEM) were used to characterize the morphology and composition of the exfoliated products obtained through the various reaction conditions. Out of the three bulk starting materials, CaB_6 proved to be the most versatile for exfoliation and sensitive to changes in reaction conditions. We were able to exfoliate CaB_6 into small nanosheets and platelets, CeB_6 was nanostructured to a moderate degree and formed regular square-shaped platelets while SmB_6 only underwent a partial exfoliation to produce fragmented disk shaped particles.

References

1. J. M. Lafferty, *J. Appl. Phys*. **1951**, *22*, 299–309.
2. A. Berrada, J. P. Mercurio, J. Etourneau, F. Alexandre, J. B. Theeten, T. M. Duc, *Surf. Sci*. **1978**, *72*, 177–188.
3. S. Souma, H. Komatsu, T. Takahashi, R. Kaji, T. Sasaki, Y. Yokoo, J. Akimitsu, *Phys. Rev. Lett*. **2003**, *90*, 027202.
4. M. Takeda, T. Fukuda, F. Domingo, T. Miura, *J. Solid State Chem*. **2004**, *177*, 471–475.
5. J. Nickerson, R. White, K. Lee, R. Bachmann, T. Geballe, G. Hull, *Phys. Rev. B*. **1971**, *3*, 2030.
6. S. Wolgast, Ç. Kurdak, K. Sun, J. W. Allen; D. J. Kim; Z. Fisk, *arXiv*. **2012**, *1211*, 5104.
7. D. J. Kim, J. Xia, Z. Fisk. *Nat. Mater*. **2014**, *13*, 466–470.
8. H. Zhang, Q. Zhang, J. Tang, L. Qin. *J.A.C.S*. **2005.** 127. *22*. 8002-8003.
9. M. Jha, R. Patra, S. Ghosh, A. K. Ganguli. *J. Mater. Chem.* **2012.** 22. *13*. 6356-6366.
10. R. Patra, S. Ghosh, E. Sheremet, M. Jha, R. D. Rodriguez, D. Lehmann, A. K. Ganguli, O. D. Gordan, H. Schmidt, S. Schulze, D. R. T. Zahn. *J. Appl. Phys.* **2014**. 115. *9*. 094302.
11. O. Torabi, S. Naghibi, M. H. Golabgir, A. J. Jamshidi. *Chin. Chem. Soc.* **2016**. 63. *4*. 379-384.
12. T.T. Xu, J.G. Zheng, A.W. Nicholls, S. Stankovich, R.D. Piner, R.S. Ruoff. *Nano Lett.* **2004** 4. *10*. 2051-2055.
13. J. Xu, Y. Zhao, C. Zou, Q. Ding. *J. Solid State Chem.* **2007**. 180. 2577-2580.
14. J. Q. Xu, Y. M. Zhao, X. H. Ji, Q. Zhang, S. P. Lau. *J. Phys. D.* **2009**. 42. *13*. 135403.
15. D. Ağaoğulları, Ö. Balcı, M. L. Öveçoğlu, C. Suryanarayana, & İ. Duman. *J. Eur. Ceram. Soc.* **2015**. 35. *15*. 4121-4136.
16. G.A. Ozin, *Adv. Mater*. **1992**, *4*, 612–649.

17. N. Vojteer, J. Stauffer, H. Hillebrecht, K. Hofmann, M. Panda, B. Albert, *Z. Anorg. Allg. Chem*. 2009, *635*, 653–659.

18. I. V. Dudenkov, K. A. Solntsev. *Russ. J. Inorg. Chem*. 2009, *54*, 1105–1113.

19. T. Ungár, *Scr. Mater*. 2004, *51*, 777–781.

20. T. T. Xu, J. G. Zheng, A. W. Nicholls, S. Stankovich, R. D. Piner, R. S. Ruoff, *Nano Lett*. 2004, *4*, 2051–2055.

21. G. Mair, H. G. von Schnering, M. Wörle. *Z. Anorg. Allg. Chem*. 1999, *625*, 1207–1211.

CHAPTER 5

LITHATION OF ALUMINUM DIBORIDE AND EXFOLIATION USING AQUEOUS AND NON-AQUEOUS CONDITIONS

Roshini Ramachandran and Tina T. Salguero. To be submitted to *Journal of Materials Research*.

Abstract

We used a lithium ion incorporation technique to lithiate bulk aluminum diboride powder. After lithation, the lithiated intermediate was structurally characterized using powder x-ray diffraction, multinuclear solid-state nuclear magnetic resonance spectroscopy and scanning electron microscopy. The lithiated intermediate was then exfoliated by subsequently treating with deionized water to remove the lithium ions incorporated and produce a disassembly of the structure. The product formed through this lithiation-exfoliation reaction composed of small, crumpled nanosheets that were quickly oxidized under ambient conditions to form aluminum hydroxide. Another variation of exfoliation was done under non-aqueous conditions using methyl iodide and hexane and this yielded clusters of rolled up sheets of aluminum diboride. Powder x-ray diffraction, multinuclear solid-state nuclear magnetic resonance spectroscopy, transmission electron microscopy and atomic force microscopy were used to characterize the morphology and composition of the exfoliated products obtained through both conditions.

Introduction

Aluminum diboride is a high performance refractory ceramic with a melting point of 1655 ^{o}C. It has a hexagonal crystal structure similar to magnesium diboride with sheets of boron atoms alternating with aluminum atoms in a hexagonal arragement.[1] Aluminum diboride has been shown to exhibit metallic conductivity.[2] As with the case of the metal boride series, aluminum diboride presents difficulties in processing and this largely limits its applications in devices or coatings.

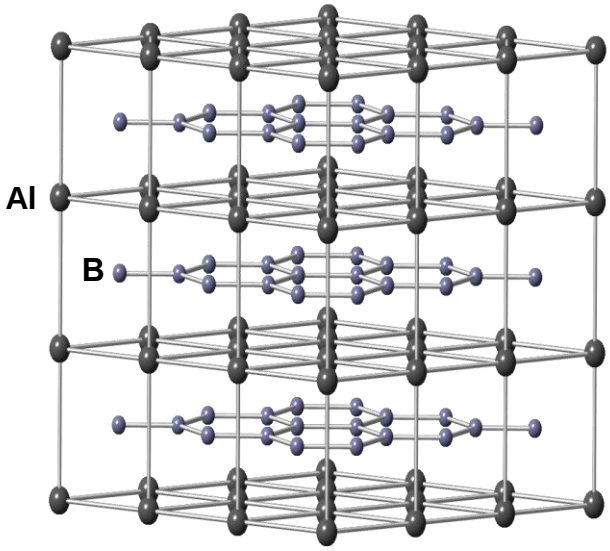

Figure 5.1. Hexagonal crystal structure of AlB_2

While observing the crystal structure of AlB_2 (Figure 5.1), we see that the compound is layered, having spaces between the boron sheets and aluminum atoms. However, this is not a typical layered van der Waals arrangement, with much stronger B-B covalent bonding and ionic interactions existing within the layers.[1] Therefore, although there is scope for top-down exfoliation into two-dimensional nanoproducts, the reaction conditions will have to be stronger than solution-based methods used for well-studied layered materials such as graphite, metal dichalcogenides and layered oxides and hydroxides.[3,4,5,6]

We have employed a top-down lithium ion insertion-exfoliation approach to form nanosheets of AlB_2. Previously, lithium intercalation using Li/NH_3 or *n*-BuLi solutions have been successfully utilized for the exfoliation of van der Waals materials like bismuth chalcogenides.[7] However, in the case of magnesium diboride (MgB_2), a similar lithium insertion reaction led to the Li^+ ions being incorporated into the MgB_2 structure in defect sites.[8,9] Although very different from the lithiation chemistry of van der Waals materials, the lithium incorporation into cationic sites instead of between the layers led to crystal strain, followed by disassembly of the MgB_2 structure to yield two-dimensional MgB_2 nanostructures.[8] However, the main setback of this chemistry is the oxidation of MgB_2 nanoplatelets into MgO and $Mg(OH)_2$ nanosheets.[8]

In this work, we have utilized the Li^+ ion incorporation technique on AlB_2, with the aim to cause disassembly of the crystal lattice. We have explored both aqueous and non-aqueous exfoliation conditions to avoid the issue of oxidation that was observed in the case of MgB_2.

Experimental

Materials: Aluminum diboride (Office of Naval Research, USA), lithium ribbon (99.9%, Sigma Aldrich), hexanes (≥98.5%, Fisher), anhydrous ammonia (99.99%, Airgas), methyl iodide/iodomethane (≥ 99%. Sigma Aldrich)

Reaction of aluminum diboride with Li/NH_3:

0.1 g (0.002 moles) of AlB_2 powder and 0.1 g (0.014) Li metal were placed in a modified Schlenk vessel with Teflon cap. The Schlenk vessel was kept in an ethanol bath equipped with temperature probe maintained at -50 ^oC. The reaction vessel was pumped down to 5 mbar using a diffusion pump. Once the ethanol bath reached -50 ^oC, the pump was switched off and 30 mL of ammonia gas was slowly condensed into the vessel. The AlB_2 powder is left sitting in the Li/NH_3 solution for 2 days, after which the NH_3 gas is evaporated off into dil HCl solution. The product is washed with NH_3 two or three times to remove any remaining elemental lithium. Then the reaction vessel is flushed with Argon gas, pumped down to remove any remaining gas and taken into an Argon glove box. The lithiated AlB_2 powder ($Li_xAl_{1-x}B_2$) is removed from the Schlenk vessel and stored in the Argon glove box pending future characterization.

Reaction of aluminum diboride with NH_3 (control):

0.1 g (0.002 moles) of AlB_2 powder was placed in a modified Schlenk vessel with Teflon cap. The Schlenk vessel was kept in an ethanol bath equipped with temperature probe maintained at -50 ^oC. The reaction vessel was pumped down to 5 mbar using a diffusion pump. Once the

ethanol bath reached -50 ^{o}C, the pump was switched off and 30 mL of ammonia gas was slowly condensed into the vessel. The AlB_2 powder is left sitting in NH_3 for 2 days, after which the NH_3 gas is evaporated off into dil HCl solution. Then the reaction vessel is flushed with Argon gas, pumped down to remove any remaining gas and taken into an Argon glove box. The AlB_2 powder is removed from the Schlenk vessel and stored in the Argon glove box pending future characterization.

Reaction of $Li_xAl_{1-x}B_2$ with water (aqueous exfoliation):

The lithiated aluminum diboride powder ($Li_xAl_{1-x}B_2$) was treated with 20 mL of deionized water kept in an ice bath. The product mixture was centrifuged and decanted to remove soluble byproduct LiOH. The solid product was washed and subjected to another cycle of centrifugation and decanting. The residual product was then re-dispersed in water and probe sonicated at 60 amp for 1 hour or bath sonicated for 2 hours. The subsequent exfoliated product was vacuum dried or stored as a dispersion in water until future analysis.

Reaction of $Li_xAl_{1-x}B_2$ with methyl iodide (non-aqueous exfoliation):

The lithiated aluminum diboride powder ($Li_xAl_{1-x}B_2$) was treated with 20 mL of methyl iodide in an Argon glove box. The product mixture was suspended in anhydrous hexane and centrifuged and decanted to remove excess methyl iodide/hexane. The solid product was washed with hexane and subjected to another cycle of centrifugation. The residual product was then re-dispersed in hexane and probe sonicated at 60 amp for 1 hour or bath sonicated for 2 hours. The

subsequent exfoliated product was vacuum dried or stored as a dispersion in hexane until future analysis.

Characterization:

The composition of the bulk, lithiated and exfoliated materials was confirmed using a Bruker D8- Advance powder X-ray diffractometer (Co-Kα radiation source) operated at 40 mA and 40 kV. The PXRD patterns were recorded over the 2θ range of 5−80° with a scanning rate of 0.1 sec step^{-1}. The morphology of the lithiated metal boride and exfoliated products were examined using a FEI Inspect F field emission gun scanning electron microscope (FEG-SEM) equipped with a EDAX energy dispersive x-ray spectrometer (EDS) operating at 20 kVand a FEI Teneo FEG-SEM with an Oxford EDS system operated at 5-10 keV. The lithiated samples were prepared for SEM by sprinkling the powders on carbon sticky tape while the exfoliated samples were dropcast on a silicon wafer. A Misonix S-4000 Ultrasonic Liquid Processor was used for the sonication step.

The morphology of the exfoliated nanoproducts were additionally characterized using a FEI Tecnai 20 (200 kV) TEM with selected area electron diffraction (SAED) capability. The height of the samples was determined using a Bruker Innova atomic force microscope (AFM) in tapping mode. AFM samples were prepared by adding a drop of dilute suspension of exfoliated nanosheets on a clean silicon wafer. Solid-state NMR data were collected with a Bruker Avance III 400 spectrometer operating at 10000 Mhz. Spectral deconvolution was performed using the SpinWorks4 software and peak fitting of NMR spectra was done using OriginPro 8.5 software.

Results and discussion

We treated bulk aluminum diboride powder with a Li/NH_3 reaction for 3 days. Observing the bulk and lithiated AlB_2 powders under SEM showed difference in the morphology of the lithiated AlB_2 (Figure 5.2). Bulk AlB_2 is made of irregular platelets (Figure 5.2 A), however lithiated AlB_2 is uniformly comprised of smaller platelets of dimensions less than a micron (Figure 5.2 B). Performing EDS mapping on the lithiated AlB_2 sample indicated the presence of Boron, Aluminum and Oxygen respectively (Figure 5.2 D-F). However, we notice that the Aluminum mapping is not uniformly distributed over the surface; there are pockets of Al randomly distributed over the platelets. Surprisingly, the boron mapping is consistent with the expected results. This leads us to believe that some Al^{3+} in AlB_2 are being substituted by Li^+ ions upon lithiation. A similar observation has been previously made for lithiated MgB_2.[8]

Lithium borides of type LiB_2 have been theoretically predicted to exist.[10,11] In this compound, the Li^+ would occupy the cationic sites as expected of the metal in the MB_2 structure.[10] We hypothesize that upon lithium incorporation into MgB_2, we form a mixed boride of composition $Li_xAl_{1-x}B_2$.

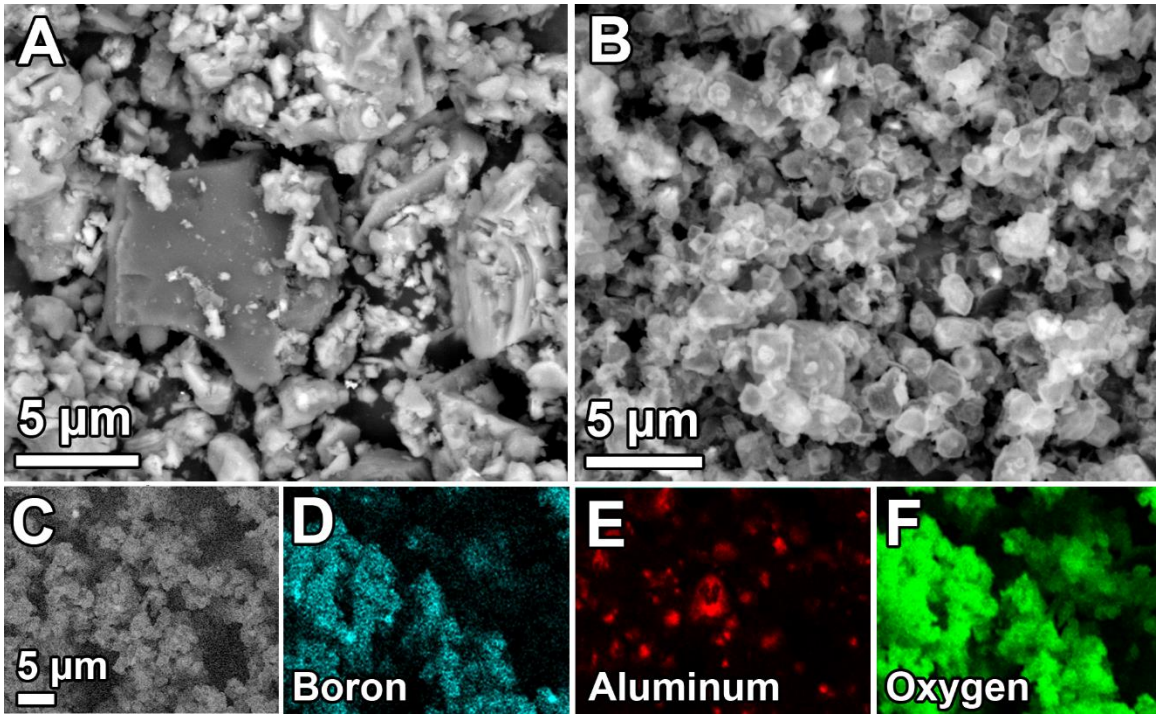

Figure 5.2. Lithiated AlB_2 A) SEM image of bulk AlB_2 B) SEM image of lithiated AlB_2 illustrating the decrease in particle size upon lithiation C) Zoomed in SEM image of lithiated AlB_2 D-F) Elemental mapping of Boron, Aluminum and Oxygen respectively

We further confirmed the presence of Li in lithiated AlB_2 using ^{7}Li NMR spectroscopy (Figure 5.3), which gave us an intense peak asymmetric peak containing a shoulder peak. Performing peak-fitting on this asymmetric peak gave us two chemical shift values: the peak at 2.71 ppm can be assigned to $LiNH_2$ which is a common side product of the Li/NH_3 reaction. The more intense peak at 1.4 ppm is unique to our sample and can be assigned to the Li^+ ions present in the AlB_2 structure. We also characterized lithiated and bulk AlB_2 using ^{11}B and ^{27}Al solid-state NMR spectroscopy (Figure 5.4). We observed asymmetry in the central ^{11}B peak in lithiated AlB_2, peak-fitting showed the presence of a new peak at 31.5 ppm indicating a change in the chemical

environment of the lithiated AlB_2. Similarly, performing peak-fitting on the asymmetric ^{27}Al central peak displayed the presence of a new peak at 1634 ppm, which is very close to the bulk AlB_2 peak at 1639 ppm. Therefore, we see that Li^+ incorporation into AlB_2 creates a significant change in the ^{11}B chemical environment but not so much in the case of the ^{27}Al nucleus. Considering the small size of the Li^+ ion, it makes sense that Li^+ substitution in AlB_2 would minimally impact the larger Al^{3+} chemical environment. PXRD on the lithiated AlB_2 (Figure 5.6) largely showed the presence of AlB_2, along with common side products $LiNH_2$ and LiOH.

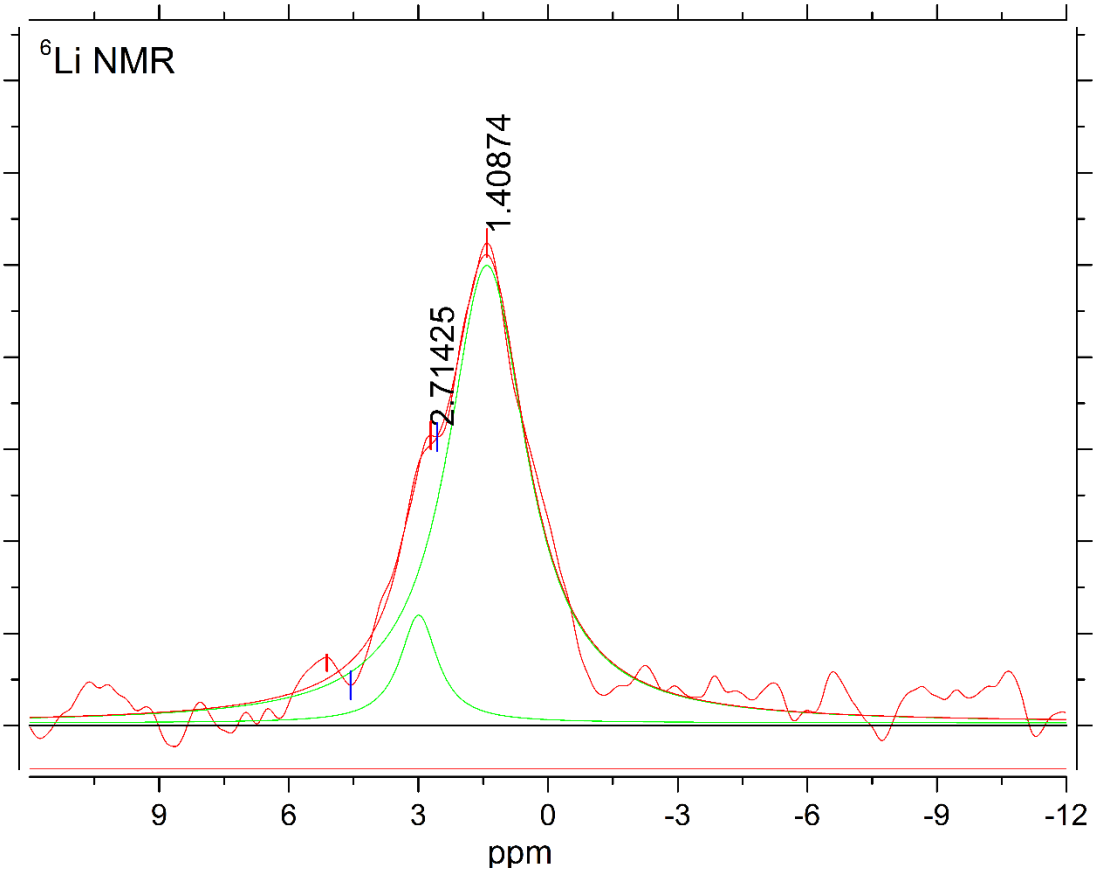

Figure 5.3. Peak-fitted ^6Li Solid-state NMR spectrum of lithiated AlB_2 showing two distinct peaks

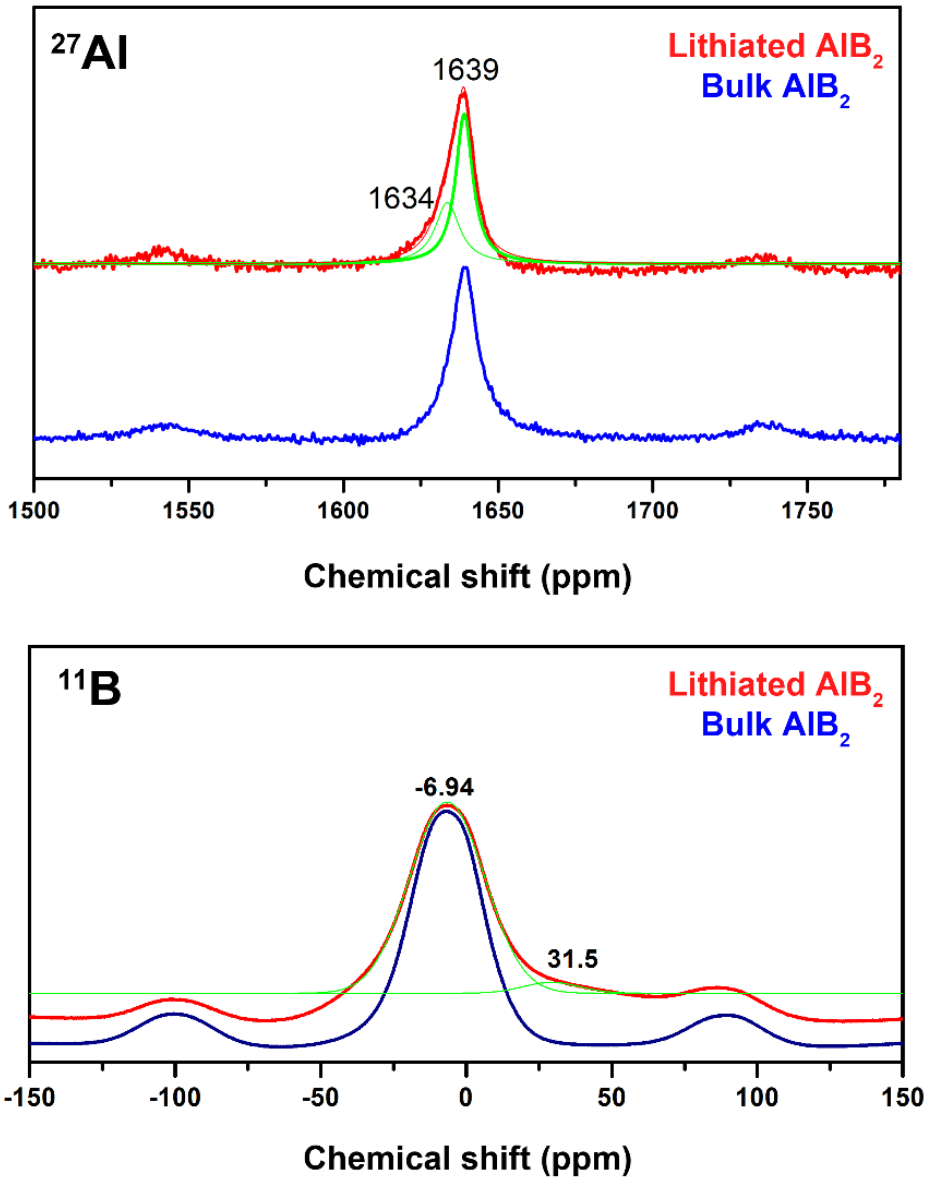

Figure 5.4. Peak-fitted solid-state ^{27}Al (top) and ^{11}B (bottom) NMR spectra for AlB_2

Table 5.1. Solid state NMR shifts for ^{11}B, ^{6}Li and ^{27}Al nuclei for bulk and lithiated AlB_2

Sample	^{11}B	^{6}Li	^{27}Al
AlB_2 bulk	-6.94	-	1639
AlB_2 lithiated	-6.94 31.5	1.4 2.7	1634 1639

We used two different conditions to exfoliate the lithiated AlB_2; the first being under aqueous conditions and the second utilizing non-aqueous conditions. The aqueous exfoliated product yielded an abundance of small, fragmented nanosheets of lateral dimensions less than 100 nm (Figure 5.5A). Perfoming SAED on the nanosheets produced a polycrystalline diffraction pattern that matched α-AlO(OH). It is important to mention that the product changed color from black to light brown upon being stored for two days under aqueous conditions after exfoliation. This leads us to believe that the exfoliated AlB_2 gets completely oxidized over a period of two-three days when exposed to water at room temperature. AFM measurements on the nanosheets showed that they have a flat topography with a thickness of about 3 nm (Figure 5.5C-D). Owing to the thin nature of the nanosheets, as well as their high surface area, we can hypothesize that hydrolysis of AlB_2 nanosheets occurs to form α-AlO(OH). PXRD further confirmed that the oxidized product was indeed α-AlO(OH) (Figure 5.6). However, on characterizing the lithiated AlB_2 using XRD and NMR, we do not see the presence of any α-AlO(OH), leading us to conclude that the aqueous conditions are responsible for the chemical transformation. Such an oxidation to the metal oxide and hydroxide has been observed in the case of MgB_2 for various conditions.[8,12]

In contrast, when we exfoliated lithiated AlB_2 using methyl iodide with hexane as a solvent, we obtain a product composed of nanosheets that are rolled up (Figure 5.5B). The scrolling could be occurring because of the hydrophobicity of the solvent. Doing SAED on the product gives us a polycrystalline pattern with d-spacings indexed to AlB_2. PXRD also confirmed that the exfoliated product is AlB_2 (Figure 5.6), however, due to the insolubility of $LiNH_2$, LiOH side products and the LiI byproduct in hexane, we obtain an impure product mixture that is difficult to isolate by physical separation techniques.

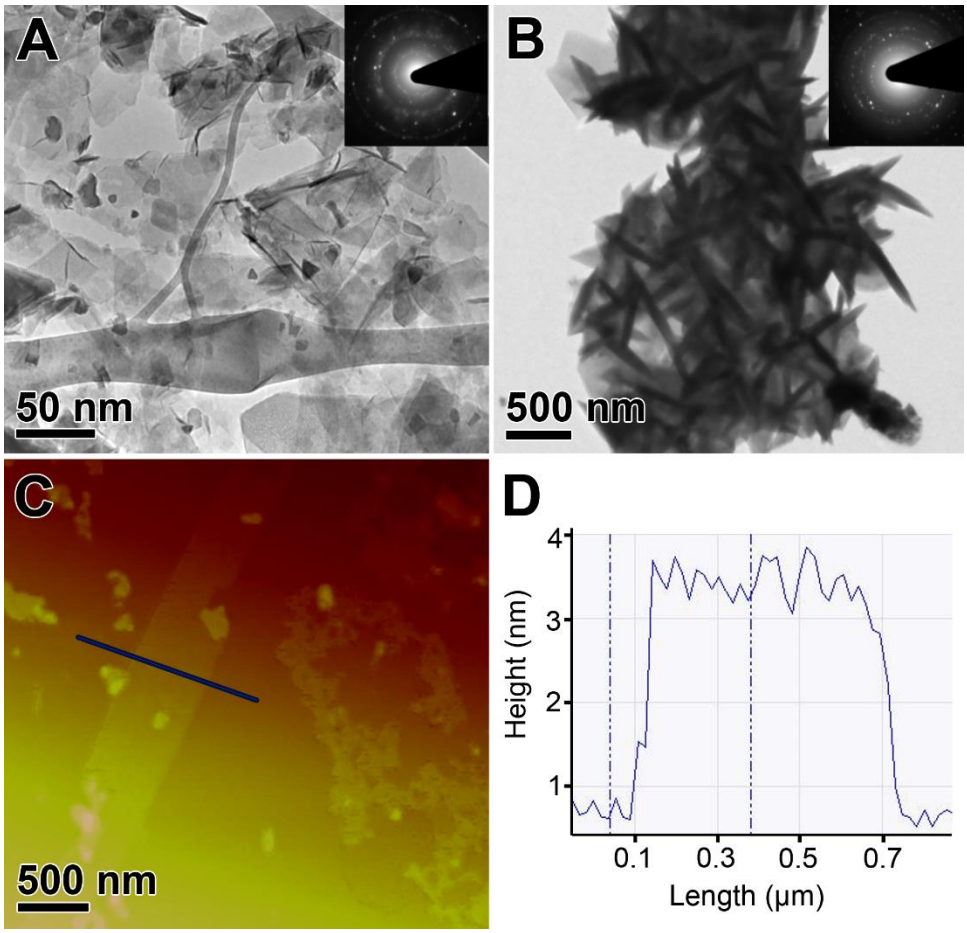

Figure 5.5. A) TEM image of crumpled nanosheets formed upon exfoliation of lithiated AlB_2 under aqueous conditions. Inset polycrystalline SAED pattern matches α-AlO(OH) B) TEM image of clusters of rolled up nanosheets formed upon non-aqueous exfoliation of lithiated AlB_2. Inset polycrystalline SAED pattern matches AlB_2 C) AFM image of aqueous-exfoliated nanosheets D) Height profile indicates that the thickness of the nanosheets is about 3 nm

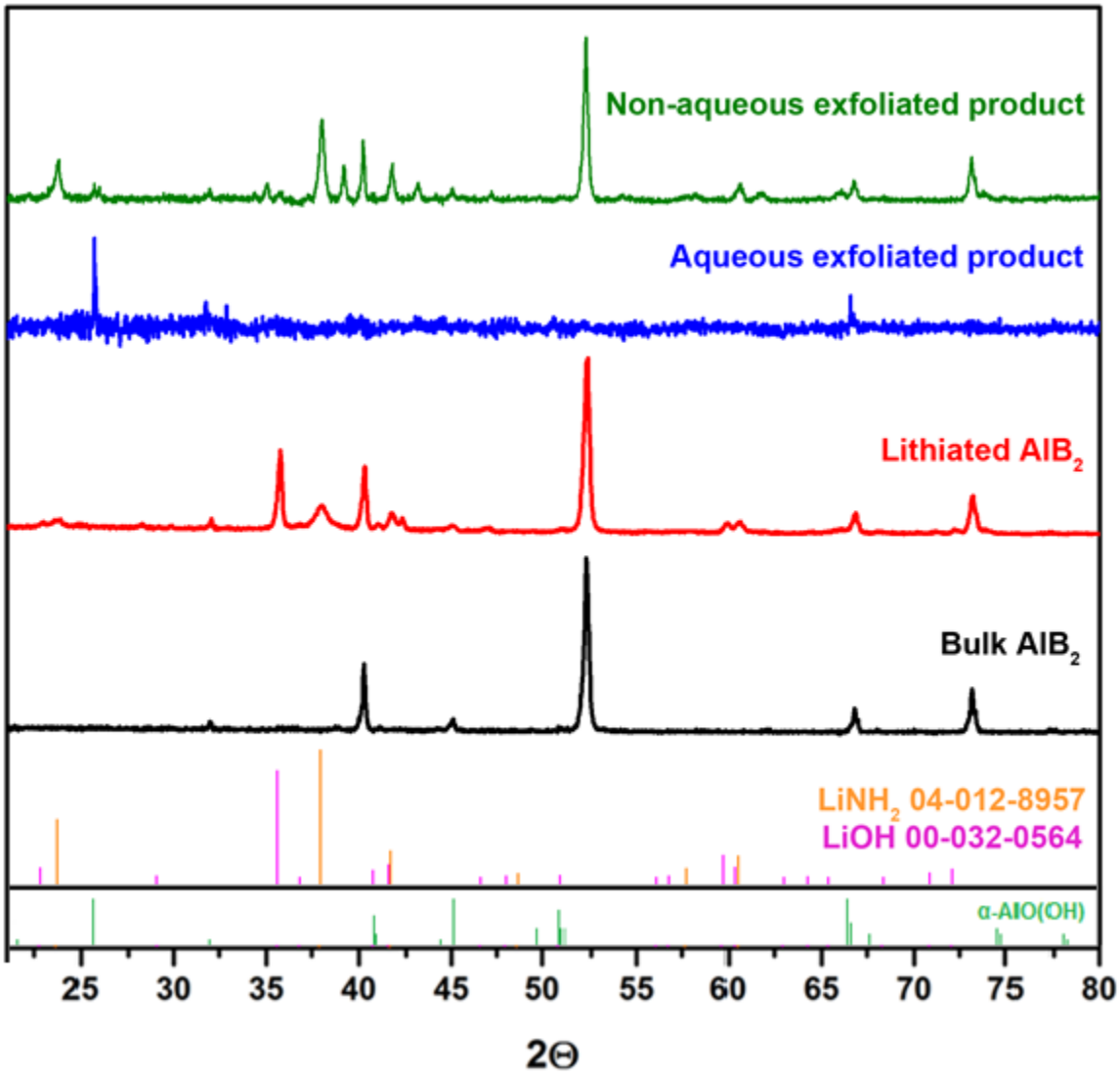

Figure 5.6. PXRD analysis (bottom-top) of bulk AlB_2, lithiated AlB_2 showing presence of side products $LiNH_2$ (ICDD. 04-012-8957) and LiOH (ICDD. 00-032-0564), aqueous exfoliated product that matches α-AlO(OH), and non-aqueous exfoliated product that contains AlB_2 and insoluble byproducts LiOH and $LiNH_2$

To test the stability of the lithiated AlB_2 to air/moisture, we further exposed the lithiated AlB_2 powder to air for a period of a few weeks at room temperature. Observing the exposed powder under SEM shows a drastic change in morphology when compared to lithiated AlB_2 stored in an Argon glove box. The exposed lithiated AlB_2 comprises of clusters of nanoflowers that are made up of small, thin, nanosheets (Figure 5.7B). These sheets look very similar to the nanosheets we obtained upon aqueous exfoliation of the lithiated AlB_2. Further characterization using EDS mapping (Figure 5.7 D-F) showed a high presence of Al and O in the nanosheets, while the B levels were much lower. Therefore, we comprehend that lithiated AlB_2 can undergo a spontaneous exfoliation-oxidation under ambient atmospheric conditions.

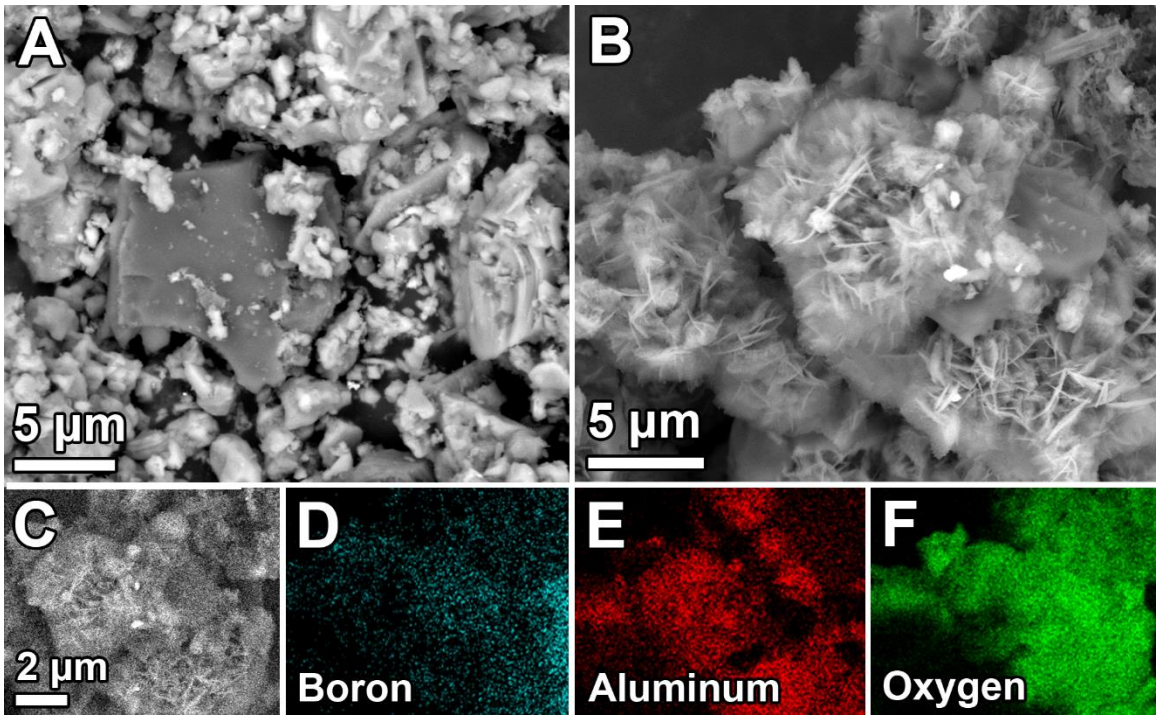

Figure 5.7. Lithiated AlB_2 exposed to air A) SEM image of bulk AlB_2 B) SEM image of lithiated AlB_2 after exposing to air, displaying clusters of aluminum oxide/hydroxide nanosheets held together C) Zoomed in SEM image of lithiated AlB_2 D-F) Elemental mapping of Boron, Aluminum and Oxygen respectively

To ensure that liquid NH_3 would not react or cause a morphological or compositional change in AlB_2, we performed a control reaction of bulk AlB_2 in liquid NH_3 for 3 days without adding elemental lithium. SEM on the AlB_2 control product did not show any morphological changes (Figure 5.8 B), and PXRD of the product matched that of bulk AlB_2 (Figure 5.8 C).

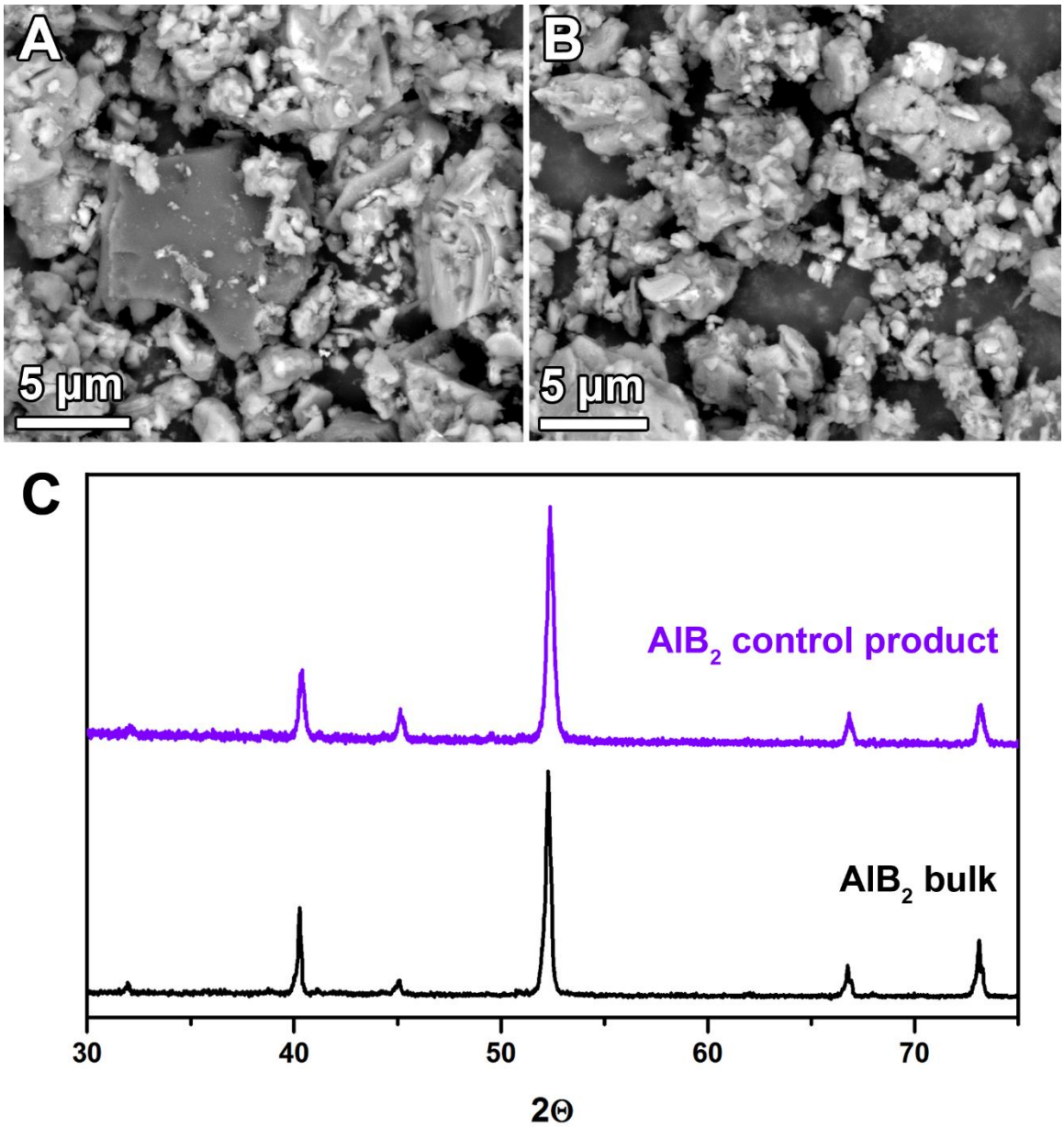

Figure 5.8. A) SEM image of bulk AlB_2 B) SEM image of AlB_2 control product C) PXRD patterns of bulk AlB_2 and AlB_2 control product showing no change in composition

Conclusions

We successfully lithiated bulk aluminum diboride powder using a Li/NH_3 reaction and confirmed the presence of Li in the compound using ^6Li solid state NMR spectroscopy. We learned that there is a morphological change through nanostructuring that occurs in aluminum diboride upon lithiation, however, there is no change in the boron composition. We hypothesize that lithium ions are replacing aluminum ions in the metal boride lattice, leading to a destabilization.

We exfoliated the lithiated AlB_2 powder using aqueous conditions to obtain nanosheets of aluminum hydroxide that were less than 3 nm in thickness. To prevent the issue of oxidation by water, we exfoliated lithiated AlB_2 using methyl iodide and non-polar solvent that produced clusters of rolled up sheets of aluminum diboride. This method is more favorable, however the separation of the nanoproduct from insoluble byproducts presents challenges.

We explored the stability of lithiated AlB_2 under ambient conditions and discovered that a spontaneous exfoliation and subsequent oxidation occurs due to air/moisture. This can be combated by storing the lithiated AlB_2 in an Argon glove box.

To conclude, this synthetic method of lithiation-exfoliation is a promising route to synthesize AlB_2 nanosheets. The conditions of exfoliation, specifically the reaction environment and storage of product, must be carefully monitored to prevent oxidation to α-AlO(OH).

References

1. Burkhardt, U., Gurin, V., Haarmann, F., Borrmann, H., Schnelle, W., Yaresko, A., & Grin, Y. *J. Soid State Chem.* **2004.** 177. *2*. 389-394.
2. Sirtl, E., Woerner, L. M. *J. Cry. Growth* **1972**. 16. *3*. 215-218.
3. Hernandez, Y., Nicolosi, V., Lotya, M., Blighe, F.M., Sun, Z., De, S., McGovern, I.T., Holland, B., Byrne, M., Gun'Ko, Y.K. and Boland, J.J. *Nat. Nano.* **2008.** 3. *9*. 563-568.
4. Coleman, J.N., Lotya, M., O'Neill, A., Bergin, S.D., King, P.J., Khan, U., Young, K., Gaucher, A., De, S., Smith, R.J. and Shvets, I.V. *Science* **2011.** 331. *6017*. 568-571.
5. Novoselov, K. S., Jiang, D., Schedin, F., Booth, T. J., Khotkevich, V. V., Morozov, S. V., & Geim, A. K. *Proc. Natl. Acad. Sci. U.S.A.* **2005**. 102. *30*. 10451-10453.
6. Ma, R., & Sasaki, T. *Adv. Mater.* **2010.** 22. *45*. 5082-5104.
7. Ding, Z., Bux, S. K., King, D. J., Chang, F. L., Chen, T. H., Huang, S. C., & Kaner, R. B. *J. Mater. Chem.* **2009.** 19. *17*. 2588-2592.
8. Sexton, D. R. (2014). Synthesis, delamination, and characterization of substituted magnesium diboride (Doctoral dissertation, UGA).
9. Salguero, T. T., Barrett, C.A., Sexton, D.R. U.S. Patent Application No. 13/653,463.
10. Serebryakova, T. I., Lyashenko, V. I., & Levandovskii, V. D. *Powder Metall. Met. C+*. **1995.** 33. *1-2*. 49-53.
11. Wang, D. H., Zhou, H. Y., Hu, C. H., Zhong, Y., Oganov, A. R., & Rao, G. H. *Phys. Chem. Chem. Phys*. **2017**. 19. *12*. 8471-8477.
12. Klug, K.L. Dravid, V.P. *Appl. Phys. Lett*. **2002.** 81. *9*. 1687-1689.

CHAPTER 6

FORMATION AND SCROLLING BEHAVIOR OF METAL FLUORIDE AND OXYFLUORIDE NANOSHEETS

Abstract

We report 1-2 unit cell thick CaF_2 nanosheets, which can be converted topochemically into $LaF_{3-2x}O_x$ nanosheets that scroll spontaneously. The formation of CaF_2 nanosheets is achieved through interlayer confinement and templating within $CaSi_2$ during reaction with HF(aq). The structure and morphology of these nanosheets are characterized by HRTEM, AFM, and powder XRD. Solid-state MAS and solution ^{19}F NMR spectroscopies provide further information about interstitial fluoride sites within CaF_2 nanosheets as well as help identify side products of the $CaSi_2$ + HF reaction. CaF_2 nanosheets react with lanthanide salts under aqueous, room-temperature conditions to yield nanostructured hexagonal LnF_3 (Ln = Ce, Pr, Nd, Sm, Eu), orthorhombic LnF_3 (Ln = Gd, Dy, Ho, Er, Yb), and cubic YbF_{3-x} products. Futhermore, the reaction of CaF_2 nanosheets with lanthanum salts is unique in producing $LaF_{3-2x}O_x$. The evidence for this composition includes powder XRD, EDS, XPS, and ^{19}F NMR data. The structure of hexagonal $LaF_{3-2x}O_x$ differs from hexagonal LaF_3 only in the replacement of two fluorides by one oxygen. While this topochemical transformation preserves the two-dimensional morphology it also causes lattice strain that initiates scrolling. The resulting product consists of remarkable ~20 x 5 nm scroll-like tubes of $LaF_{3-2x}O_x$. These nanoscrolls are the first among metal fluoride materials. These results demonstrate both novel metal fluoride nanochemistry and a new scrolling mechanism.

Introduction

Metal fluorides are an attractive class of compounds for diverse applications in microelectronics, optoelectronics, coatings and catalysis.[1-2] Their advantageous properties include a non-hygroscopic nature, stability with respect to oxidation, and high transparency over a wide wavelength region.[3-4] The alkaline earth metal fluorides CaF_2 and BaF_2, of interest for bioimaging applications,[5] have been produced by a wide range of methods that allow morphology control on the nanoscale, including co-precipitation,[4] sol-gel,[6] microemulsion,[1, 3] and hydrothermal techniques.[7] Additional functionality can be accessed in two ways: nanostructured CaF_2 and BaF_2 can act as host crystals, typically for lanthanide cations, or they can form heterovalent solid solution systems.[8-9] Interestingly, lanthanide fluorides and their associated solid solutions exhibit complex morphotropic changes based on the chemical composition of the lanthanide and/or alkaline earth cations; structures include cubic fluorite-type, hexagonal tysonite-type, and orthorhombic β-YF_3 type phases.[9-12] These materials are promising targets for bio-detection, upconversion, and laser applications, especially in nanostructured forms, due to their strong photoluminescence, excellent stability, and low toxicity.[7, 13-20] Proven synthetic approaches to lanthanide fluoride nanomaterials commonly utilize hydrothermal conditions that yield a variety of nanomorphologies.[7, 14,16, 19-21]

There have been limited reports of more complex nanomorphologies among metal fluoride materials, however. One promising target is the nanoscroll—a thin and flexible nanosheet that has rolled up—which has properties distinct from nanowires, -tubes, and -rods.[22-23] Nanoscrolls are especially interesting because of their unique open-ended structure, tunability with respect to diameter and interlayer spaces, reversible scrolled/unscrolled states, and enhanced stiffness.[22-24] Carbon-based nanoscrolls have been most studied,[25-31] followed closely by various

metal oxide,[22,32-36] hydroxide,[37-40] and chalcogenide nanoscrolls.[41-43] To date, there are no reported examples of metal fluoride-based nanoscrolls despite the widespread importance of this class of materials. Metal fluoride scrolls would be ideal for bio-detection and imaging applications because of the surface-tunable nature of two-dimensional nanosheets coupled with a rigid one-dimensional morphology once in the scrolled state. In addition, the interlayer spaces provide new possibilities for hosting small molecule or nanoparticle payloads.[44-46]

In this work, we describe new nanochemistry that can be used to make freestanding metal fluoride nanoscrolls. The approach requires two steps: first the preparation of metal fluoride nanosheets, then the initiation of scrolling. We begin with a layered material, calcium silicide ($CaSi_2$), which has a structure comprised of covalently-bonded, corrugated silicide $(Si_2^{2-})_n$ sheets alternating with Ca^{2+} that is ideal for interlayer reactions. This feature is well known from the reactions of $CaSi_2$ with HCl or metal chlorides that produce a range of silicon-based products: Wöhler- or Weiss-type siloxene nanosheets $[Si_6H_3(OH)_3]_n$,[47-52] Kautsky-type siloxene nanosheets $[Si_6O_3H_6]_n$,[53] functionalized polysilane-type nanosheets $[Si_6R_6]_n$ (R = H, alkyl, aryl),[54] and various intercalated or partially oxidized intermediate products structures,[55-57] depending on conditions. According to the accepted mechanism for the formation of Wöhler-type siloxene, HCl(aq) reacts with the interlayer Ca^{2+} of $CaSi_2$ to produce soluble $CaCl_2$ while the silicide layers become hydroxylated under the acidic aqueous conditions.

The present work utilizes the layered nature of $CaSi_2$ in a quite different way by transforming the Ca^{2+} into CaF_2 while solubilizing the silicide. The interlayer confinement and templating effects of the silicide sheets within the $CaSi_2$ lattice serve to direct the formation of CaF_2 into the desired nanosheet morphology. In the second stage of the process, reaction of the CaF_2 nanosheets with lanthanum salts in water at ambient conditions causes a topochemical

conversion to yield partially oxidized lanthanum fluoride nanosheets. The lattice strain produced by this transformation induces spontaneous nanosheet scrolling. To our knowledge, this is the first example of scrolling by such a mechanism, which opens the possibility of studying previously inaccessible nanoscrolls.

Experimental

Materials: 6R-$CaSi_2$ (Materion Corporation), HF (Sigma Aldrich, 48% in water), Lanthanum(III) chloride hexahydrate (Sigma Aldrich, 99.9%), Lanthanum(III) trifluoromethanesulfonate (Sigma Aldrich, 99.9%), Lanthanum(III) bromide hydrate (Sigma Aldrich, 99.99%), Neodymium(III) nitrate hexahydrate (Sigma Aldrich, 99.9%), Cerium(III) chloride heptahydrate (Sigma Aldrich, 99%), Praseodymium(III) trifluoromethanesulfonate (Sigma Aldrich, 99.9%), Europium(III) chloride hexahydrate (Sigma Aldrich, 99.99%), Gadolinium(III) nitrate hexahydrate (Sigma Aldrich, 99.9%), Terbium(III) chloride hexahydrate (Sigma Aldrich, 99.9%), Dysprosium(III) chloride hexahydrate (Sigma Aldrich, 99.9%), Holmium(III) chloride hexahydrate (Sigma Aldrich, 99.99%), Erbium(III) nitrate pentahydrate (Sigma Aldrich, 99.9%), Thulium(III) chloride hexahydrate (Sigma Aldrich, 99.9%), Ytterbium(III) trifluoromethanesulfonate hydrate (Sigma Aldrich, 99.99%) and Lutetium(III) chloride hexahydrate (Sigma Aldrich, 99.9%) and Samarium(III) chloride (Alfa Aesar, 99.9%).

Synthesis of CaF_2 Nanosheets: *Caution! HF is highly volatile and toxic in both aqueous and vapor forms. It should be handled only in a well-ventilated space using proper safety precautions.* 0.15 g (1.56 mmol) of $CaSi_2$ was ground under nitrogen atmosphere with mortar/pestle and then added to 30 mL of degassed, deionized water in a tetrafluoroethylene round-bottom flask

immersed in an ice bath. While stirring, 24 drops of HF(aq) were added to the solution. The reaction was stirred for 1 h. The white product then was washed twice with a mixture of deionized H_2O and isopropyl alcohol and isolated by centrifugation. Isolated yield was 0.084 g (68.9 %).

Reactions of CaF_2 Nanosheets with Lanthanide Salts: 0.25 mmol of the CaF_2 nanosheets and 0.2 mmol of lanthanide salt were dispersed in 20 mL of water. The solution was then either stirred at room temperature for 2 h and left to age overnight, or ultrasonicated at 30 amplitude for 30 min and left to age overnight. The product was isolated by centrifugation and dried in a vacuum oven at 50 °C overnight.

Hydrothermal Control Reaction of CaF_2 Nanosheets with $LaCl_3$: 0.02 g (0.25 mmol) of the CaF_2 nanosheets and 0.05 g (0.2 mmol) of $LaCl_3$•$6H_2O$ were dispersed in 20 mL of water. This solution was then sealed in a tetrafluoroethylene-lined autoclave and heated at 180 °C for 24 hours. The product was isolated by centrifugation and dried in a vacuum oven at 50 °C overnight.

Characterization: Product compositions were confirmed using a Bruker D8-Advance powder x-ray diffractometer (Co-Kα radiation source) operated at 40 mA and 40 kV. PXRD patterns were recorded in the 2θ range of 5−80° with a scanning rate of 0.1 sec step−1. The morphology of the CaF_2 nanosheets and lanthanide fluoride nanoproducts were characterized using a FEI Tecnai 20 (200 kV) TEM with SAED capability. Additional characterization on the $LaF_{3-2x}O_x$ nanoscrolls was accomplished using a FEI Nova Nano (30 kV) electron microscope in STEM mode, a Hitachi H9500 (300 kV) high-resolution TEM, an FEI Tecnai F30 TEM (300 kV) and an FEI Talos F200x STEM with energy dispersive x-ray spectroscopy (EDS) mapping. Solid State ^{19}F MAS NMR were collected with a Bruker Avance 600 spectrometer using a Bruker 4mm HFX MAS probe. MAS frequency was actively controlled at ±2 Hz with cooling and spinning air exit temperature maintained at 4°C. ^{19}F (564.671 MHz) spectra were collected using a Hahn-echo pulse sequence

with a 2.5μs excitation pulse, a rotor synchronized 5μs refocusing π-pulse and EXORCYCLE1 phase cycling of the excitation and refocusing pulses to minimize pulse artifacts from RF inhomogeneity. Recycle delays were set to be at least 5*T_1 where ^{19}F T_1 was estimated from the null time ($T_1=\tau_{null}/\ln 2$) with an inversion-recovery sequence. ^{19}F chemical shifts are reference to $CFCl_3$ at 0 ppm. Spectral deconvolution was performed using a SIMPLEX routine integrated into the solids lineshape analysis module (v2.0.1) in the Bruker TopSpin v2.1.6 software with five mixed Lorentzian/Gaussian peaks. XPS data were collected using an X-ray source (Staib Instruments) and a hemispherical analyzer (Leybold Heraeus) under UHV conditions, with the $LaF_{3-2x}O_x$ nanoscrolls dropcast as a thin film on indium foil.

Results and Discussion

Formation of CaF_2 Nanosheets:

The reaction of $CaSi_2$ with HF to produce CaF_2 is known to be strongly exothermic; in fact, $CaSi_2$ has been tested as a candidate for the remediation of HF(g) formed during the detonation of explosives containing fluorinated binders.[58] Here we use this reactivity under aqueous conditions to produce nanostructured CaF_2. The addition of dilute HF(aq) to a stirred suspension of $CaSi_2$ in water leads to a vigorous exothermic reaction that immediately precipitates a white powder. The phase of this product is confirmed to be entirely CaF_2 by powder X-ray diffraction (XRD) (Figure 6.1c). Scherrer analysis of the broad peaks provides an average crystallite size of 16 nm (Table S1).

Transmission electron microscopy (TEM) reveals that the product consists of CaF_2 in three morphologies: square or rectangular nanosheets approximately 20 nm in lateral dimensions

(Figures 1a and S1), irregularly shaped 5-10 nm particles (Figures 1a, S2 and S4), and sparse ~2.5 μm square-shaped platelets (Figure S7). The platelets can be separated by centrifugation, but the nanosheets and nanoparticles remain mixed in the samples subjected to characterization and reactivity studies. High-resolution TEM of individual nanosheets (Figure 6.1b) shows that the lattice fringes are separated by ~0.315 nm, which corresponds to the (111) orientation of CaF_2. Atomic force microscopy (AFM) measurements show that the CaF_2 nanosheets are 0.6 to 1.0 nm thick (Figure S5), which corresponds to one to two unit cells. We can compare these results directly with a recent study of the reaction of $CaSi_2$ with a BF_4^--based ionic liquid, in which by Yaokawa and coworkers observed that the three-dimensional structure of $CaSi_2$ remained intact while the Ca^{2+} layers converted into CaF_2 and the silicide layers transformed into bilayered silicenes.[57] Atomic-resolution TEM revealed that the confined CaF_2 consisted of 0.5-0.9 nm-thick bilayers and trilayers, which is consistent with the freestanding CaF_2 nanosheets isolated here from the reaction of CaF_2 with HF. In related work, flower-like clusters of polycrystalline, ~10 nm thick CaF_2 nanoflakes have been described,[59] but such clusters are difficult to break up into freestanding nanosheets.

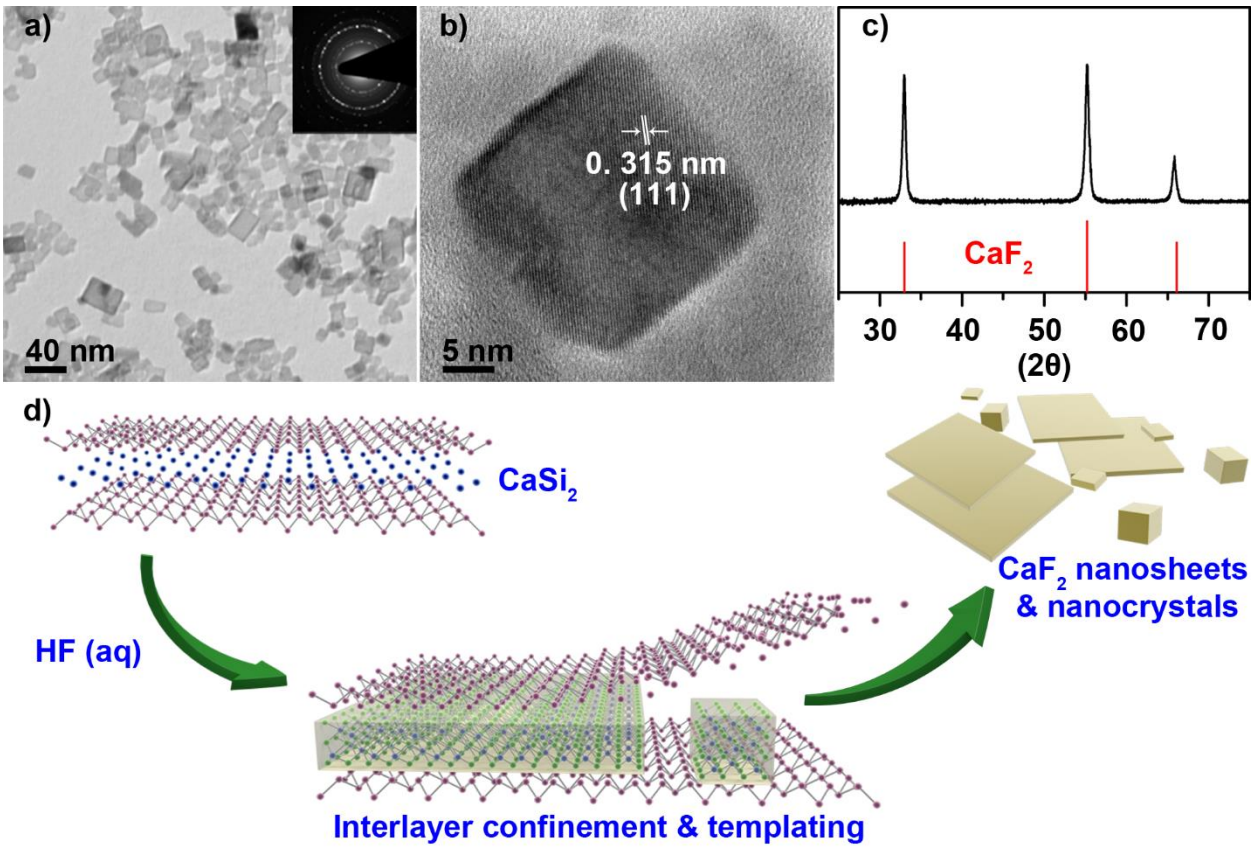

Figure 6.1. CaF_2 nanosheets: a) TEM image shows the rectangular CaF_2 nanosheets and small irregular CaF_2 particles. Inset: SAED arising from the cubic CaF_2 crystal structure. b) High resolution TEM image of a single CaF_2 nanosheet displaying lattice fringes matching the (111) plane. c) Powder XRD pattern for CaF_2 nanosheets with reference pattern for CaF_2 (ICDD no. 01-087-0971). d) Reaction schematic for the formation of CaF_2 nanosheets from $CaSi_2$ through interlayer confinement and templating effects.

Solid-state ^{19}F magic angle spinning (MAS) nuclear magnetic resonance (NMR) spectroscopy is a standard technique used to study disorder and size effects in alkaline earth fluorides.[60-63] As illustrated in Figure 6.2, the ^{19}F MAS NMR spectrum of the CaF_2 nanosheets/nanoparticle sample shows a major broad resonance signal at -108 ppm with spinning

side bands, which arises from the CaF_2 fluoride nuclei that occupy tetrahedral lattice sites surrounded by Ca^{2+}.[63] The small size of our CaF_2 nanosheets is reflected by the ^{19}F NMR spin-lattice relaxation time, T_1 of ~288 ms, which is consistent with literature data on CaF_2 nanocrystallites.[62]

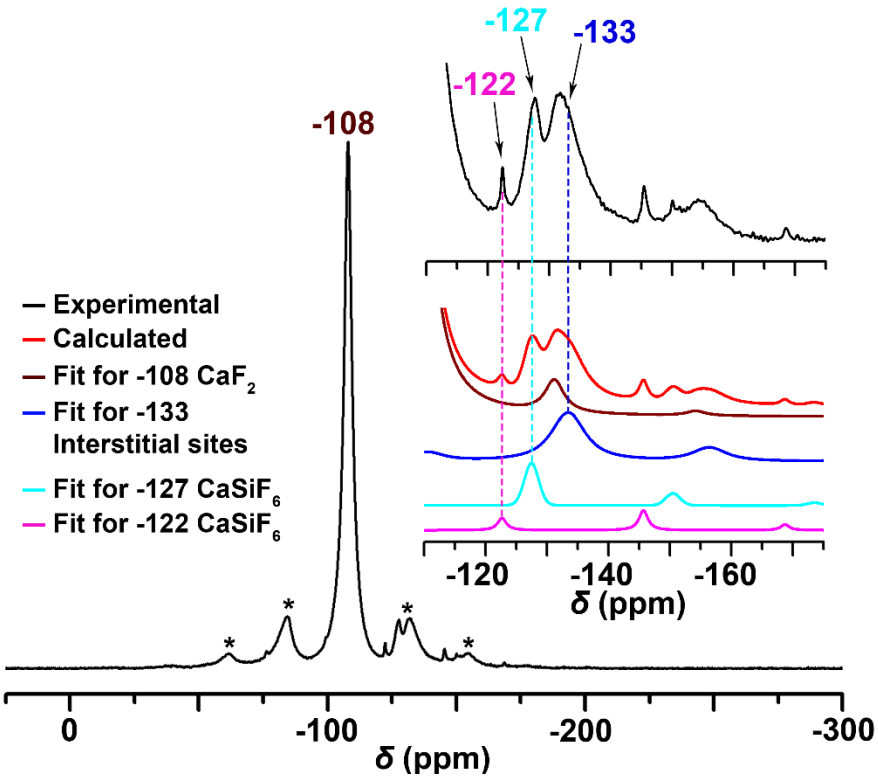

Figure 6.2. ^{19}F MAS NMR spectrum of CaF_2 nanosheets/nanoparticles. The * mark the spinning side bands for the main peak at -108 ppm corresponding to CaF_2. The inset shows a comparison of the experimental data with calculated NMR spectra; the peak at -133 ppm is consistent with Frenkel defect sites in CaF_2, and peaks at -127 and -122 ppm arise from $CaSiF_6$.

In addition to the main CaF_2 peak, a small peak at -133 ppm corresponds to F^- displaced into cuboctahedral interstitial sites (anion Frenkel defects).[61] This particular kind of defect is well known to be more prevalent as crystal size decreases, and it is especially favored on the surfaces of nanocrystallites.[61] Owing to the fast and exothermic nature of the $CaSi_2$ + HF reaction, we

expect at least some of the nanosheets/nanoparticles formed to have defective CaF_2 structures. Additional weak signals at -122 ppm and -127 ppm can be assigned to an amorphous $CaSiF_6$ byproduct.[6, 64] Relative intensities of the ^{19}F resonances show that $CaSiF_6$ accounts for 6.6% of the product mixture (Table S2). The primary fluorine-containing byproduct, water-soluble fluorosilicic acid (H_2SiF_6), was confirmed by solution ^{19}F NMR measurements on the reaction supernatant (Figure S3). Thus, we can account for all species involved in the primary reaction (Eq. 1) as well as a side reaction (Eq. 2):

(Eq. 1) $$CaSi_2(s) + 14\ HF(aq) \rightarrow CaF_2(s) + 2\ H_2SiF_6(aq) + 5\ H_2(g)$$

(Eq. 2) $$H_2SiF_6(aq) + Ca^{2+}(aq) \rightarrow CaSiF_6(s) + 2\ H^+(aq)$$

In the reactions of $CaSi_2$ with HCl(aq) *versus* HF(aq), the differences in the solubilities of the calcium halides formed, as well as the high reactivity of silicon with HF, contribute to the very different products that result. In the case of HF(aq), the fast formation of CaF_2 in the limited interlayer spaces [~0.5 nm between $(Si^-)_n$ sheets] accounts for the resulting nanosheet morphology. Additionally, we posit that CaF_2 formation is templated between the silicon layers of the $CaSi_2$ as the fluoride ions first react with the interlayer calcium ions, as seen in the reaction of $CaSi_2$ with BF_4^-.[57] After CaF_2 formation is complete, there are no dangling bonds attaching CaF_2 to the silicide layers, and the CaF_2 nanosheets are easily released as the silicide is consumed according to Eq. 1. Thus, as illustrated in Figure 6.1d, both confinement and templating direct the two-dimensional growth of CaF_2 in this system. Similar effects have been noted in examples of nanoparticle formation within the layers of a host material,[65-68] and in a handful of cases, two-dimensional nanomorphologies have been obtained, e.g., the formation of graphene between the layers of a MgAl-layered double hydroxide.[69]

Based on the formation of CaF_2 nanosheets in this work together with the results published by Yaokawa and coworkers,[57] we also can conclude that the reaction of $CaSi_2$ with fluoride sources is not a viable route to fluorinated silicene $(Si_6F_6)_n$, which has potential electronics applications and is predicted to be stable in freestanding nanosheet form.[44-45, 70-72]

Reactions of CaF_2 Nanosheets with Lanthanide Ions:

Next we studied the reactivity of CaF_2 nanosheets with Ln^{3+} (Ln = La–Lu) by stirring the nanosheets in aqueous solutions of Ln^{3+} salts at room temperature.[73] In all cases the products were fully nanostructured, and the complete range of morphologies and compositions were analyzed by TEM (Figure 6.3) and PXRD (Figure 6.4). These results are summarized in Table 1. Unexpectedly, none of the reactions yielded Ln^{3+}-doped CaF_2, the typical product that forms when nano-CaF_2 is exposed to Ln^{3+}.[4, 73] The most interesting case is the reaction with La^{3+}, which produces nanoscrolls and clusters of nanoparticles (Figures 3a and S8). We will return to this exceptional product in the next section of this report.

Table 6.1. Summary of product compositions and morphologies for reactions of CaF_2 nanosheets with Ln^{3+} sources. Products include hexagonal LnF_3 (*h*-LnF_3), orthorhombic LnF_3 (*o*-LnF_3), and cubic CaF_2 (*c*-CaF_2).

Ln^{3+} Source	**Product Composition**				**Product Morphology**
	***h*-LnF_3**	***o*-LnF_3**	***c*-CaF_2**	**Other**	
$LaCl_3$, $LaBr_3$, $La(OTf)_3$	--	--	--	Hexagonal $LaF_{3-2x}O_x$	20 nm in length nanoscrolls + 5-10 nm diameter nanoparticles
$CeCl_3 \cdot 7H_2O$	✓	--	✓	--	200-500 nm diameter disks of CeF_3 + unreacted CaF_2 nanosheets
$Pr(OTf)_3$	✓	--	--	--	20 nm oblong platelets of PrF_3
$Nd(NO_3)_3 \cdot 6H_2O$	✓	--	--	--	40 nm diameter clusters of nanoparticles of NdF_3
$SmCl_3$	✓	--	--	--	100-200 nm diameter disks of SmF_3
$EuCl_3 \cdot 6H_2O$	✓	--	✓	--	20 nm diameter square sheets of EuF_3 and unreacted 20 nm diameter square sheets of CaF_2
$Gd(NO_3)_3 \cdot 6H_2O$	--	✓	--	--	20 nm diameter square sheets of GdF_3 and 20 nm diameter square sheets of CaF_2
$TbCl_3 \cdot 6H_2O$	--	--	✓	--	20 nm diameter square sheets and oblong platelets of CaF_2
$DyCl_3 \cdot 6H_2O$	--	✓	--	--	200 nm in length aggregates of nanoparticles of DyF_3
$HoCl_3 \cdot 6H_2O$	--	✓	--	--	40 nm diameter square sheets and oblong platelets of HoF_3
$Er(NO_3)_3 \cdot 5H_2O$	--	✓	--	--	40 nm diameter square sheets and oblong platelets of ErF_3
$TmCl_3 \cdot 6H_2O$	--	--	✓	--	20 nm diameter square sheets of CaF_2
$Yb(OTf)_3$	--	✓	--	cubic $YbF_{2.37}$	20 nm diameter square sheets and nanoparticles of $YbF_{2.37}$ and YbF_3
$LuCl_3 \cdot 6H_2O$	--	--	✓	--	20 nm diameter square sheets of CaF_2

The reactions of CaF_2 nanosheets with Ln^{3+} ions Ce^{3+} through Eu^{3+} consistently produced hexagonal LnF_3 products. For example, cerium and samarium chlorides lead to the formation of uniform 200-500 nm diameter disks (Figures 3b, 3e) of the respective hexagonal trifluorides CeF_3 and SmF_3 (Figures 4b, 4e). Judging by the rather large lateral dimensions of these products, these reactions likely proceed through a dissolution-renucleation mechanism. Using $Pr(OTf)_3$ leads to oblong platelets (Figure 6.3c) of hexagonal PrF_3 (Figure 6.4c), whereas the reaction with $Nd(NO_3)_3$ produces nanoparticle clusters (Figure 6.3d) of hexagonal NdF_3 (Figure 6.4d). Reacting CaF_2 nanosheets with $EuCl_3$ leads to the formation of hexagonal EuF_3 nanosheets that appear similar in morphology to the starting material, which suggests a mechanism of direct templating of EuF_3 from CaF_2. In some of these reactions, PXRD also indicates the presence of unreacted cubic CaF_2 (Figures 4b, 4f) and/or elemental silicon (Figures 4a, 4b, 4d).

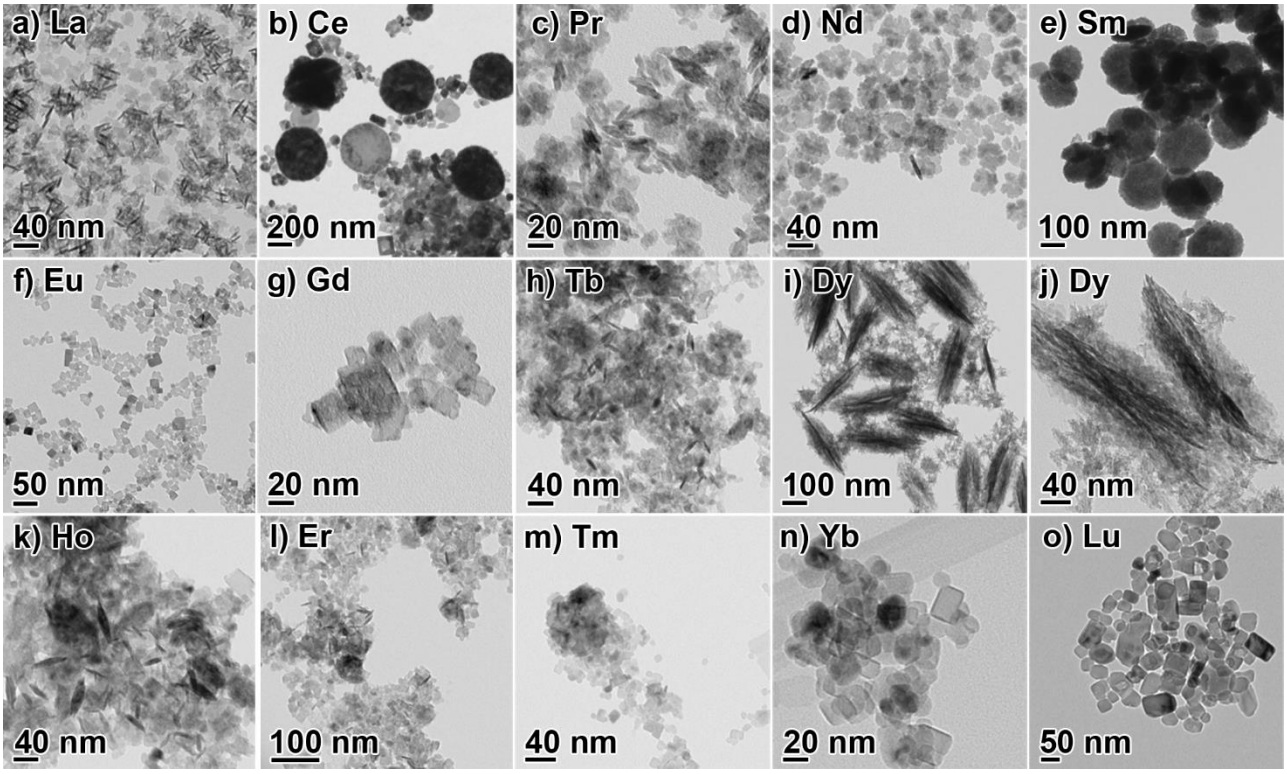

Figure 6.3. TEM images showing the nanoproducts obtained from reacting CaF_2 nanosheets with lanthanide salts.

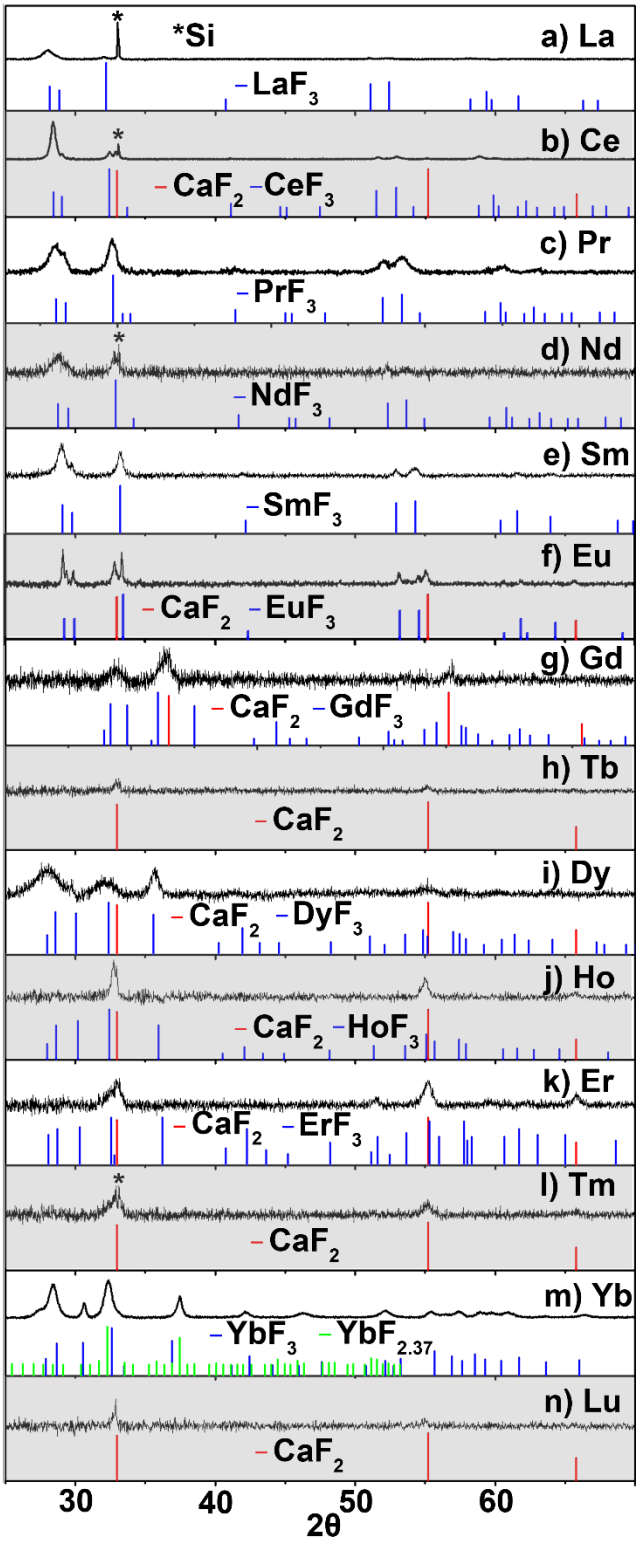

Figure 6.4. PXRD patterns for the nanoproducts produced by the reaction of CaF_2 nanosheets with lanthanide salts: a) hexagonal LaF_3 with matching ICDD no. 04-005-4471 reference pattern[74], b)

mixture of hexagonal CeF_3 ICDD no. 04-008-8281 reference pattern[75] and cubic CaF_2 with ICDD no. 00-004-0864 reference pattern[76], c) hexagonal PrF_3 with ICDD no. 04-005-5143 reference pattern[77], d) hexagonal NdF_3 with ICDD no. 04-006-8285 reference pattern[78], e) hexagonal SmF_3 with ICDD no. 00-012-0792 reference pattern[79], f) mixture of hexagonal EuF_3 with ICDD no. 00-032-0373 reference pattern[80] and cubic CaF_2 with ICDD no. 00-004-0864 reference pattern[76], g) mixture of orthorhombic GdF_3 with ICDD no. 04-006-9968 reference pattern[81] and cubic CaF_2 with ICDD no. 00-004-0864 reference pattern[76], h) cubic CaF_2 with ICDD no. 00-004-0864 reference pattern[76], i) mixture of orthorhombic DyF_3 with ICDD no. 04-007-3260 reference[82] and cubic CaF_2 with ICDD no. 00-004-0864 reference pattern[76], j) mixture of orthorhombic HoF_3 with ICDD no 00-023-0284 pattern[83] and cubic CaF_2 with ICDD no. 00-004-0864 reference pattern[76] k), Mixture of orthorhombic ErF_3 with ICDD no. 00-032-0361 reference[80] and cubic CaF_2 with ICDD no. 00-004-0864 reference pattern[76] l), cubic CaF_2 with ICDD no. 00-004-0864 reference pattern[76] m), mixture of orthorhombic YbF_3 with ICDD no. 00-032-0102 reference[84] and cubic $YbF_{2.37}$ with ICDD no. 00-034-0824 reference pattern[85], and n) cubic CaF_2 with ICDD no. 00-004-0864 reference pattern[76]. *Silicon impurity is seen in some samples; reference ICDD no. 04-016-4861[86].

Extensive prior studies have established that lanthanides fluorides where Ln = La-Sm/Eu preferentially adopt a hexagonal tysonite-type crystal structure whereas compositions where Ln = Gd-Yb/Lu, LnF_3 adopt an orthorhombic *Pnma* structure.[10,87] The switch from hexagonal to orthorhombic LnF_3 has been attributed to decreasing ionic radii along with changes in coordination number.[16, 88-89] We observe the same phenomenon in the reactions of CaF_2 nanosheets with Ln^{3+} salts where Ln = La-Eu yields hexagonal fluoride products but Ln = Gd-Yb yields orthothombic

LnF_3. The reaction with $Gd(NO_3)_3$ forms a product that looks very similar to the initial CaF_2 nanosheets (Figure 6.3g), yet the product composition indicates a mixture of orthorhombic GdF_3 and unreacted CaF_2 (Figure 6.4g); as in the case of CaF_2 nanosheets --> EuF_3 nanosheets, it is probable that this reaction occurs by topochemical templating. Reaction with $DyCl_3$ produces cylindrical morphologies (Figure 6.3i); however, upon closer inspection these structures appear to be aggregates of nanoparticles (Figure 6.3j), and XRD shows that the product is orthorhombic DyF_3 (Figure 6.4i). Reaction with holmium and erbium salts produces orthorhombic HoF_3 and ErF_3, respectively, and unreacted cubic CaF_2 nanosheets also are present in the product mixture (Figure 6.4j, 4k). These nanoproducts are composed up of ~40 nm square nanosheets and some oblong platelets (Figure 6.3k, 3l). Using $Yb(OTf)_3$ also yields square nanosheets and nanoparticles (Figure 6.3n), but in this case the product is a mixture of orthorhombic YbF_3 and cubic $YbF_{2.37}$ phases (Figure 6.4m).

In contrast to the other lanthanides, exposing CaF_2 nanosheets to salts of Tb, Tm and Lu appears to have little effect (Figures 4h, 4l, 4n). Although it is possible that a low level of Ln^{3+} doping is incorporated into the CaF_2 lattice, the XRD patterns of the recovered material matched closely with the starting CaF_2 nanosheets, and thus we did not pursue alternative confirmation of doping.

Formation of $LaF_{3-2x}O_x$ Nanoscrolls:

The formation of a scrolled product in the reaction of CaF_2 nanosheets with La^{3+} salts is surprising. According to significant precedent, the product of this reaction should be hexagonal LaF_3.[16, 88-89] As demonstrated by the cerium through europium examples above and also by a prior example of ~2 nm thick LaF_3 nanotriangles,[15] there is no driving force for scrolling in hexagonal LnF_3 systems. We now describe how the reaction of CaF_2 nanosheets with La^{3+} produces partially hydrolyzed lanthanum fluoride in a topochemical fashion that leads to lattice strain-induced scrolling. As illustrated in Figure 6.5, the nanoscrolls are approximately 20 nm in length and 5 nm in diameter (Figure 6.5a and Figures S9 and S10 in supporting information). High-resolution TEM of an individual nanoscroll highlights the rolled up edges with corresponding lattice fringing (Figure 6.5b). The d-spacing on the tapered portion of the scroll matches (101) LaF_3, whereas the d-spacings on the body of the scroll vary, indicating that the lattice is perturbed in some way. High resolution scanning transmission electron microscopy (STEM) with energy dispersive x-ray spectroscopy (EDS) elemental mapping (Figure 6.5d, 6.5e) shows the presence of La and F co-located in the nanoscrolls. However, quantitative EDS measurements (Table S3) indicate a non-stoichiometric, fluorine deficient, lanthanum fluoride composition with an overall chemical formula of $LaF_{1.96}O_{0.76}$. The amount of Ca present in the scrolls is negligible, indicating complete cationic exchange.

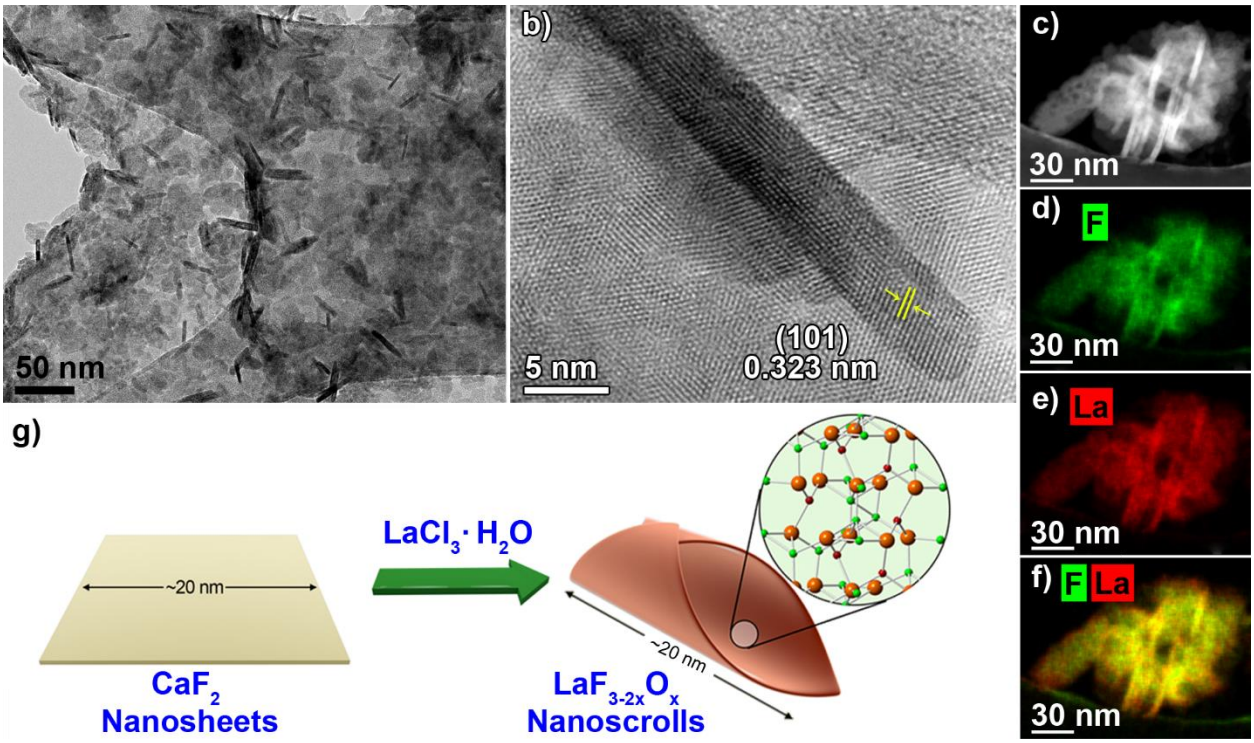

Figure 6.5. Characterization of $LaF_{3-2x}O_x$ nanoscrolls: a) TEM image of the $LaF_{3-2x}O_x$ nanoscrolls, b) High resolution TEM image of a single nanoscroll showing the lattice fringing with a d-spacing of 3.23 Å that matches the (101) plane of the LaF_3 structure, c) STEM image illustrates both the particle and scroll morphologies, d-f) STEM elemental mapping shows the presence of La and F in the scrolls and particles, and g) schematic of the overall scrolling process.

To check whether the lanthanum or the chloride ions were responsible for the scrolling behavior, we reacted the CaF_2 nanosheets with alternate La^{3+} sources, including $La(OTf)_3$ (Figure S11) and $LaBr_3$ (Figure S12); both of these La^{3+} sources produced the same scrolling effect as $LaCl_3$. Using an excess of lanthanum salt does not change the nanoscroll morphology of the product, however, doing the reaction with sub-stoichiometric amounts of lanthanum salt leads to partial substitution and partial scrolling (Figure S13). Due to the observance of partially rolled nanosheets, as well as the non-uniform contrast under TEM and the edges of the nanoscroll

showing only a single sheet layer (Figure S14), we confirm that these nanostructures are indeed nanoscrolls and not nanorods. Although we conducted all the reactions of CaF_2 nanosheets with Ln^{3+} salts summarized in Table 1 at room temperature, in the case of La^{3+} we also conducted the reaction at hydrothermal conditions. In contrast to the nanoscrolls formed at room temperature, at 180 °C the reaction yielded 30-70 nm hexagonal-shaped LaF_3 nanocrystals (Figure S15). This result, suggesting dissolution-renucleation under these more intense conditions, is similar to previously-reported hydrothermal syntheses of nanostructured lanthanide fluorides.[20, 88-89]

The data, especially the EDS results, can be best explained by a partially oxidized LaF_3 nanoproduct $LaF_{3-2x}O_x$. As documented in the literature, the hydrolysis of bulk LnF_3 is known to proceed through several stages: LnF_3 --> $LnF_{3-2x}O_x$ --> LnOF --> Ln_2O_3.[8, 10-11, 90] LaF_3, in particular, is among the most difficult lanthanide fluorides to hydrolyze, and several documented examples stop at the $LaF_{3-2x}O_x$ oxyfluoride.[8, 10-11, 91-93] However, among all lanthanide fluoride cases, direct hydrolysis occurs only at high temperatures of 400-1000 °C (pyrohydrolysis). On the other hand, there are several reports of nanostructured cubic LaOF formation under hydrothermal conditions,[20,93-94] and these products transform into LaF_3 upon further heating.[95]

The hexagonal (trigonal) tysonite-type LaF_3 structure consists of highly-coordinated La^{3+} surrounded by eleven F^- ions, nine at the corners and two above and below.[96] In the $LaF_{3-2x}O_x$ structure, two F^- are replaced by a single O^{2-} while maintaining the overall hexagonal LnF_3 structure.[8] Typically such F^- replacements are accompanied by anionic vacancies that stabilize the crystal by lowering anionic repulsions, resulting in fluorine-deficient stoichiometries.[8,92] Although atomic coordinates for the $LaF_{3-2x}O_x$ structure are not available, a detailed study on the incorporation of oxygen into LaF_3 thin films demonstrates that an O/F ratio as high as 0.35 is possible.[92]

X-ray photoelectron spectroscopy (XPS) data on the nanoscrolls further substantiates the interpretation of $LaF_{3-2x}O_x$ formation. Figure 6.6a shows two O 1s peaks at 531.97 eV and 532.82 eV for La-O binding sites and surface oxygen, respectively,[97] as well as a shoulder at 862.97 eV on the La $3d_{5/2}$ peak (Figure 6.6b) that indicates the presence of La-O species due to oxidation.[92, 97] The F 2p spectrum reveals the typical LaF_3 peak in addition to a small peak at 706.28 eV, which we assign to the O-F environment (Figure 6.6c). A Si peak (Figure 6.6d) most likely is due to elemental silicon originally present as an impurity in the commercial $CaSi_2$ starting material and carried through the synthetic steps.

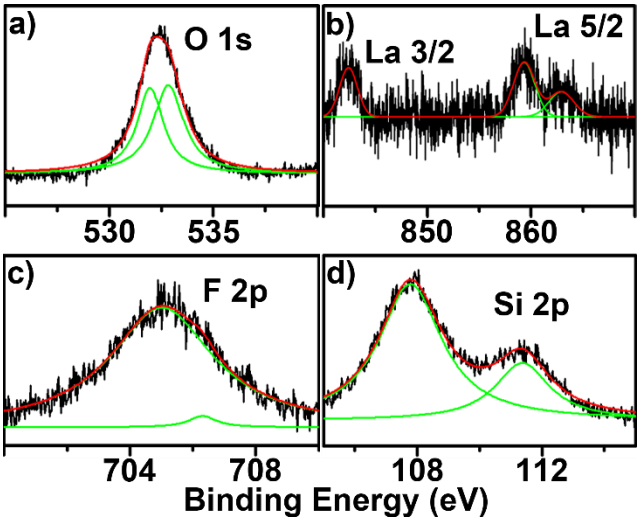

Figure 6.6. XPS measurements on the $LaF_{3-2x}O_x$ nanoscrolls with peak fitting of a) O 1s, b) La 3d, c) F 2p, and d) Si 2p.

Solid-state ^{19}F MAS NMR spectroscopy on the $LaF_{3-2x}O_x$ nanoscroll powder (Figure 6.7) shows peaks arising from the $LaF_{3-2x}O_x$, from CaF_2 platelets that do not convert to LaF_3 due to their larger size and thickness, and from several expected byproducts. The $LaF_{3-2x}O_x$ nanoscrolls contribute the broad resonances at -23, 20 and 28 ppm with spinning side bands at the same

chemical shift as typically seen for LaF_3.[62] The CaF_2 platelets display the expected central peak at -108 ppm, in addition to a sharp peak at -85 ppm due to CaClF derived from halide exchange of CaF_2 platelets with Cl^- originating from $LaCl_3$.[6] Additionally, we see peaks corresponding to $CaSiF_6$ and interstitial CaF_2 sites that already were present in the CaF_2 nanosheets (Figure 6.2).

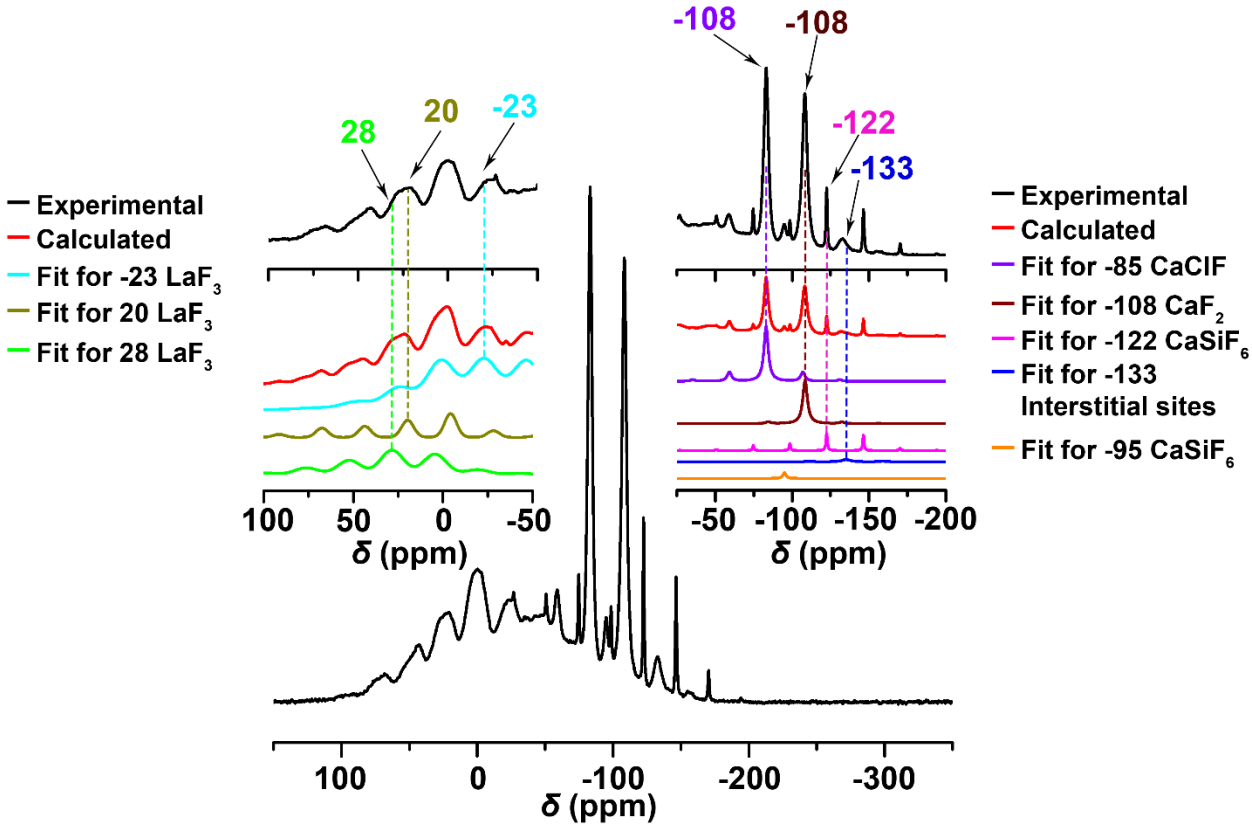

Figure 6.7. ^{19}F MAS NMR spectrum of $LaF_{3-2x}O_x$ nanoscrolls. The left inset shows a comparison of the experimental and calculated NMR spectra for the three LaF_3 peaks at 28, 20, and -23. The right inset shows a comparison of the experimental and calculated NMR spectra for CaClF and CaF_2 and the peaks at -133 ppm which is indicative of Frenkel defect sites as well as at -127 and -122 ppm for the $CaSiF_6$ species.

The overall chemical transformation from CaF_2 nanosheets most likely proceeds by Eq. 3 to a hydroxyl intermediate and then finally to the $LaF_{3-2x}O_x$ nanoscroll product:

(Eq. 3) $3\ CaF_2(s) + 2\ LaCl_3(aq) + x\ H_2O \rightarrow 2\ LaF_{3-x}(OH)_x(s) + 3\ CaCl_2(aq) + x\ H^+(aq)$

There are four unique aspects to this chemistry. The first is the unexpected conversion of CaF_2 into $LaF_{3-2x}O_x$. As already discussed, the reaction of CaF_2 + $LaCl_3$ usually leads to CaF_2:La^{3+} doping when La^{3+} inserts into Ca^{2+} sites. However, because CaF_2 nanosheets have a high surface area and 1-2 layer thickness, there is a complete exchange of cations rather than doping. A second interesting aspect is the ease of Eq. 3, with the reaction conducted in one pot at ambient conditions. As often the case, the small size and large surface area of the nanostructured precursor leads to greatly enhanced reactivity compared to bulk counterparts. In addition, the CaF_2 nanosheets used here are essentially "bare", i.e. no capping ligands are present, which contributes to their reactivity. The third unique aspect is the remarkable topochemical nature of the $CaF_2 \rightarrow LaF_{3-2x}O_x$ transformation that preserves the nanosheet-nanoscroll morphologies. Although there is precedence for topochemical reactions that preserve two-dimensional morphologies,[98-99] we are not aware of any examples involving metal fluorides. Certainly the lattice vacancies in this system also must play an important role in stabilizing the hexagonal LaF_3 structure, which in turn helps to maintain the nanosheet-nanoscroll morphologies.[10-11]

The final notable aspect of the nanochemistry reported here is the scrolling mechanism itself. Typically, nanoscrolls are formed as products of intercalation-exfoliation reactions, and the scrolling itself is caused by either surface interactions that decrease the system energy in monolayer nanosheets (e.g., favorable van der Waals interactions) or by structural stresses due to strained bonds, ion binding, vacancies, or nanosheet asymmetry.[22-23,26] Taking into consideration the larger ionic radius of La^{3+} compared to Ca^{2+}, the partially oxidized structure, and the presence

of fluoride vacancies, we propose that the nanosheets scroll as a result of lattice strain accompanying the formation of $LaF_{3-2x}O_x$ directly from CaF_2. Such spontaneous rolling coupled with novel topochemistry provides a new mechanism for how to trigger scrolling in two-dimensional materials. The closest comparison in the literature is the instance of oleic acid-capped LaF_3 triangular nanoplates;[15] these "nanosheets" do not scroll despite their ~2 nm thickness, however.

Conclusions

In summary, we have demonstrated novel routes that provide access to CaF_2 nanosheets and $LaF_{3-2x}O_x$ nanoscrolls. These are rare examples of the two-dimensional structuring of non-layered materials, which is synthetically challenging because of the inherent difficulty in differentiating planes that define two-dimensional morphologies. In particular, there exists only a small subset of nanoscroll materials based on non-layered lattices: *fcc* Ni nanoscrolls,[100] cubic $Y_2O_3:Eu^{3+}$ nanoscrolls,[101] and scrolled close-packed membranes of Au nanoparticles.[102] Conceptually related examples are provided by nanotubes of several cubic materials, including CdSe,[41] MgO,[103] and Si.[104] The addition of $LaF_{3-2x}O_x$ nanoscrolls to this group confirms that there are still many nanoscroll structures to be discovered, and it opens valuable pathways in nanosheet and nanoscroll research based on the most challenging material systems.

References

1. Cao, M.; Hu, C.; Wang, E., The First Fluoride One-dimensional Nanostructures: Microemulsion-mediated Hydrothermal Synthesis of BaF_2 Whiskers. *J. Am. Chem. Soc.* **2003,** *125*, 11196–11197.

2. Rüdiger, S.; Groß, U.; Kemnitz, E., Non-aqueous Sol-gel Synthesis of Nano-structured Metal Fluorides. *J. Fluorine Chem.* **2007,** *128*, 353–368.

3. Hua, R.; Zang, C.; Shao, C.; Xie, D.; Shi, C., Synthesis of Barium Fluoride Nanoparticles from Microemulsion. *Nanotechnology* **2003,** *14*, 588–591.

4. Mao, Y. Zhang, F., Wong, S. S. Ambient Template-Directed Synthesis of Single-Crystalline Alkaline-Earth Metal Fluoride Nanowires. *Adv. Mater.* **2006**, *18*, 1895–1899.

5. Dong, N. N.; Pedroni, M.; Piccinelli, F.; Conti, G.; Sbarbati, A.; Ramirez-Hernandez, J. E.; Maestro, L. M.; Iglesias-de la Cruz, M. C.; Sanz-Rodriguez, F.; Juarranz, A.; Chen, F.; Vetrone, F.; Capobianco, J. A.; Sole, J. G.; Bettinelli, M.; Jaque, D.; Speghini, A., NIR-to-NIR Two-photon Excited CaF_2: Tm^{3+},Yb^{3+} Nanoparticles: Multifunctional Nanoprobes for Highly Penetrating Fluorescence Bio-imaging. *ACS Nano* **2011,** *5*, 8665–8671.

6. Rehmer, A.; Scheurell, K.; Kemnitz, E., Formation of Nanoscopic CaF_2 via a Fluorolytic Sol-gel Process for Antireflective Coatings. *J. Mater. Chem. C* **2015,** *3*, 1716–1723.

7. Li, C.; Lin, J., Rare Earth Fluoride Nano-/Microcrystals: Synthesis, Surface Modification and Application. *J. Mater. Chem.* **2010,** *20*, 6831–6847.

8. Sobolev, B.; Fedorov, P.; Seiranian, K.; Tkachenko, N., On the Problem of Polymorphism and Fusion of Lanthanide Trifluorides. II. Interaction of LnF_3 with MF_2 (M= Ca, Sr, Ba), Change

in Structural Type in the LnF_3 Series, and Thermal Characteristics. *J. Solid State Chem.* **1976,** *17*, 201–212.

9. Fedorov, P., Association of Point Defects in Non Stoichiometric $M_{1-x}R_xF_{2+x}$ Fluorite-type Solid Solutions. *Butll. Soc. Cat. Cièn* **1991,** *12*, 349–381.

10. Sobolev, B. *The High Temperature Chemistry of the Rare Earth Trifluorides*; Institut d'Estudis Catalans: Barcelona, 2000.

11. Sobolev, B.; Alekseeva, I.; Khitarov, D. *Introduction to Materials Science of Multicomponent Metal Fluoride Crystals*; Institut d'Estudis Catalans: Barcelona, 2001.

12. Dieudonné, B.; Chable, J.; Mauvy, F.; Fourcade, S.; Durand, E.; Lebraud, E.; Leblanc, M.; Legein, C.; Body, M.; Maisonneuve, V., Exploring the $Sm_{1-x}Ca_xF_{3-x}$ Tysonite Solid Solution as a Solid-state Electrolyte: Relationships Between Structural Features and F–ionic Conductivity. *J. Phys. Chem. C* **2015,** *119*, 25170–25179.

13. Lucca, A.; Debourg, G.; Jacquemet, M.; Druon, F.; Balembois, F.; Georges, P.; Camy, P.; Doualan, J.L.; Moncorgé, R., High-power Diode-pumped Yb^{3+}: CaF_2 Femtosecond Laser. *Opt. Lett.* **2004,** *29*, 2767–2769.

14. Lemyre, J.-L.; Ritcey, A. M., Synthesis of Lanthanide Fluoride Nanoparticles of Varying Shape and Size. *Chem. Mater.* **2005,** *17*, 3040–3043.

15. Zhang, Y.-W.; Sun, X.; Si, R.; You, L.-P.; Yan, C.-H., Single-crystalline and Monodisperse LaF_3 Triangular Nanoplates from a Single-source Precursor. *J. Am. Chem. Soc.* **2005,** *127*, 3260–3261.

16. Li, C.; Yang, J.; Yang, P.; Lian, H.; Lin, J., Hydrothermal Synthesis of Lanthanide Fluorides LnF_3 (Ln= La to Lu) Nano-/Microcrystals with Multiform Structures and Morphologies. *Chem. Mater.* **2008,** *20*, 4317–4326.

17. Wang, G. F.; Peng, Q.; Li, Y. D., Upconversion Luminescence of Monodisperse CaF_2:Yb^{3+}/Er^{3+} Nanocrystals. *J. Am. Chem. Soc.* **2009,** *131*, 14200–14201.

18. Chen, G. Y.; Shen, J.; Ohulchanskyy, T. Y.; Patel, N. J.; Kutikov, A.; Li, Z. P.; Song, J.; Pandey, R. K.; Agren, H.; Prasad, P. N.; Han, G., (α-$NaYbF_4$:Tm^{3+})/CaF_2 Core/Shell Nanoparticles with Efficient Near-infrared to Near-infrared Upconversion for High-contrast Deep Tissue Bioimaging. *ACS Nano* **2012,** *6*, 8280–8287.

19. Bartůněk, V.; Jakeš, V.; Král, V.; Rak, J., Lanthanum Trifluoride Nanoparticles Prepared using Ionic Liquids. *J. Fluorine Chem.* **2012,** *135*, 358–361.

20. Fedorov, P. P.; Luginina, A. A.; Kuznetsov, S. V.; Osiko, V. V. Nanofluorides. *J. Fluorine Chem.* **2011,** *132*, 1012–1039.

21. Rahman, P.; Green, M., The Synthesis of Rare Earth Fluoride Based Nanoparticles. *Nanoscale* **2009,** *1*, 214–224.

22. Ma, R.; Sasaki, T. Conversion of Metal Oxide Nanosheets into Nanotubes. In *Inorganic and metallic nanotubular materials: recent technologies and applications*; Kijima, T Ed.; Springer Science & Business Media, 2010; pp. 135–146.

23. Perim, E.; Machado, L. D.; Galvao, D. S., A Brief Review on Syntheses, Structures and Applications of Nanoscrolls. *Front. Mater.* **2014**. *1*, 1–7.

24. Wang, X.; Chen, Y.; Schmidt, O. G.; Yan, C., Engineered Nanomembranes for Smart Energy Storage Devices. *Chem. Soc. Rev.* **2016**, *45*, 1308–1330.

25. Viculis, L. M.; Mack, J. J.; Kaner, R. B., A Chemical Route to Carbon Nanoscrolls. *Science* **2003,** *299*, 1361–1361.

26. Wallace, J., Shao, L. Defect-Induced Carbon Nanoscroll Formation. *Carbon* **2015**, *91*, 96-102.

27. Yao, K.; Manjare, M.; Barrett, C. A.; Yang, B.; Salguero, T. T.; Zhao, Y., Nanostructured Scrolls from Graphene Oxide for Microjet Engines. *J. Phys. Chem. Lett.* **2012,** *3*, 2204–2208.

28. Xu, Z.; Zheng, B.; Chen, J.; Gao, C., Highly Efficient Synthesis of Neat Graphene Nanoscrolls from Graphene Oxide by Well-controlled Lyophilization. *Chem. Mater.* **2014,** *26*, 6811–6818.

29. Brand, C.; Sclafani, M.; Knobloch, C.; Lilach, Y.; Juffmann, T.; Kotakoski, J.; Mangler, C.; Winter, A.; Turchanin, A.; Meyer, J.; Cheshnovsky, O.; Arndt, M., An Atomically Thin Matter-wave Beamsplitter. *Nat. Nanotechnol.* **2015,** *10*, 845–848.

30. Amadei, C. A.; Stein, I. Y.; Silverberg, G. J.; Wardle, B. L.; Vecitis, C. D., Fabrication and Morphology Tuning of Graphene Oxide Nanoscrolls. *Nanoscale* **2016,** *8*, 6783–6791.

31. Zheng, B.; Xu, Z.; Gao, C., Mass Production of Graphene Nanoscrolls and Their Application in High Rate Performance Supercapacitors. *Nanoscale* **2016,** *8*, 1413–1420.

32. Abe, R.; Shinohara, K.; Tanaka, A.; Hara, M.; Kondo, J. N.; Domen, K., Preparation of Porous Niobium Oxide by the Exfoliation of $K_4Nb_6O_{17}$ and its Photocatalytic Activity. *J. Mater. Res.* **1998,** *13*, 861–865.

33. Saupe, G. B.; Waraksa, C. C.; Kim, H.-N.; Han, Y. J.; Kaschak, D. M.; Skinner, D. M.; Mallouk, T. E., Nanoscale Tubules Formed by Exfoliation of Potassium Hexaniobate. *Chem. Mater.* **2000,** *12*, 1556–1562.

34. Muhr, H. J.; Krumeich, F.; Schonholzer, U. P.; Bieri, F.; Niederberger, M.; Gauckler, L. J.; Nesper, R., Vanadium Oxide Nanotubes–A New Flexible Vanadate Nanophase. *Adv. Mater.* **2000,** *12*, 231–234.

35. Shi, L.; Xu, Y.; Li, Q., Controlled Growth of Lead Oxide Nanosheets, Scrolled Nanotubes, and Nanorods. *Cryst. Growth Des.* **2008,** *8*, 3521–3525.

36. Rostamzadeh, T.; Adireddy, S.; Wiley, J. B., Formation of Scrolled Silver Vanadate Nanopeapods by Both Capture and Insertion Strategies. *Chem. Mater.* **2015,** *27*, 3694–3699.

37. Ren, L.; Hu, J.-S.; Wan, L.-J.; Bai, C.-L., A Simple Method to Synthesize Layered Double Hydroxide Nanoscrolls. *Mater. Res. Bull.* **2007,** *42*, 571–575.

38. Kuroda, Y.; Ito, K.; Itabashi, K.; Kuroda, K., One-Step Exfoliation of Kaolinites and Their Transformation into Nanoscrolls. *Langmuir* **2011,** *27*, 2028–2035.

39. Li, X.; Liu, Q.; Cheng, H.; Zhang, S.; Frost, R. L., Mechanism of Kaolinite Sheets Curling via the Intercalation and Delamination Process. *J. Colloid Interface Sci.* **2015,** *444*, 74–80.

40. White, R. D.; Bavykin, D. V.; Walsh, F. C., Spontaneous Scrolling of Kaolinite Nanosheets into Halloysite Nanotubes in an Aqueous Suspension in the Presence of GeO_2. *J. Phys. Chem. C* **2012,** *116*, 8824–8833.

41. Shen, Q.; Jiang, L.; Miao, J.; Hou, W.; Zhu, J.-J., Sonoelectrochemical Synthesis of CdSe Nanotubes. *Chem. Commun.* **2008,** *14*, 1683–1685.

42. Radovsky, G.; Popovitz-Biro, R.; Stroppa, D. G.; Houben, L.; Tenne, R., Nanotubes from Chalcogenide Misfit Compounds: Sn–S and Nb–Pb–S. *Acc. Chem. Res.* **2014,** *47*, 406–416.

43. Thangasamy, P.; Sathish, M., Rapid, One-pot Synthesis of Luminescent MoS_2 Nanoscrolls using Supercritical Fluid Processing. *J. Mater. Chem. C* **2016,** *4*, 1165–1169.

44. Ma, R.; Kobayashi, Y.; Youngblood, W. J.; Mallouk, T. E., Potassium Niobate Nanoscrolls Incorporating Rhodium Hydroxide Nanoparticles for Photocatalytic Hydrogen Evolution. *J. Mater. Chem.* **2008,** *18*, 5982–5985.

45. Rani, J. R.; Oh, S.-I.; Woo, J. M.; Tarwal, N. L.; Kim, H.-W.; Mun, B. S.; Lee, S.; Kim, K.-J.; Jang, J.-H., Graphene Oxide–Phosphor Hybrid Nanoscrolls with High Luminescent Quantum Yield: Synthesis, Structural, and X-ray Absorption Studies. *ACS Appl. Mater. Interfaces* **2015,** *7*, 5693–5700.

46. Singh, V. V.; Wang, J., Nano/Micromotors for Security/Defense Applications. A Review. *Nanoscale* **2015,** *7*, 19377–19389.

47. Wöhler, F., Ueber Verbindungen des Siliciums mit Sauerstoff und Wasserstoff. [Concerning Compounds of Silicon with Oxygen and Hydrogen] *Justus Liebigs Ann. Chem.* **1863,** *127*, 257–274.

48. Weiss, A.; Beil, G.; Meyer, H., The Topochemical Reaction Of $CaSi_2$ to a Two-dimensional Subsiliceous Acid $Si_6H_3(OH)_3$ (= Kautskys' Siloxene). *Z. Naturforsch. B* **1980**, *35*, 25–30.

49. Dahn, J. R.; Way, B. M.; Fuller, E.; Tse, J. S., Structure of Siloxene and Layered Polysilane. *Phys. Rev. B* **1993,** *48*, 17872–17877.

50. Vogg, G.; Brandt, M. S.; Stutzmann, M., Kinetics of the Topotactic Formation of Siloxene. *Chem. Mater.* **2003,** *15*, 910–915.

51. Nakano, H.; Ishii, M.; Nakamura, H., Preparation and Structure of Novel Siloxene Nanosheets. *Chem. Commun.* **2005,** *23*, 2945–2947.

52. Brandt, M. S.; Vogg, G.; Stutzmann, M., Silicon-and Germanium-Based Sheet Polymers and Zintl Phases. In *Silicon Chemistry*; John Wiley & Sons: Weinheim, 2007; pp. 194–199.

53. Kleewein, A.; Pätzold, U.; Hengge, E.; Tasch, S.; Leising, G. New Results in Cyclosilane Chemistry: Siloxene-Like Polymers. In *Organosilicon chemistry set: from molecules to materials;* Auner, N., Weis, J. Eds.; Wiley, 2008; pp. 327–332.

54. Hoenle, W.; Dettlaff-Weglikowska, S.; Molassioti-Dohms, A.; Weber, J., Siloxenes: What do we know about the Structures? In *Tailor-made silicon-oxygen compounds: from molecules to materials*; Vieweg, 1996; pp 99-116.

55. Oh, S. Y.; Imagawa, H.; Itahara, H., Facile and Scalable Synthesis of Silicon-Based Nanocomposites with Slitlike Nanopores: A Solid-state Exfoliation Reaction Using Layered $CaSi_2$. *Chem. Asian J.* **2014,** *9*, 3130–3135.

56. Imagawa, H.; Takahashi, N.; Nonaka, T.; Kato, Y.; Nishikawa, K.; Itahara, H., Synthesis of a Calcium-bridged Siloxene by a Solid State Reaction for Optical and Electrochemical Properties. *J. Mater. Chem. A* **2015,** *3*, 9411–9414.

57. Yaokawa, R.; Ohsuna, T.; Morishita, T.; Hayasaka, Y.; Spencer, M. J.; Nakano, H., Monolayer-to-bilayer Transformation of Silicenes and Their Structural Analysis. *Nat. Commun.* **2016,** *7*, 1–6.

58. Caflin, K. C.; Anderson, P. E., In-situ Remediation of Hydrogen Fluoride during a Detonation Event. *Propellants Explos. Pyrotech.* **2014,** *39*, 904–908.

59. Hou, S.; Zou, Y.; Liu, X.; Yu, X.; Liu, B.; Sun, X.; Xing, Y., CaF_2 and CaF_2: Ln^{3+} (Ln= Er, Nd, Yb) Hierarchical Nanoflowers: Hydrothermal Synthesis and Luminescent Properties. *CrystEngComm* **2011,** *13*, 835–840.

60. Ruprecht, B.; Wilkening, M.; Steuernagel, S.; Heitjans, P., Anion Diffusivity in Highly Conductive Nanocrystalline BaF_2:CaF_2 Composites Prepared by High-Energy Ball Milling. *J. Mater. Chem.* **2008,** *18*, 5412–5416.

61. Jain, P.; Kim, S.; Youngman, R. E.; Sen, S., Direct Observation of Defect Dynamics in Nanocrystalline CaF_2: Results from ^{19}F MAS NMR Spectroscopy. *J. Phys. Chem. Lett.* **2010,** *1*, 1126–1129.

62. Abdellatief, M.; Abele, M.; Leoni, M.; Scardi, P., Combined X-ray Diffraction and Solid-State ^{19}F Magic Angle Spinning NMR Analysis of Lattice Defects in Nanocrystalline CaF_2. *J. Appl. Crystallogr.* **2013,** *46*, 1049–1057.

63. Lorbeer, C.; Behrends, F.; Cybinska, J.; Eckert, H.; Mudring, A. V., Charge Compensation in RE^{3+} (RE = Eu, Gd) and M^+ (M = Li, Na, K) Co-Doped Alkaline Earth Nanofluorides Obtained by Microwave Reaction with Reactive Ionic Liquids Leading to Improved Optical Properties. *J. Mater. Chem. C* **2014,** *2*, 9439–9450.

64. Kiczenski, T.; Stebbins, J. F., Fluorine Sites in Calcium and Barium Oxyfluorides: ^{19}F NMR on Crystalline Model Compounds and Glasses. *J. Non-Cryst. Solids* **2002,** *306*, 160–168.

65. Yao, K.; Nishimura, S.; Inoue, K.; Abe, E.; Tateyama, H., CdS Nanoparticles Formed in the Interlayer Nanospace of Expandable Mica. *J. Mater. Sci. Lett.* **2001,** *20*, 1253–1254.

66. Wei, L. M.; Tang, T.; Huang, B. T., Synthesis and Characterization of Polyethylene/Clay-silica Nanocomposites: A Montmorillonite/Silica-hybrid-supported Catalyst and In Situ Polymerization. *J. Polym. Sci. A Polym. Chem.* **2004,** *42*, 941–949.

67. Ide, Y.; Fukuoka, A.; Ogawa, M., Preparation of Au Nanoparticles in the Interlayer Space of a Layered Alkali Silicate Modified with Alkylthiol Groups. *Chem. Mater.* **2007,** *19*, 964–966.

68. Wu, P.; Zhu, W.; Wei, A.; Dai, B.; Chao, Y.; Li, C.; Li, H.; Dai, S., Controllable Fabrication of Tungsten Oxide Nanoparticles Confined in Graphene-analogous Boron Nitride as an Efficient Desulfurization Catalyst. *Chem. Eur. J.* **2015**, *21*, 15421–15427.

69. Sun, J.; Liu, H.; Chen, X.; Evans, D. G.; Yang, W.; Duan, X., Synthesis of Graphene Nanosheets with Good Control over the Number of Layers within the Two-Dimensional Galleries of Layered Double Hydroxides. *Chem. Commun.* **2012,** *48*, 8126–8128.

70. Garcia, J. C.; de Lima, D. B.; Assali, L. V.; Justo, J. F., Group IV Graphene-and Graphane-like Nanosheets. *J. Phys. Chem. C* **2011,** *115*, 13242–13246.

71. Ding, Y.; Wang, Y., Electronic Structures of Silicene Fluoride and Hydride. *Appl. Phys. Lett.* **2012,** *100*, 083101–2.

72. Wei, W.; Jacob, T., Strong Many-body Effects in Silicene-based Structures. *Phys. Rev. B* **2013,** *88*, 045203–7.

73. Sun, X.; Li, Y., Size-Controllable Luminescent Single Crystal CaF_2 Nanocubes. *Chem. Commun.* **2003,** *14*, 1768–1769.

74. Schlyter, K., On the Crystal Structure of Fluorides of the Tysonite or LaF_3 Type. *Ark. Kemi* **1953,** *5*, 73–82.

75. Cheetham, A. K.; Fender, B. E. F.; Fuess, H.; Wright, A. F., A Powder Neutron Diffraction Study of Lanthanum and Cerium Trifluorides. *Acta Crystallogr. Sect. B-Struct. Sci.* **1976,** *32*, 94–97.

76. Swanson, H. E.; Tatge, E.; Fuyat, R. K., Standard X-ray Diffraction Powder Patterns. *Natl. Bur. Stand. (U.S.) Circ.* **1953,** *39*, 69.

77. Maksimov, B. A.; Sirota, M. I.; Galiulin, R. V.; Sobolev, B. P., The Crystal Structure of PrF_3 and the Twinning and Symmetry of Tysonite-like Structures. *Sov. Phys. Crystallogr.* **1985,** *30*, 284–289.

78. Kondratyuk, I. P.; Loshmanov, A. A.; Muradyan, L. A.; Maksimov, B. A.; Sirota, M. I.; Krivandina, E. A.; Sobolev, B. P., Neutron-Diffraction Study on NdF_3. *Sov. Phys. Crystallogr.* **1988,** *33*, 57–60.

79. McMurdie, H. F.; Morris, M. C.; Evans, E. H.; Paretzkin, B.; de Groot, J. H.; Hubbard, C. R.; Carmel, S.J., Standard X-ray Diffraction Powder Patterns. *Natl. Bur. Stand. (U.S.) Monogr.* **1962,** *25*, 41.

80. Greis, O. Ph.D. Thesis, University of Freiburg i. Br., Germany. Personal Communication, 1976.

81. Sobolev, B. P.; Garashina, L. S.; Fedorov, P. P.; Tkachenko, N. L.; Seiranyan, K. B., Polymorphism and Crystallographic Properties of Yttrium and Rare-earth Trifluorides. *Sov. Phys. Crystallogr.* **1974**, *18*, 473.

82. Zalkin, A.; Templeton, D. H., The Crystal Structures of YF_3 and Related Compounds. *J. Am. Chem. Soc.* **1953,** *75*, 2453–2458.

83. Swanson, H. E.; McMurdie, H. F.; Morris, M. C.; Evans, E. H.; Paretzkin, B., Standard X-ray Diffraction Powder Patterns. *Natl. Bur. Stand. (U.S.) Monogr.* **1972,** *25*, 23.

84. Liddell, K. Dept. of Mechanical, Materials & Manufacturing Engineering, Univ. of Newcastle, England, UK. Personal Communication, 1996.

85. Davidovich, R. L.; Kharlamova, L. G.; Samarets, L. V., Oxofluorovanadates of Alkali Metals and Ammonia. *Koord. Khim.* **1977**, *3*, 850.

86. Weitzera, F.; Schustera, J. C; Nakab, M.; Steinc, F.; Palmc, M., On the Reaction Scheme and Liquidus Surface in the Ternary System Fe–Si–Ti. **2008**, *16*, 273–282.

87. Konings, R. J. M.; Kovács, A. Thermodynamic Properties of the Lanthanide (II) Halides. In *Handbook on the physics and chemistry of rare earths*; Bünzli, J.C., Pecharsky, V.K. Eds.; Elsevier, 2003; pp.150–151.

88. Zachariasen, W., Crystal Chemical Studies of the 5f-series of Elements. XIV. Oxyfluorides, XOF. *Acta Crystallogr.* **1951,** *4*, 231–236.

89. Wang, X.; Zhuang, J.; Peng, Q.; Li, Y., Hydrothermal Synthesis of Rare-earth Fluoride Nanocrystals. *Inorg. Chem.* **2006,** *45*, 6661–6665.

90. Weller, P. F.; Kucza, J. A., Single-Crystal Growth of LaF_3. *J. Appl. Phys.* **1964,** *35*, 1945–1946.

91. Vijayakumar, M.; Selvasekarapandian, S.; Gnanasekaran, T.; Fujihara, S.; Koji, S., Characterization of Oxygen Impurities in Thermally Evaporated LaF_3 Thin Films Suitable for Oxygen Sensor. *Appl. Surf. Sci.* **2004,** *222*, 125–130.

92. Targove, J. D.; Lingg, L. J.; Lehan, J. P.; Macleod, H. A., Effect of Oxygen Incorporation on the Structure of Ion-beam-assisted LaF_3 Thin Films. *Appl. Opt.* **1988,** *27*, 213–215.

93. Sun, X.; Zhang, Y. W.; Du, Y. P.; Yan, Z. G.; Si, R.; You, L. P.; Yan, C. H., From Trifluoroacetate Complex Precursors to Monodisperse Rare-earth Fluoride and Oxyfluoride Nanocrystals with Diverse Shapes through Controlled Fluorination in Solution Phase. *Chem. Eur. J.* **2007,** *13*, 2320–2332.

94. Zeng, J. H.; Lou, T. J.; Wang, Y. F.; Guo, J. C.; Di, D.; Ma, R. L., Inorganic Single-Source Precursor to Complex Fluoride and Oxyfluoride Nanocrystallines and Their Photoluminescence. *J. Phys. Chem. C* **2008,** *113*, 597–602.

95. Hu, H.; Chen, Z.; Cao, T.; Zhang, Q.; Yu, M.; Li, F.; Yi, T.; Huang, C., Hydrothermal Synthesis of Hexagonal Lanthanide-doped LaF_3 Nanoplates with Bright Upconversion Luminescence. *Nanotechnology* **2008,** *19*, 375702–375711.

96. Cotton, S. *Lanthanide and actinide chemistry*; John Wiley & Sons, 2013.

97. De Marco, R.; Hauser, P.; Cattrall, R.; Liesegang, J.; Nyberg, G.; Hamilton, I., XPS Studies of the Fluoride Ion-selective Electrode Membrane LaF_3: Evidence for a Gel Layer on the Surface. *Surf. Interface Anal.* **1989,** *14*, 463–468.

98. Zhu, J.; Bai, L.; Sun, Y.; Zhang, X.; Li, Q.; Cao, B.; Yan, W.; Xie, Y., Topochemical Transformation Route to Atomically Thick Co_3O_4 Nanosheets Realizing Enhanced Lithium Storage Performance. *Nanoscale* **2013,** *5*, 5241–5246.

99. Chen, C.; Xu, L.; Sewvandi, G. A.; Kusunose, T.; Tanaka, Y.; Nakanishi, S.; Feng, Q., Microwave-assisted Topochemical Conversion of Layered Titanate Nanosheets to {010}-faceted Anatase Nanocrystals for High Performance Photocatalysts and Dye-sensitized Solar Cells. *J. Cryst. Grow.* **2014,** *14*, 5801–5811.

100. Zhang, G.; Sun, S.; Li, R.; Zhang, Y.; Cai, M.; Sun, X., Large-Scale Aqueous Synthesis and Growth Mechanism of Single-Crystalline Metal Nanoscrolls at Room Temperature: The Case of Nickel. *Chem. Mater*. **2010**, *22*, 4721–4727.

101. Zheng, Y.; Guo, N.; Jia, Y.; Qiao, H.; You, H., An Obvious Rolling Process in the Synthesis of Y_2O_3: Eu^{3+} Micro-urchins Built from Nanoscrolls. *CrystEngComm* **2012,** *14*, 7195–7200.

102. Kim, J.-H.; Lu, T.-M., Bio-inspired Janus Composite Nanoscrolls for On-demand Tumour Targeting. *RSC Adv.* **2016,** *6*, 17179–17187.

103. Li, Y.; Bando, Y.; Golberg, D.; Liu, Z. Ga-filled Single-crystalline MgO Nanotube: Wide-temperature Range Nanothermometer. *Appl. Phys. Lett.* **2003,** *83*, 999–1001.

104. Hu, J.; Bando, Y.; Liu, Z.; Zhan, J.; Golberg, D.; Sekiguchi, T., Synthesis of Crystalline Silicon Tubular Nanostructures with ZnS Nanowires as Removable Templates. *Angew. Chem. Int. Ed.* **2004,** *43*, 63–66.

CHAPTER 7

CONCLUSIONS

Conclusions

The metal borides are well known for their high melting points, strength and hardness which make them useful for high performance applications.[1,2,3] We have developed an innovative top-down method to nanostructure metal hexaborides and metal diborides using a lithiation insertion-exfoliation technique. We have successfully synthesized lithiated intermediates (Li_xMB_6) of strontium hexaboride and lanthanum hexaboride, and investigated these materials using PXRD, solid-state multinuclear NMR spectroscopy, and SEM. We treated the lithiated intermediates with water to cause a disassembly or exfoliation to yield nanoparticles of SrB_6 and nanosheets of LaB_6. These nanoproducts were in characterized using TEM, PXRD and NMR spectroscopy. We determined the effect of lithiating agent, reaction duration, reaction temperature, and morphology of starting material on the morphology of the respective nanoproducts formed.

We extended the lithium ion incorporation-exfoliation method to other hexaborides such as CaB_6, CeB_6 and SmB_6 and were able to nanostructure them to varying degrees using different lithiation methods and reaction durations.

We also applied this synthetic strategy to lithiate and exfoliate aluminum diboride, which has a layered crystal structure. We characterized lithiated AlB_2 using NMR, PXRD and SEM and exfoliated the Li_xAlB_2 using aqueous and non-aqueous conditions which yielded different nanoproducts with respect to morphology and composition, which we learned from NMR, TEM and PXRD analyses.

Metal fluorides are an attractive class of compounds for diverse applications in microelectronics, optoelectronics, coatings and catalysis.[4,5] Their advantageous properties include a non-hygroscopic nature, stability with respect to oxidation, and high transparency over a wide wavelength region.[6,7] We applied a novel, bottom-up synthetic approach to form CaF_2 nanosheets by utilizing layered calcium silicide as a templating agent to direct the growth of CaF_2 through interlayer confinement. The composition and morphology of the nanosheets were confirmed using PXRD, TEM and solid-state NMR spectroscopy.

We then used the CaF_2 nanosheets as a template to react with a variety of lanthanide salts to form lanthanide fluorides through topotactic transformation while preserving the nanoscale morphology. These reactions produced nanostructured hexagonal LnF_3 (Ln = Ce, Pr, Nd, Sm, Eu), orthorhombic LnF_3 (Ln = Gd, Dy, Ho, Er, Yb), and cubic YbF_{3-x} products with different morphologies such as nanosheet, nanoparticles, and nanoplatelets which were characterized using PXRD and TEM. Interestingly, the reaction of CaF_2 nanosheets with lanthanum salts is unique in producing nanoscrolls of $LaF_{3-2x}O_x$. While this topochemical transformation preserves the two-dimensional morphology it also causes lattice strain that initiates scrolling. These ~20 x 5 nm nanoscrolls are the first among metal fluoride materials.

References

1. Mroz, C. *Am. Ceram. Soc. Bull.*, **1995**. *74*. 165–166
2. Chambers, S. A., Swanson, L. W. *Surf. Sci*. **1983**. 131. *2-3*. 385-402.
3. Lundström, T. *Pure Appl. Chem*. **1985**. 57. *10*. 1383-90.
4. Fahrenholtz, W. G., Hilmas, G. E., Talmy, I. G., & Zaykoski, J. A. *J. Am. Ceram. Soc.* **2007.** 90. *5*. 1347-1364.
5. Cao, M.; Hu, C.; Wang, E. *J. Am. Chem. Soc*. **2003.** 125. 11196−11197.
6. Rü diger, S.; Groß, U.; Kemnitz, E. *J. Fluorine Chem*. **2007**. 128. 353− 368.
7. Hua, R.; Zang, C.; Shao, C.; Xie, D.; Shi, C. *Nanotechnol.* **2003**. 14. 588−591.
8. Mao, Y.; Zhang, F.; Wong, S. S. *Adv. Mater*. **2006**. 18. 1895−1899